

**CHARACTERIZATION OF HIGH MOMENTUM FLUX
COMBUSTION POWERED FLUIDIC ACTUATORS FOR HIGH
SPEED FLOW CONTROL**

A Thesis
Presented to
The Academic Faculty

by

Brett James Warta

In Partial Fulfillment
of the Requirements for the Degree
Master of Science in the
School of Mechanical Engineering

Georgia Institute of Technology
December 2007

**CHARACTERIZATION OF HIGH MOMENTUM FLUX
COMBUSTION POWERED FLUIDIC ACTUATORS FOR HIGH
SPEED FLOW CONTROL**

Approved by:

Dr. Ari Glezer, Advisor
School of Mechanical Engineering
Georgia Institute of Technology

Dr. Tom Crittenden
School of Mechanical Engineering
Georgia Institute of Technology

Dr. Tim Lieuwen
School of Aerospace Engineering
Georgia Institute of Technology

Date Approved: Nov. 13th 2007

ACKNOWLEDGEMENTS

First of all I would like to thank my advisor Dr. Ari Glezer. I feel very fortunate that he took me in as one of his students and lucky to have had the opportunity to work with him on this project. Ari was there to push me and to ensure that I always had more work to be done. It has been a rewarding experience and one that I am very grateful to have been a part of. I would also like to express my gratitude to Dr. Tom Crittenden for all of his invaluable input and expert knowledge that had help me throughout my project. Tom played a major role in getting me started here at the Fluid Mechanics Research Lab. He taught me a lot regarding this project and was always happy to help if ever an issue had surfaced. Additionally, I want to express gratitude to Dr. Tim Lieuwen for being on my committee and for lending his expertise in combustion processes. And, I would like to thank the generous funding support of the NASA URETI program for Aero propulsion and Power Technology which made this work possible, and the Georgia Institute of Technology.

I am very grateful for having such a loving and supportive family that has helped me unconditionally. They were there to encourage me when I decided to pursue my graduate degree, and I know they will be there supporting me throughout my future career. I would like to extend a special thanks to my mother, she has always been someone I respect very much and someone that I could consult. She always made sure that my decisions were in the best interest for me personally. I want her to know that I am very grateful for the countless things that she has helped me with and that she has my full

admiration. Also, I would like to mention my dad for all of his support and encouragement throughout the years. He helped instill confidence in myself, and greatly contributed to where I am today.

Lastly, I would like to thank all of my friends that I have made here. They all contributed greatly to making the time I spent in Atlanta truly memorable. I would like to mention my labmates who all have been exceedingly helpful during my two-plus year stint. Especially Dan Brzozowski, Dave Garth, Hanif Hunter, and John Culp whom we had spent many late nights working hard in the lab, consumed countless cups of coffee, and shared many laughs.

TABLE OF CONTENTS

	Page
ACKNOWLEDGEMENTS	iii
LIST OF TABLES	vii
LIST OF FIGURES	viii
NOMENCLATURE	xiii
SUMMARY	xvi
<u>CHAPTERS</u>	
1. INTRODUCTION	1
1.1 Motivation	1
1.2 Brief Outline	5
2. LITERATURE REVIEW	7
2.1 Overview	7
2.2 Small Scale Combustion	7
2.3 Resonant Combustion Chambers	10
2.4 Earlier COMPACT Development	11
3. EXPERIMENTAL SETUP	15
3.1 Combustion Chamber	15
3.2 Data Acquisition	19
3.3 Flame Photography	20
4. PREMIXED AND NONPREMIXED COMBUSTOR CONFIGURATIONS	22
4.1 Global Difference in Premixed and Nonpremixed combustors	22
4.2 Parametric Study of Nonpremixed and Premixed Combustor Configuration	33
4.2.1 Fuel Type and Equivalence Ratio	33
4.2.2 Combustion Frequency	38
4.2.3 Chamber Volume	40
4.2.4 Flow Rates	44
4.2.5 Exhaust Orifice Diameter	45

5. OPTIMIZATION OF OPERATING FREQUENCY	48
5.1 Flow Field Characteristics	49
5.1.1 Fuel & Equivalence Ratio	49
5.1.2 Combustion Frequency	52
5.1.3 Variation of Actuator Impulse	54
5.1.4 Flow Rate	63
5.1.5 Spark Location and Multiple Ignition Points	66
5.2 Chamber Size and Shape	70
5.2.1 Chamber Volume	70
5.2.2 Aspect Ratio	72
5.3 Fuel/Air Injection	75
5.3.1 Air Inlet	75
5.3.2 Fluidic Element	77
5.3.3 Reed Valves	80
5.3.4 Direct Injection of Fuel and Air	84
6. CONCLUSION	90
REFERENCES	95

LIST OF TABLES

	Page
Table 4.1: Fuel properties of Hydrogen and Propane (Turns 2000; Crittenden 2003).	36
Table 4.2: Surface area to volume ratio given various volumes and aspect ratio	41

LIST OF FIGURES

	Page
Figure 1.1: Phase averaged smoke visualization images of the flow above the surface of an airfoil ($\alpha = 15^\circ$, $\gamma = 60^\circ$). Baseline (a), $St_{C_{act}} = 0.7$ (b), 1.1 (c), 2.05 (d), 3.3 (e), and 10 (f). Courtesy Glezer and Amitay (Glezer, Amitay et al. 2005).	2
Figure 1.2: Basic COMPACT prototype schematic.	4
Figure 2.1: Phase-averaged chamber pressure with phase-locked Schlieren images of exhaust jet ($V = 1$ cc, $H/D = 1.27$, hydrogen/air premixed $\Phi = 0.62$, $d = 1.3$ mm, $Q = 50$ cc/s, and $f = 30$ hz)	12
Figure 2.2: Generic pressure-time history of combustion powered actuator including t_{mix} for nonpremixed operation	14
Figure 3.1: Fuel injection configurations of premixed (a), nonpremixed (b), and direct injection (c).	16
Figure 3.2: Diagram of COMPACT combustion chamber with chamber dimensions	17
Figure 3.3: Simple air injection configuration schematic	19
Figure 3.4: A 2cc windowed chamber for flame photography.	21
Figure 4.1: Premixed (—) and nonpremixed (—) pressure time history of hydrogen 2cc chamber, $Q = 6$ L/min, $\Phi = 0.41$, $d = 1.78$ mm, (—) 1 Hz, (---) 35 Hz, (····) 55 Hz.	26
Figure 4.2: Peak pressure vs. f/f_i , of hydrogen 2cc, $Q = 12$ L/min premixed (+) and nonpremixed (+), $Q = 6$ L/min premixed (•) and nonpremixed (•), $\Phi = 0.41$, $d = 1.78$ mm.	26
Figure 4.3: Premixed (—) and nonpremixed (—) pressure time history with photograph location; Propane, 2cc, $Q = 9$ L/min, $\Phi = 1.0$, $d = 1.78$ mm, $f = 30$ Hz.	29
Figure 4.4: Premixed propane flame propagation, 2cc, $Q = 9$ L/min, $\Phi = 1.0$, $d = 1.78$ mm, $f = 30$ Hz at $t = 1.1$ ms (a), 1.8 ms (b), 2.5 ms (c), 3.1ms (d), 3.6 ms (e), 4.0 ms (f), 4.7 ms (g), 5.3 ms (h), and 7.0 ms (i).	30

- Figure 4.5: Nonpremixed propane flame propagation, 2cc, $Q = 9/\text{min}$, $\Phi = 1.0$, $d = 1.78$ mm, $f = 30$ Hz at $t = 1.1$ ms (a), 1.8 ms (b), 2.5 ms (c), 3.1ms (d), 3.6 ms (e), 4.0 ms (f), 4.7 ms (g), 5.3 ms (h), and 7.0 ms (i). 31
- Figure 4.6: Nonpremixed propane combustion pressure time history with $\Phi = 0.74$ (—), 0.86 (—), 1.00 (—), 1.15 (—), 1.31 (—), $V = 2\text{cc}$, $Q = 4.8$ L/min, $d = 0.89$ mm, $f = 5$ Hz, $H/D = 1.25$. 34
- Figure 4.7: Nonpremixed hydrogen combustion pressure time history with $\Phi = 0.32$ (···), 0.41 (···), 0.51 (—), 0.62 (—), 0.74 (—), 0.86 (—), 1.00 (—), 1.15 (—), $V = 2\text{cc}$, $Q = 4.8$ L/min, $d = 0.89$ mm, $f = 5$ Hz, $H/D = 1.25$. 35
- Figure 4.8: Premixed (—) and Nonpremixed (---) pressure time history at $\Phi = 0.32$ (—), 0.41 (—), 0.51 (—), 0.74 (—), 2cc , $Q = 14\text{L}/\text{min}$, $d = 1.98$ mm, $f = 20$ Hz. 37
- Figure 4.9: Peak pressure vs. normalized actuation frequency, comparing ideal performance (---) to measured performance (•). $V = 2\text{cc}$, $Q = 12$ L/min, $\Phi = 0.41$, $d = 1.78$ mm. 38
- Figure 4.10: Pressure time history, premixed (a) and nonpremixed (b) hydrogen $V = 0.25\text{cc}$ (—), 0.50cc (—), 0.75cc (—), 1.00cc (—), 2cc (—), ignition spark is fired at 1 ms, $Q = 4$ L/min, $\Phi = 0.51$, $d = 0.89$ mm, $f = 10$ Hz. 43
- Figure 4.11: Pressure time history of premixed (—) and nonpremixed (···) hydrogen combustion with $Q = 4.80$ L/min (—), 7.20 L/min (—), 9.60 L/min (—), ignition spark at 1 ms, $V = 2\text{cc}$, $\Phi = 0.51$, $d = 1.50$ mm, $f = 10$ Hz, $H/D = 1.25$. 45
- Figure 4.12: Pressure time history of premixed (—) and nonpremixed (---) hydrogen combustion with $d = 1.61$ mm (—), 1.98 mm (—), 2.21 mm (—), ignition spark at 1 ms, $V = 2\text{cc}$, $Q = 18$ L/min, $\Phi = 0.37$, $f = 10$ Hz, $H/D = 2.27$. 47
- Figure 5.1: Peak pressure plot of propane mixture (a) and hydrogen mixture (b) with $\Phi = 0.32$ (···), 0.41 (···), 0.51 (—), 0.62 (—), 0.74 (—), 0.86 (—), 1.00 (—), 1.15 (—), $V = 2\text{cc}$, $Q = 4.8$ L/min, $d = 0.89$ mm, $H/D = 1.25$. 51
- Figure 5.2: Pressure time history at $f/f_i = 0.10$ (—), 0.20 (—), 0.30 (—), 0.40 (—), 0.50 (—), 0.60 (—), 0.75 (—), 0.90 (—), 1.05 (—), 1.20 (—), 1.35 (—), 1.50 (—), 1.65 (—), 1.80 (—), 1.95 (—), 2.10 (—), 2.25 (—), 2.40 (—), 2.55 (—), ignition at 1 ms, $V = 2\text{cc}$, $Q = 2.4$ L/min, $d = 0.89$ mm, $\Phi = 0.51$, $H/D = 2.27$. 53

- Figure 5.3: Pressure time history with $d = 1.50$ mm (—), 1.61 mm (—), 1.78 mm (—), 1.98 mm (—), 2.21 mm (—), 2.54 mm (—), spark initiated at 1 ms, $V = 2$ cc, $Q = 18$ L/min, $\Phi = 0.37$, $H/D = 2.27$, $h/d = 2$, $f = 10$ Hz. 55
- Figure 5.4: Peak Pressure with $d = 1.50$ mm (—), 1.61 mm (—), 1.78 mm (—), 1.98 mm (—), 2.21 mm (—), 2.54 mm (—), $V = 2$ cc, $Q = 18$ L/min, $\Phi = 0.37$, $H/D = 2.27$, $h/d = 2$. 55
- Figure 5.5: Peak thrust [N] with $d = 1.50$ mm (—), 1.61 mm (—), 1.78 mm (—), 1.98 mm (—), 2.21 mm (—), 2.54 mm (—), $V = 2$ cc, $Q = 18$ L/min, $\Phi = 0.37$, $H/D = 2.27$, $h/d = 2$. 59
- Figure 5.6: Impulse computed during t_{pulse} [N·s] with $d = 1.50$ mm (—), 1.61 mm (—), 1.78 mm (—), 1.98 mm (—), 2.21 mm (—), 2.54 mm (—), $V = 2$ cc, $Q = 18$ L/min, $\Phi = 0.37$, $H/D = 2.27$, $h/d = 2$. 59
- Figure 5.7: Impulse gain during t_{pulse} with $d = 1.50$ mm (—), 1.61 mm (—), 1.78 mm (—), 1.98 mm (—), 2.21 mm (—), 2.54 mm (—), $V = 2$ cc, $Q = 18$ L/min, $\Phi = 0.37$, $H/D = 2.27$, $h/d = 2$. 60
- Figure 5.8: Impulse gain computed over τ with $d = 1.50$ mm (—), 1.61 mm (—), 1.78 mm (—), 1.98 mm (—), 2.21 mm (—), 2.54 mm (—), $V = 2$ cc, $Q = 18$ L/min, $\Phi = 0.37$, $H/D = 2.27$, $h/d = 2$. 60
- Figure 5.9: Circular simple orifice cross-sectional and top view (a) and converging-diverging cross-sectional view (b). 61
- Figure 5.10: Pressure time history varying $h/d = 2.0$ (—), 0.5 (—), 0.7 converging (—), and CD nozzle (—), $V = 2$ cc, $Q = 14$ L/min, $\Phi = 0.51$, $d = 1.78$ mm, $f = 30$ Hz. 62
- Figure 5.11: Peak pressure vs. normalized actuation frequency varying $h/d = 2.0$ (—), 0.5 (—), 0.7 converging (—), and CD nozzle (—), $V = 2$ cc, $Q = 14$ L/min, $\Phi = 0.51$, $d = 1.78$ mm. 62
- Figure 5.12: Pressure time history varying $Q = 18.0$ (—), 16.0 L/min (—), 14.0 (—), 12.0 (—) and 10.0 (—), $V = 1.33$ cc, $\Phi = 0.27$, $d = 1.98$ mm, $H/D = 1.51$, $f/f_i = 0.5$. 64
- Figure 5.13: Peak pressure vs. actuation frequency, f , varying $Q = 18.0$ (—), 16.0 L/min (—), 14.0 (—), 12.0 (—) and 10.0 (—), $V = 1.33$ cc, $\Phi = 0.27$, $d = 1.98$ mm, $H/D = 1.51$. 64
- Figure 5.14: Peak pressure vs. normalized frequency, f/f_i , varying $Q = 18.0$ (—), 16.0 L/min (—), 14.0 (—), 12.0 (—) and 10.0 (—), $V = 1.33$ cc, $\Phi = 0.27$, $d = 1.98$ mm, $H/D = 1.51$. 65

- Figure 5.15: Pressure time history comparing spark location $l/H = 0.75$ (—), 0.50 (—), 0.25 (—), $V = 2\text{cc}$, $Q = 2.4\text{ L/min}$, $\Phi = 0.51$, $d = 0.89\text{ mm}$, $H/D = 2.27$, $f = 2\text{ Hz}$. 67
- Figure 5.16: Peak pressure vs. normalized actuation frequency comparing spark location $l/H = 0.75$ (—), 0.50 (—), 0.25 (—), $V = 2\text{cc}$, $Q = 2.4\text{ L/min}$, $\Phi = 0.51$, $d = 0.89\text{ mm}$, $H/D = 2.27$. 68
- Figure 5.17: Pressure time history comparing multiple sparks and their location $l/H = 0.75$ & 0.50 (—), 0.50 & 0.25 (—), 0.75 & 0.50 & 0.25 (—), $V = 2\text{cc}$, $Q = 2.4\text{ L/min}$, $\Phi = 0.51$, $d = 0.89\text{ mm}$, $H/D = 2.27$, $f = 2\text{ Hz}$. 69
- Figure 5.18: Peak pressure comparing multiple sparks and their location $l/H = 0.75$ & 0.50 (—), 0.50 & 0.25 (—), 0.75 & 0.50 & 0.25 (—), $V = 2\text{cc}$, $Q = 2.4\text{ L/min}$, $\Phi = 0.51$, $d = 0.89\text{ mm}$, $H/D = 2.27$, $f = 2\text{ Hz}$. 70
- Figure 5.19: Nonpremixed peak pressure vs. actuation frequency with $V = 0.25$ (—), 0.50 (—), 0.75 (—), 1.00 (—), 2cc (—), $Q = 4\text{ L/min}$, $d = 0.89\text{ mm}$, and $\Phi = 0.51$. 71
- Figure 5.20: Nonpremixed peak pressure vs. normalized actuation frequency with varying $V = 0.25$ (—), 0.50 (—), 0.75 (—), 1.00 (—), 2cc (—), $Q = 4\text{ L/min}$, $d = 0.89\text{ mm}$, and $\Phi = 0.51$. 72
- Figure 5.21: Pressure time history with $H/D = 1.27$ (—) and $H/D = 2.27$ (—) for $V = 2\text{cc}$, $Q = 4.8\text{ L/min}$, $d = 1.50\text{ mm}$, $\Phi = 0.51$, $f = 10\text{ Hz}$. 74
- Figure 5.22: Peak pressure ratio vs. normalized frequency with $H/D = 1.27$ (—) and $H/D = 2.27$ (—) for $V = 2\text{cc}$, $Q = 4.8\text{ L/min}$, $d = 1.50\text{ mm}$, $\Phi = 0.51$. 75
- Figure 5.23: Pressure time history with air intake $l_a/H = 0.25$ (—), $l_a/H = 0.50$ (—), $l_a/H = 0.75$ (—), $V = 2\text{cc}$, $Q = 4.8\text{ L/min}$, $d = 0.89\text{ mm}$, $\Phi = 0.51$, $H/D = 2.27$, $f = 2\text{ Hz}$, $r/R = 0.50$. 76
- Figure 5.24: Peak pressure vs. actuation frequency of three air intake $l_a/H = 0.25$ (—), $l_a/H = 0.50$ (—), $l_a/H = 0.75$ (—), $V = 2\text{cc}$, $Q = 4.8\text{ L/min}$, $d = 0.89\text{ mm}$, $\Phi = 0.51$, $H/D = 2.27$, $f = 2\text{ Hz}$, $r/R = 0.50$. 77
- Figure 5.25: Pressure time history with varying sintered metal porosity level of 2 (—), 5 (—), 10 (—), 20 (—), $40\mu\text{m}$ (—), $V = 2\text{cc}$, $Q = 2.4\text{ L/min}$, $d = 1.50\text{ mm}$, $\Phi = 0.51$, $H/D = 2.27$, and $f = 2\text{ Hz}$. 78
- Figure 5.26: Peak pressure with varying sintered metal porosity level of 2 (—), 5 (—), 10 (—), 20 (—), $40\mu\text{m}$ (—), $V = 2\text{cc}$, $Q = 2.4\text{ L/min}$, $d = 1.50\text{ mm}$, $\Phi = 0.51$, $H/D = 2.27$. 79

- Figure 5.27: Peak pressure with varying sintered metal porosity level of 2 (—), 5 (—), 10 (—), 20 (—), 40 μ m (—), $V = 2\text{cc}$, $Q = 3.6\text{ L/min}$, $d = 1.50\text{ mm}$, $\Phi = 0.51$, $H/D = 2.27$. 79
- Figure 5.28: Reed valve design utilizing two plates, inlet orifice grid plate (a), and reed valve plate (b and c). 81
- Figure 5.29: Pressure time history comparing conventional reedless design (—) with reed valve lengths of 1.40 (—), 1.75 (—), 2 mm (—), 11 reed configuration, 12.7 μ m thick reeds, $V = 2\text{cc}$, $Q = 14\text{ L/min}$, $d = 1.78\text{ mm}$, $\Phi = 0.37$, $f = 10\text{ Hz}$, $H/D = 1.27$. 82
- Figure 5.30: Peak pressure vs. normalized frequency comparing conventional reedless design (—) with reed valve lengths of 1.40 (—), 1.75 (—), 2 mm (—), 11 reed configuration, 12.70 μ m thick reeds, $V = 2\text{cc}$, $Q = 14\text{ L/min}$, $d = 1.78\text{ mm}$, $\Phi = 0.37$, $H/D = 1.27$. 83
- Figure 5.31: Pressure time history comparing conventional reedless design (—) to reeds made of 301SS (—), Spring Steel (—), Ti (—), Graphite foil (—), reed length 2 mm and thickness 50.80 μ m, $V = 2\text{cc}$, $Q = 14\text{ L/min}$, $d = 1.61\text{ mm}$, $\Phi = 0.37$, $H/D = 1.27$, and $f/f_i = 0.17$. 84
- Figure 5.32: Different injection configurations: standard injection with sintered metal (a), direct injection with induced co-rotational swirl (b), direct injection with impinging flow and swirl (c), and direct injection with impinging flow (d). 86
- Figure 5.33: Pressure time history comparing the use of sintered metal (—) with direct injection of co-rotational swirl (—), impinging swirl (—), and impinging without swirl (—), $V = 2\text{cc}$, $Q = 14\text{ L/min}$, $d = 1.98\text{ mm}$, $\Phi = 0.37$, $H/D = 1.27$ (100 micron sintered metal used). 87
- Figure 5.34: Peak pressure comparing the use of sintered metal (—) with direct injection co-rotational swirl (—), impinging swirl (—), and impinging without swirl (—), $V = 2\text{cc}$, $Q = 14\text{ L/min}$, $d = 1.98\text{ mm}$, $\Phi = 0.37$, $H/D = 1.27$ (100 micron sintered metal used). 88

NOMENCLATURE

A	orifice area
A_i	inviscid area
c	speed of sound
d	exhaust orifice diameter
d_a	air inlet diameter
d_f	fuel inlet diameter
D	combustion chamber diameter
f	actuation frequency or operating frequency, the frequency in which the actuator is operating
f_{\max}	maximum attainable actuation frequency
f_s	spark frequency, the frequency in which the ignition system is operating
f_i	the ideal actuation frequency at which the time between combustion is sufficient for one complete chamber refill of A/F mix [$\equiv Q/V$]
f/a	fuel/air
h	exhaust orifice height
H	combustion chamber height
J	combustion impulse during pulse duration
J_o	impulse without combustion
J_t	impulse during entire combustion cycle period
l	distance of spark along of the axis of the chamber from the exhaust orifice
l_a	distance of air orifice from exhaust orifice
l_c	cord length of an airfoil

l_f	distance of fuel orifice from exhaust orifice
M	Mach number
P_o	baseline chamber pressure, without combustion
P_a	atmospheric pressure
P_b	back pressure
P_c	combustion chamber pressure
P_e	exit plane pressure
P_{\max}	maximum chamber pressure, or peak pressure, obtained during combustion cycle
P_r	normalized pressure [$\equiv P_c/P_a$]
P_t	stagnation pressure
Q	volumetric flow rate
R	radius of combustion chamber [$\equiv D/2$]
r	radial distance from combustion chamber center [$r \leq R$]
Re	Reynolds number [$\equiv Ud/\nu$, where d is the characteristic length desired]
S_L	laminar flame speed
S_T	turbulent flame speed
St	Strouhal number, typically based on chord length [$\equiv fC/U_\infty$]
STP	standard temperature and pressure (300 K and 1 atm)
t	time, referenced from point of ignition discharge
t_{mix}	time required for mixing to occur in nonpremixed operation
t_{peak}	time to peak pressure
t_{pulse}	time duration of pressure increase due to combustion
t_{refill}	time duration of new reactants into the combustion chamber

U	velocity
U_∞	free stream velocity
V	combustion chamber volume
v	velocity
v'_{rms}	mean unburned gas velocity
α	thermal diffusivity or airfoil angle of attack
δ_L	laminar flame thickness
γ	specific heat ratio
\overline{m}_F	average reaction rate
ν	kinematic viscosity
ρ	density
ρ_b	density of burned mixture
ρ_u	density of unburned mixture
τ	cycle period [$\equiv 1/f$]
τ_{conv}	convective time scale over an airfoil [$\equiv U_\infty/l_c$]
Φ	equivalence ratio fuel/air [1.0 = stoichiometric; lean < 1.0 < rich]
Φ_{eff}	effective equivalence ratio fuel/air + exhaust present
Φ_{min}	lower flammability limit equivalence ratio
ω	vorticity
∞	free stream properties

SUMMARY

The performance of a high-power small-scale combustion-based fluidic actuator for high-speed flow control applications is characterized with specific focus on comparisons between premixed and nonpremixed operating modes for the device. Momentary (pulsed) actuation jets are produced by the ignition of a mixture of gaseous fuel and oxidizer within a small (cubic centimeter scale) combustion chamber. The combustion process yields a high pressure burst (1 to 3 ms in duration in the typical configurations) and the ejection of a high-speed exhaust jet. The actuation frequency can be continuously varied by independently controlling the flow rate of the fuel/oxidizer and the spark ignition frequency up to a maximum determined by the operating characteristics of the actuator. The actuator performance is characterized by both its peak thrust and net total impulse, with increases in peak jet momentum often two to three orders of magnitude above the baseline steady jet. Results for operation of the device in both premixed and nonpremixed modes are presented and analyzed, with nonpremixed operation typically yielding higher pressures and greater frequency ranges in the present configurations.

CHAPTER 1

INTRODUCTION

1.1 Motivation

The control of flow separation over aerodynamic surfaces can expand the envelope of flight platforms in ways that are not feasible with conventional flaps and mechanical surfaces. Active control of flow separation can aid in increasing aerodynamic performance, decrease drag, and extend a system's range of capabilities. By replacing mechanical control surfaces with non-intrusive fluidic actuators, the overall system performance can be improved (e.g. reduced weight, complexity, power consumption), while opening up a new realm of aero maneuvering capabilities.

Significant ongoing research at the Georgia Institute of Technology has focused on the development and demonstration of synthetic jet actuators for controlling shear flows. These devices are comprised of an enclosed cavity with a simple orifice where a jet is created by the time-periodic motion of a driver (typically a moving diaphragm) that results in blowing and suction of fluid out of into the cavity. Synthetic jets were extensively investigated by Smith and Glezer (1998). The use of synthetic jets for manipulation of separated flows was demonstrated by Amitay with his work on a stalled airfoil (Amitay 1998; Amitay, Kibens et al. 1999) and by Vukasinovic (2006) in a free shear layer experiment. These studies differ from that of early flow control experiments in that the dimensionless frequency of excitation was at least an order of magnitude

higher than the characteristic frequency of the flow [i.e., $St \geq O(10)$] rather than on the same order as the characteristic frequency of the flow [i.e., $St \sim O(1)$]. This technique is applicable over a broader range of flow conditions since it does not rely on coupling to global flow instabilities.

Early work with flow control using synthetic jets or pulsed blowing techniques demonstrated success with actuators having a momentum coefficient (C_μ) on the order of 10^{-3} . Figure 1.1 illustrates the progression of attaching flow to a stalled wing at a high angle of attack using synthetic jets. The outset of the actuation near the leading edge leads to the collapse of the separated flow domain and the formation of transitory large scale vortices followed by flow attachment. These vortical transients are of interest because of their ability to create strong momentary aerodynamic forces on the wing.

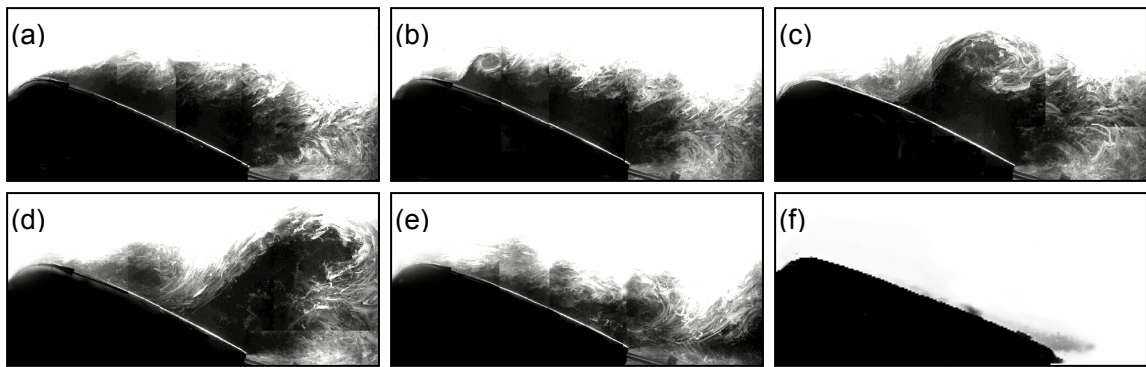


Figure 1.1: Phase averaged smoke visualization images of the flow above the surface of an airfoil ($\alpha = 15^\circ$, $\gamma = 60^\circ$). Baseline (a), $St_{\text{cact}} = 0.7$ (b), 1.1 (c), 2.05 (d), 3.3 (e), and 10 (f). Courtesy Glezer and Amitay (2005).

The methods of flow control mentioned above have been effective for relatively low flight speeds, which could prove useful in unmanned aerial vehicles (UAV) or micro-UAVs, but clearly an actuator with a larger momentum flux or C_μ would be needed in order to effectively operate at the higher flight speeds (transonic or supersonic). This application spawned the development of two novel actuator designs that were investigated by Crittenden (2003), which were a high-speed compressible synthetic jet and the combustion-driven pulsed jet actuator. While the high-speed compressible synthetic jet involves a motor driven piston design, the combustion-driven actuator has no moving parts and is comprised of a combustion chamber using a spark for ignition of fuel and oxidizer. The combustion powered actuator (COMPACT) is deemed as the most suitable for high speed flow control due to its relative simplicity and relatively low weight.

COMPACT is a novel actuation design which exploits the chemical energy of a fuel/oxidizer mixture to create a high momentum jet of exhaust products following a momentary combustion process. The COMPACT design (as illustrated in Figure 1.2) consists of a chamber volume where fuel and oxidizer are mixed and ignited by a continuously variable spark. The combustion of the mixture results in an increase of the pressure within the chamber as chemical energy is released, leading to exhaust venting out of the chamber through a simple orifice, thereby creating the high momentum jet pulse. By periodic ignition of the gaseous mixture to create the pulsed jet, periodic actuation may be effected which can outperform steady actuation (e.g., continuous

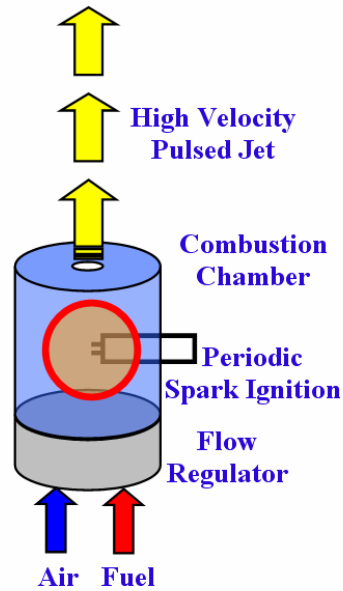


Figure 1.2: Basic COMPACT prototype schematic.

blowing). Additionally, chemically based actuation presents some attractive alternatives to conventional mechanical actuation, most notably, its low weight design, low power input requirements, and a more rapid response to changes in the flight dynamic.

A number of investigations have confirmed the effectiveness of transitory or pulsed actuation, where the actuation duty cycle is low. Brzozowski and Glezer (2006) used pulsed combustion actuation near the leading edge ($x/c = 0.2$) of a stalled airfoil to induce remarkably strong transitory changes in the circulation around the airfoil. Increases in circulation of up to 25% (compared to the baseline stalled state), accompanied by changes in the streamwise and cross stream momentum fluxes which are

associated with decreases in drag and increases in lift respectively. These tests were conducted using a NACA 4415 airfoil at angles of attack exceeding 16° and a chord Reynolds number of 570,000.

While the principal ideas of the pulsed combustion actuator were established in the earlier works of Crittenden, the characteristic operating times was limited by the internal refill process thereby affecting the operating frequency. A high operating frequency is needed for high-speed applications. The research presented in this thesis focuses primarily on efforts to increase the actuation frequency of the COMPACT technology, through more controlled mixing and combustion processes.

1.2 Brief Outline

The second chapter of this thesis covers the literature review and discusses some of the previous work on small scale combustion, particularly with Microelectromechanical Systems (MEMS). In the area of power MEMS, it is desired to use small-scale combustion as a source of high density power. Examples of power MEMS applications that are under investigation include micro-gas turbines, micro-rotary engines, and a free-piston design. Other applicable topics include a mini-pulsejet and a resonant detonation actuator that have been built. This discussion is followed by an overview of prior research with the pulsed combustion fluidic actuator, COMPACT, that was developed at Georgia Institute of Technology, using a premixed fuel/oxidizer design.

The third chapter overviews the present experimental setup. This includes a detail of the combustion chamber design, data acquisition, and the flame photography setup. The different types of premixed and nonpremixed configurations are also explained. The fourth chapter is dedicated to illustrating the differences in performance between the premixed and nonpremixed COMPACT designs. It describes the difference in the chamber configuration and elaborates on the benefit of turbulent mixing within the chamber. The present research includes an extensive parametric investigation of the pulsed combustion process including the effects of fuel type, equivalence ratio, exhaust orifice diameter, chamber aspect ratio, chamber volume, flow rate, and the actuation frequency.

Chapter 5 details several attributes of the nonpremixed pulsed combustion fluidic actuator. Including the effects of inlet placement and modification of turbulent mixing within the chamber, ignition location, and flow rate. Finally chapter 6 is a summery of the findings from the present investigations.

CHAPTER 2

LITERATURE REVIEW

2.1 Overview

The focus of this thesis is to illustrate the characteristics and benefits of nonpremixed combustion powered actuator (COMPACT) over the earlier premixed approach. This chapter begins with an overview of small scale combustion, illustrating problems and solutions in other investigations including MEMS combustion, pulsed detonation actuators, and miniature pulsejets. The last section reviews earlier investigation of a premixed COMPACT configuration.

2.2 Small Scale Combustion

In recent years, there has been considerable interest in small scale processes for applications in micro electro mechanical systems (MEMS) (Epstein, Senturia et al. 1997). This interest was motivated by the need for high energy density power to replace battery packs and small-scale propulsion for micro vehicles. This research has focused on combustion processes at scales that are on the same order as the flame thickness. The utilization of combustion is advantageous because the high energy density available is approximately 1000 times that of batteries (Lee, Park et al. 2001). This demand has spawned an array of microscale heat engines modeled after classical thermodynamic

cycles. Studies at the microscale level have included gas turbines (Waitz, Gauba et al. 1996), rotary (Wankel-like) engines (Fu, Knobloch et al. 2001) and reciprocating free-piston internal combustion engine (Lee, Park et al. 2001), pulsejets (Kiker 2005), and rocket engines (Epstein, Senturia et al. 1997). Significant work on small-scale combustion was performed on the MIT micro-gas turbine engine, whose research prototype involved combustion properties, material selection, and MEMS fabrication approach (Waitz, Gauba et al. 1996).

Combustion within a volume where the distance between the walls is on the order of the flame quenching distance poses challenges for sustaining a flame. For quiescent hydrogen mixture at STP, the flame quenching distance is 0.61mm near stoichiometric mixtures and is the smallest of any other common fuel. There have been attempts to decrease this distance in order to improve flame stability. Since the quenching distance is proportional to the flame thickness, reducing the flame thickness can be achieved by burning under high pressure and preheating the mixture prior to combustion. Another problematic issue is that an increase in flow velocity and/or turbulent mixing results in an increased flame thickness and therefore sustaining flames at small scales becomes even more difficult (Ballal and Lefebvre 1975).

Small scale combustion is also accompanied by low thermal efficiency. A combustion chamber hosting a relatively large surface area is more susceptible to heat loss. When combustion chambers approach smaller volumes, the ratio of surface area to volume, A_s/V , increases significantly. With surface area and volume corresponding to

heat loss and to a measure of potential heat generation respectively, the higher the A_s/V , the harder it is to sustain a flame. When the surface area to volume ratio is excessive, heat losses to the wall overwhelms the rate of heat production from combustion and no detectable pressure rise occurs after ignition (Lee, Park et al. 2001). Currently, some investigations utilize surface catalytic combustion systems as a means to improve the reaction rate of fuel/air mixtures. The interior of the combustion chamber is coated with platinum and heated from an external source to a temperature which ignites the mixture. Once the mixture is ignited, the external heat source is turned off and the heat from the flame sustains the process. Using the walls as the source of autoignition removes much of the problems with cold wall quenching (Boyarko, Sung et al. 2004; Spadaccini, Peck et al. 2007).

Unlike many of the power MEMS designs, COMPACT's goal is not to sustain a constant flame, but to repeatedly create a small transient combustion process, where combustion is initiated and extinguished at a high frequency without the aid of mechanical valving. The simplicity to COMPACT design enables reliability and minimal energy inputs. Furthermore, it only allows for minimal pre-pressurization since the combustion chamber is open to the environment at the exhaust orifice. In fact, preheating the combustible mixture hinders COMPACT's ability to quench flames, creating standing flames which render the actuator ineffective and limit the actuation frequency.

2.3 Resonant Combustion Chambers

Combustion chambers which utilized the resonant frequency of the chamber and its shape to induce pulsed combustion have been used since before the development of the German V-1 “Buzz Bomb.” Most applications are focused on propulsion technologies, directing the power generated from pulsed combustion through a nozzle to create thrust. The advent of turbojet technologies quickly surpassed pulsejet in terms of fuel efficiency and thrust improvements that far exceeded the capabilities of the pulsejet, owing to the turbojet’s ability to improve pressurization of the incoming air before combustion. Recent renewed interest in pulsejets has been driven by miniaturized designs. A pulsejet combustor measuring 8 cm in length, operating at nearly 1200 Hz, and providing a maximum average thrust of 0.19 lbs was developed by Kiker (2005). Using scaling laws from larger pulsejet engines they were able to develop a valveless mini-pulsejet which can function with one of three different intake configurations (Kiker 2005; Geng, Zheng et al. 2007). Kiker also mentioned an operational 4.5 cm pulsejet which used platinum coated combustor for surface catalysis, though no data was published on this configuration. A 2 cm reed valve operated micro-pulsejet was investigated numerically by Wan (2005). Their findings yielded that the minimum pressure is unaffected by the scaling which is critical to the reed valve opening, but it was found that boundary layers from the wall occupies a significant portion of the cross-section and affects the rarefaction wave that is critical to generate sufficiently low enough minimum pressure to open its reed valves.

Pulsed denotation engines (PDE) also use the concept of resonant frequency combustion, but utilize a significant increase in power that is associated with the formation of a denotation wave. While pulsejets are normally based on a deflagration wave which travels subsonically, a denotation wave propagates at supersonic speed and is a very efficient means for burning air/fuel mixture in its ability to obtain substantial increases in pressure and temperature compared to deflagration. Numerous methods for exploiting the power generation associated with the formation of denotation waves have been explored. However, practical configurations have yet to be applied outside the laboratory, and the numerical analyses have been more encouraging than experimental results (Kailasanath 2000). Beck and Cutler (2004) and Cutler et al. (2005) reported a combustion-based actuator which uses a PDE to create a pulsed jet at an actuation frequency of 1500 Hz using a motor-driven rotary valve which controls the intake of hydrogen and air. The drawback of this configuration is the large size combustion chamber combined with high energy input for the mechanical valve which too bulky and costly for many flow control applications.

2.4 Earlier COMPACT Development

The early COMPACT configuration that was developed at Georgia Tech was based on premixed combustion where the fuel and oxidizer were mixed prior to injection into the combustion chamber (Crittenden 2003). This is analogous to a carbureted internal combustion engine where the mixing is accomplished within the intake before the mixture is drawn into the cylinder. Much of the work done in this field was

demonstrated in the Ph.D. thesis work of Crittenden (2003). Here, the focus was on a proof of concept prototype that illustrates the characteristics of the premixed combustion actuator's performance over a range of operating parameters. Research results summarized the effects of the fuel type, equivalence ratio, Φ , orifice diameter, d , chamber aspect ratio, H/D , chamber volume, V , mixture flow rate, Q , and actuation frequency, f .

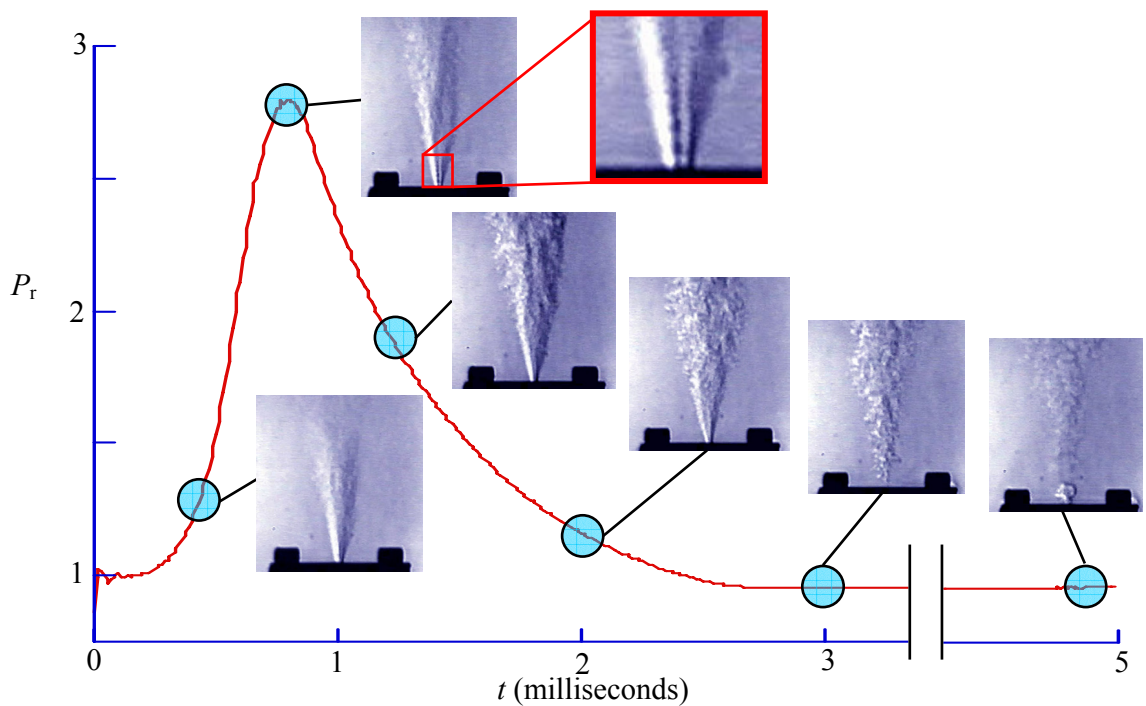


Figure 2.1: Phase-averaged chamber pressure with phase-locked Schlieren images of exhaust jet ($V = 1$ cc, $H/D = 1.27$, hydrogen/air premixed $\Phi = 0.62$, $d = 1.3$ mm, $Q = 50$ cc/s, and $f = 30$ hz)

Figure 2.1 illustrates the evolution of the combustion cycle of the combustion actuator where the time history of the normalized chamber pressure ($P_r \equiv P/P_a$) following ignition (at $t = 0$). This figure also contains phase-locked Schlieren images of the exhaust jet of a 1cc combustion chamber during the cycle. The images are recorded at $t = 0.44, 0.70, 1.20, 2.00, 3.00,$ and 4.80 ms following the spark trigger (using a $125 \mu\text{s}$ shutter speed) and the streamwise field of view is approximately 25 orifice diameters ($d = 1.30$ mm). After the spark is fired, there is a sharp rise in chamber pressure, culminating to approximately 2.8 atm at 0.7 ms. This results in a jet forming from the exhaust as soon as the pressure is on the rise, strengthening as the pressure increases and becoming choked once the P_r is above 1.9. Shock cells can be seen in the jet during peak pressure, signifying the sonic velocities. Following the peak, the pressure starts to decrease as the combustion process is completed. Note that the rise time of the pressure pulse is faster than the fall time (0.7 ms rise time compared to 1.3 ms fall). At $t = 2.7$ ms, the chamber pressure returns to atmospheric levels and the jet stops emanating from the orifice. At $t = 4.8$ ms, a small vortex ring appears, followed by a low-velocity steady jet, indicating returned flow of fuel/air mixture initiating the refilling of the chamber. The lag time signifies the effect of the passive fluidic resistance element that is designed to stop the flow of the fuel/air mixture during combustion.

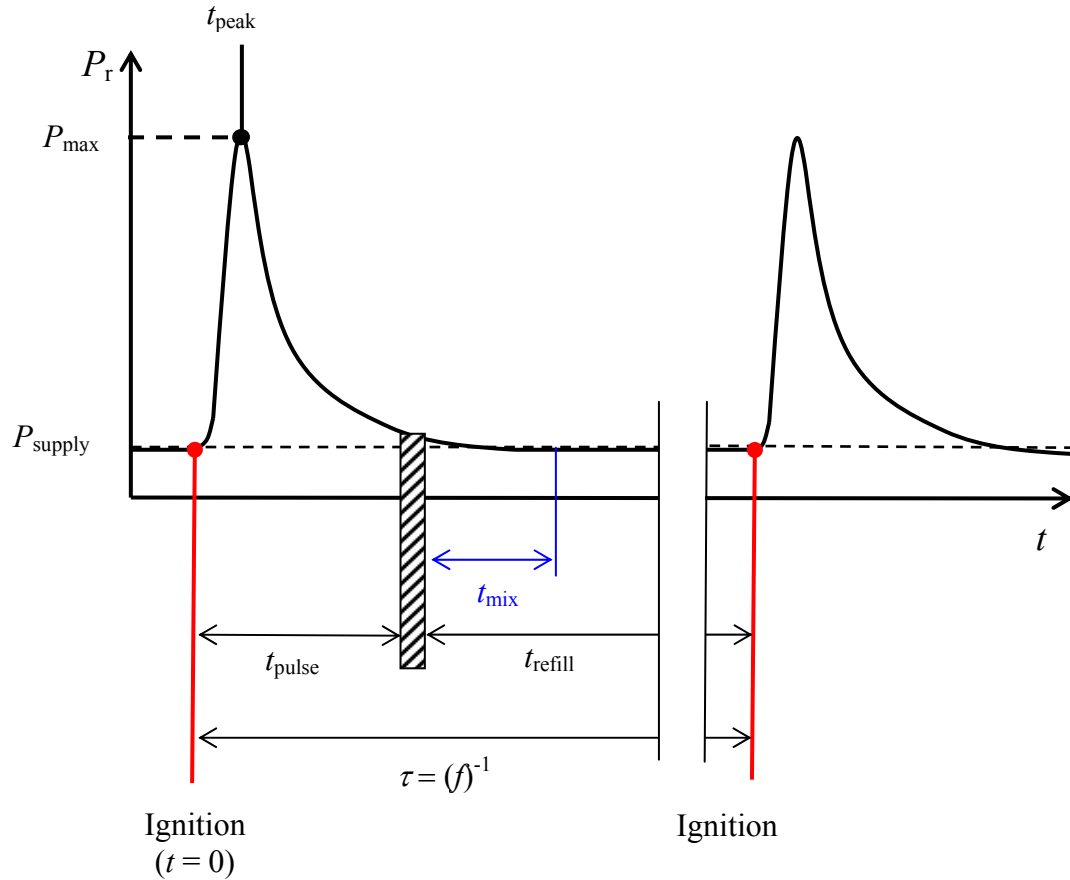


Figure 2.2: Generic pressure-time history of combustion powered actuator including t_{mix} for nonpremixed operation

The shape of the pressure curve is characterized by the peak pressure P_{max} , rise time to peak pressure t_{peak} , pulse duration t_{pulse} , and refill time t_{refill} (Figure 2.2). The mixing time t_{mix} , which is an important characteristic of a nonpremixed combustion actuator, is more difficult to quantify and was originally thought to be a performance impediment of a nonpremixed actuator.

CHAPTER 3

EXPERIMENTAL SETUP

3.1 Combustion Chamber

The combustion chamber for COMPACT is the central component of the actuator where the mixture is injected, ignited, and expands to build enough pressure to create a momentary high-velocity jet. As shown in Figure 3.1a-c, fuel and oxidizer (in the present cases air) can be injected into the chamber either in a premixed or nonpremixed configuration. For the premixed configuration (Figure 3.1a), air and fuel are mixed upstream of the chamber, and the mixture then passes through the passive fluidic resistance element regulating its flow during operation. There are two nonpremixed configurations, the first uses the passive fluidic resistance element on the fuel feed line only, and the air is injected directly into the chamber through a choked orifice with no regulating element. The second nonpremixed configuration involves direction injection both air and fuel through separate orifices (Figure 3.1c) without the resistance element (where the air orifice typically choked). In the direction injection configuration, the combustion burns all the available fuel in the chamber and the flame is then extinguished before the incoming fuel and air can form an ignitable mixture.

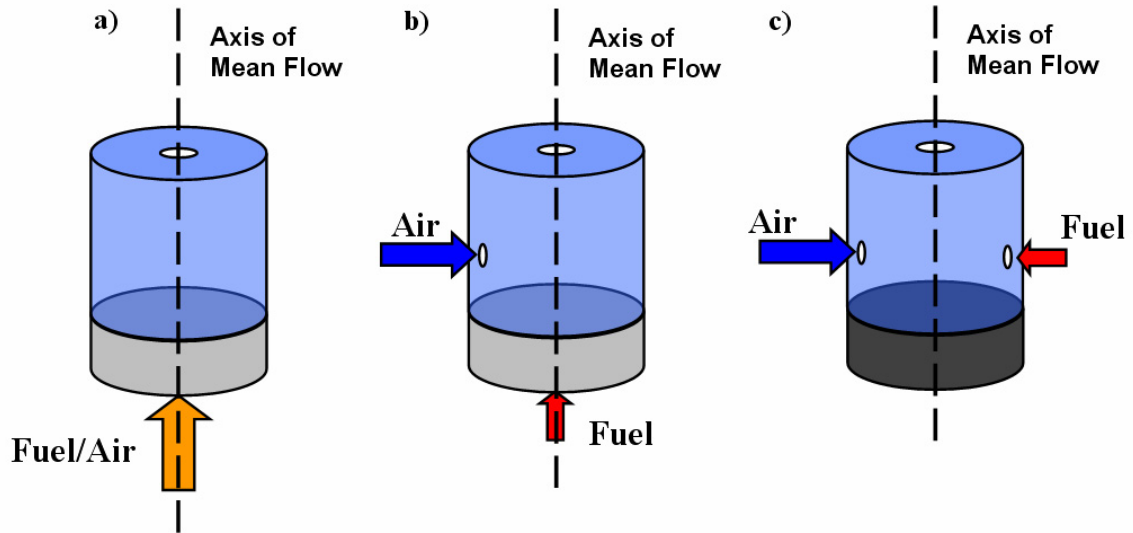


Figure 3.1: Fuel injection configurations of premixed (a), nonpremixed (b), and direct injection (c).

The chamber can be altered in shape and size to suit the required integration of the actuator. In the present investigation, all of the combustion chambers are cylindrical in design (unless noted otherwise). Figure 3.2 illustrates the general dimensions that are used to describe the combustor; chamber height, H , chamber diameter, D , exhaust orifice diameter, d , igniter position, l (distance from exhaust plate), and inlet locations for air and fuel, l_a and l_f respectively. Other system variations within the combustion chamber that are discussed in Ch. 5 include the spark location, number of spark ignition sources, inlet locations of air and/or fuel, and exhaust shape. Also shown in Figure 3.2 is the sintered metal and laser cut orifice grid used for the fuel injection regulator in most configurations. For combustors using direct injection of fuel, the sintered metal and orifice grid are replaced with a solid lower plate and two separate orifices are used to inject the air and fuel from opposite sides of the chamber (this configuration is discussed in more detail in Ch. 5).

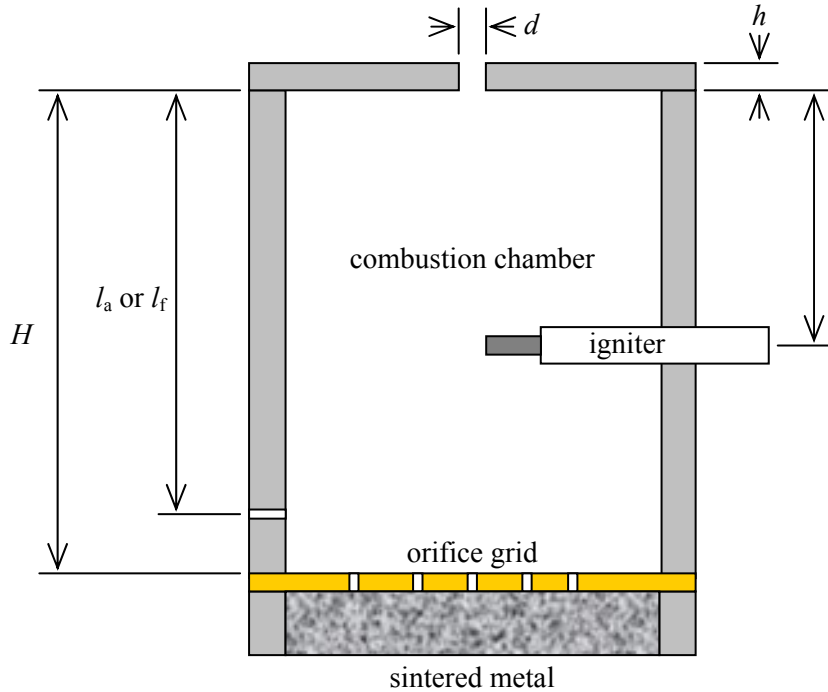


Figure 3.2: Diagram of COMPACT combustion chamber with chamber dimensions

An assembly of interchangeable aluminum combustion chambers and exhaust orifices was designed to attach to a common base-mount to hold the chamber during experiments. The base-mount can be used as a feed source of reactants to the combustion chamber, and can also house the fluidic resistance element if needed.

The two fuels tested were commercially available high purity hydrogen and propane. Compressed air from a local building source was used as oxidizer. The flow rates Q of air and fuel were measured individually using Aalborg thermal mass flowmeters calibrated for the specified gas (typical accuracy of 1%). Needle valves regulate the flow of the air and fuel separately to allow for control of the equivalence ratio, Φ , within the limits of the flowmeters' accuracy. In the premixed configuration, the

two streams are mixed upstream of the combustion chamber in a bed of glass beads and then delivered to the combustion chamber through the integrated fluidic element. For the nonpremixed chamber, both lines are injected into the chamber separately, and the mixing occurs within the chamber.

The reactants are ignited by an integrated small-scale spark plug with a gap distance of approximately 1-2 mm. In most cases, the spark plug is made of two wires housed in separate ceramic inserts and are electrically isolated from the chamber wall. In all cases, the spark's orientation is normal to the axis of the chamber and the mean direction of flow. Unless noted otherwise, a single spark was used centered about the chamber's axis of symmetry at elevation $l/H = 0.5$. In the nonpremixed operation, fuel is injected into the chamber axially opposite to the exhaust orifice through the fluidic element and orifice grid, the air is injected within a plane that is normal to the chamber axis, parallel to the chamber diameter at $r/R = 0.5$, as shown in Figure 3.3. The spark is generated by a standard automotive ignition system (Bosch ignition coil and 12V power supply) with a commercial electronic ignition control circuit triggered by a TTL signal, the frequency and duration of which are controlled by a digital LabVIEW interface.

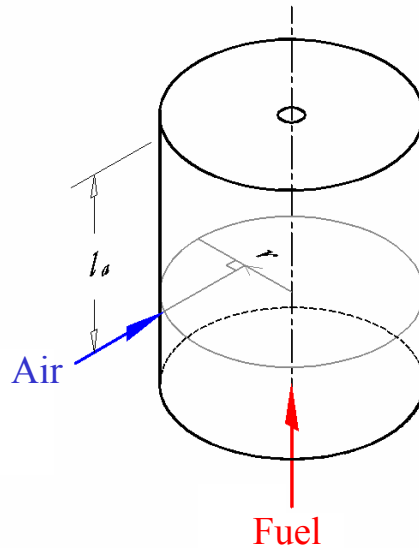


Figure 3.3: Simple air injection configuration schematic

Control of the spark duration is important when to minimize the effects of electromagnetic noise associated with the spark. The spark TTL trigger typically has a duty cycle of 1-5% for hydrogen. For heavier, less combustible fuel mixtures, a longer spark duration is required to produce enough energy to initiate combustion.

3.2 Data Acquisition

The pressure within the combustion chamber is the primary measure of the system's performance. Dynamic pressure measurements are obtained with a high-temperature, piezoresistive pressure transducer (Kulite model XTEH-7L-190M-100A) with a natural frequency response of 380 kHz, an operation temperature range of -65°F to

+750°F (-55°C to +400°C), and a compensated temperature range of +80°F to 650°F (+25°C to +343°C). Given the high flame temperatures of hydrogen and propane (about 2400°K at stoichiometric mixtures with reactants at STP), the mean exhaust temperatures at high operating frequencies can be as high as 720°F (380°C), thus a water-cooled housing jacket for the pressure transducer was designed to keep it within its compensated temperature range. The transducer output is sampled at 100 kHz with a National Instruments analog/digital data acquisition board using the TTL spark ignition signal as a timing reference. Each data set is phase-averaged over 50 realizations.

3.3 Flame Photography

Details of the flame propagation are captured using a 2cc, square base combustion chamber where one wall is made of pyrex (Figure 3.4). The chamber is made of aluminum and is black anodized. Though it is a square chamber, it was designed to closely resemble a 2cc cylindrical chamber (similar height, H , and width, W) with the air injection port positioned to induce swirl within the chamber. It is designed for premixed or nonpremixed operation with the air inlet is located at $l_a/H = 0.8$ and offset at $W/4$ from the center.

A standard CCD camera (768 by 464 pixels) having a shutter speed of 125 μ s is used to capture sample images of propane flame. A sequence of images captured at different instances during the combustion cycle is created using the vertical sync signal

from the camera and a desired time delay to trigger the spark. Propane fuel was used for the visualization of the flame because the hydrogen fuel burns in the ultraviolet and can not be visualized with the available camera. In addition to flame photography, the windowed chamber shown in Figure 3.4 was also used to test the operation of micro fabricated reed valves that were used as an alternative system of managing the inflow of reactants.

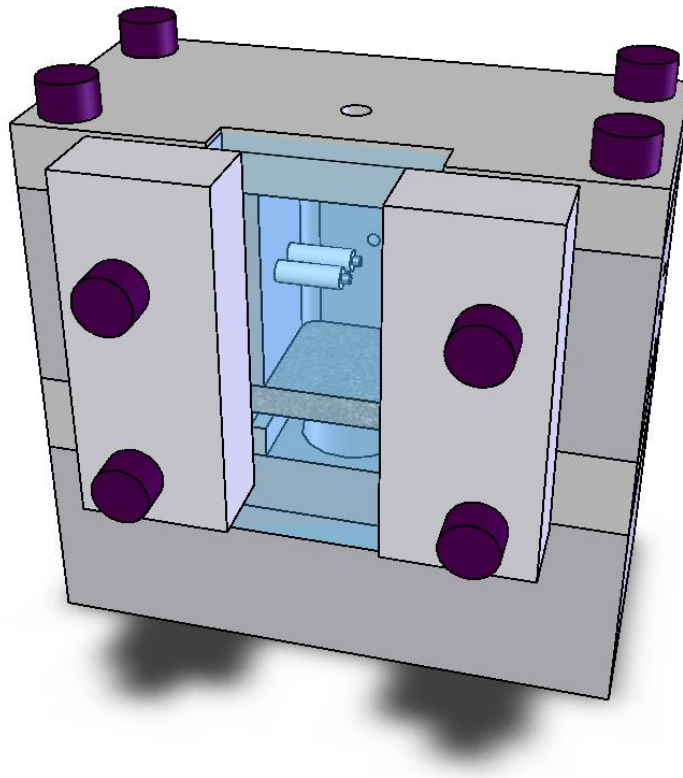


Figure 3.4: A 2cc windowed chamber for flame photography.

CHAPTER 4

PREMIXED AND NONPREMIXED COMBUSTOR CONFIGURATIONS

This chapter compares the performance of premixed and nonpremixed chamber combustor setups. Section 4.1 describes the differences in the chamber design and discusses the effects of nonpremixed fuel and small-scale mixing in the chamber, and consequently on the flame speed. Section 4.2 describes a parametric study that illustrates the differences between the nonpremixed and premixed actuator designs.

4.1 Global Difference in Premixed and Nonpremixed combustors

While a premixed COMPACT design requires only one air/fuel feed-line, its performance is limited by its burn rate of fuel. The need for using flame arrestors in the feed line can be eliminated by separating the fuel and air lines. In the nonpremixed combustion chamber, mixing of the fuel/air occurs within the chamber prior to ignition and, unlike the premixed configuration, requires two feed-lines and additional time for mixing (see section 2.4). The independent control of the flow in the nonpremixed design allows the ability to manipulate small-scale motions within the combustion chamber by exploiting the shear flow induced by the fuel and oxidizer streams. Thereby influencing

the evolution of the flame front and resulting in better mixing and concurrently faster combustion by exploiting wrinkling and lacerating of the flame front, effectively increasing its surface area and the burn rate. This can result in higher pressures and potentially shorter pulse duration and therefore higher actuation frequencies. Similar to the premixed configuration, only one fluidic resistance element is needed to regulate flow by regulating one feed line.

The flame within the combustion chamber must be initiated and extinguished repetitively for high-speed actuator operation with adequate time to refill the chamber. Increasing the flame speed allows faster combustion (and heat release) and therefore effectively decreases the pulse duration, t_{pulse} (the time from ignition until pressure is restored near pre-combustion levels, Figure 2.2). The flame speed depends on the burn characteristics of the mixture as well as the transport properties of the mixing. When considering non-turbulent flame (as in much of the thesis work of Crittenden 2003) with a laminar flame speed, S_L , the flame propagation velocity depends solely on the mixture's thermal and chemical properties where the transport properties are controlled by molecular diffusion through mass diffusion, momentum diffusion, and/or heat diffusion which are inherently slow. In order to burn faster (necessary for higher actuation frequencies), increased mixing is needed and obtained through small-scale mixing driven by stirring between the jets of fuel and air in nonpremixed configurations. Air is injected at sonic speeds with a Reynolds number as high as 90,000. These macro-motions created through eddy currents increase the turbulent transport by increasing the surface area of the mixing streams with increasing the temperature gradient between interfaces (Turns

2000). Evidence of the “turbulent” flame front is visualized with the presence of flame perturbation and irregular flame propagation (see Figure 4.5).

As discussed by Peters (Peters 1999), turbulent flame speed, S_T , can be significantly faster than laminar flame speed, S_L (Turns 2000)

$$S_L = \left[-2\alpha(v+1) \frac{\bar{m}_F}{\rho_u} \right]^{1/2} \quad \text{Eq. 4.1}$$

Laminar flame speed is a function of the thermal diffusivity α , the flow velocity v , unburned density ρ_u , and the average reaction rate of the combustion process \bar{m}_F . Where as turbulent flame speed (Peters 1999)

$$\frac{S_T}{S_L} = 1 + C \left[\frac{v'_{rms}}{S_L} \right]^n \quad (\text{commonly } C = 3.5 \text{ and } n = 0.7 \text{ for } \frac{v'_{rms}}{S_L} \gg 1) \quad \text{Eq. 4.2}$$

also depends on the mean unburned gas velocity, v'_{rms} , which contributes significantly to the increase in velocity.

Clearing the cylinder of burned gases and filling it with a fresh mixture is also affected by nonpremixed designs. Due to the low ignition energy of the combustible mixture, autoignition can occur when fresh reactants enter the chamber in the presence of hot combustion products. By venting the hot combustion products through a preferential

internal flow path, autoignition can be reduced, leading to higher actuation frequencies and potentially a reduction in the dilution of the fuel with combustion products.

The advantages of nonpremixed combustion configurations are illustrated in Figure 4.1 in which the hydrogen powered combustor supplied with $Q = 6$ L/min at $\Phi = 0.41$ and a $d = 1.78$ mm with the nonpremixed configuration injects choked air at $r/R = 0.25$ and $l_a/L = 0.75$. To begin with, the chamber pressure is significantly higher at $P_r = 4.5$ for nonpremixed compared to $P_r = 3.4$ for premixed at $f = 1$ Hz. These data show that there is a noticeable increase in the rate of pressure rise due to faster flame speeds, resulting in a lower time to peak pressure, t_{peak} (0.7ms nonpremixed and 1.15ms premixed, and pulse duration, t_{pulse} (2.4ms nonpremixed and 2.85ms premixed). The faster rate of pressure increase is prevalent throughout the entire present operating range ($f = 1$ Hz, 35 Hz, and 55 Hz).

Figure 4.2 charts normalized peak pressures of against normalized operating frequencies, f/f_i (normalized actuation frequency indicating the operating frequency relative to the characteristic flow rate and chamber volume; $f_i \equiv Q/V$), for premixed and nonpremixed hydrogen powered combustors at $Q = 12$ and 6 L/min with $\Phi = 0.41$ and $d = 1.78$ mm. The nonpremixed chamber's increased performance in both peak pressure and actuation frequency where f increases from 95 Hz (premixed) to 105 Hz (nonpremixed) at $Q = 6$ L/min and from 150 Hz to 240 Hz at $Q = 12$ L/min.

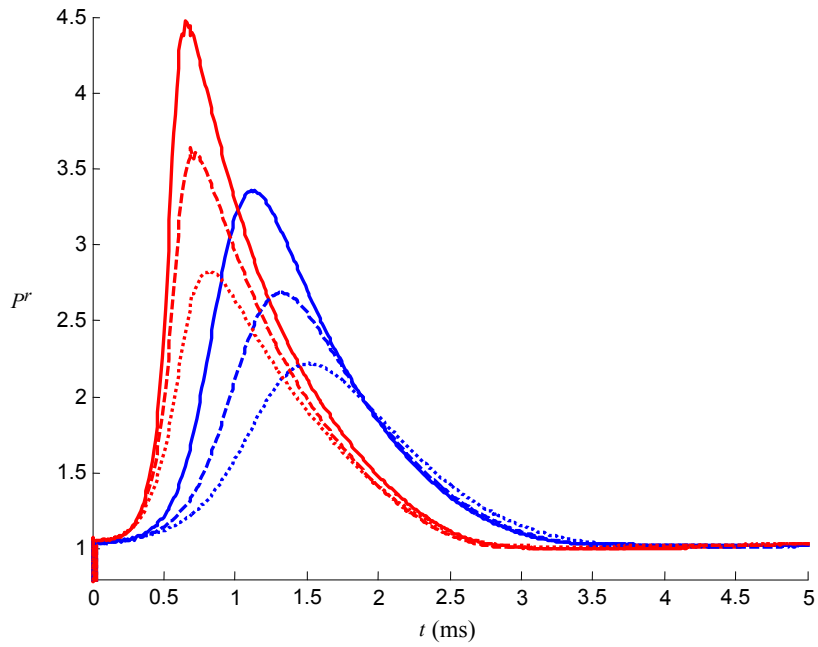


Figure 4.1: Premixed (—) and nonpremixed (—) pressure time history of hydrogen 2cc chamber, $Q = 6$ L/min, $\Phi = 0.41$, $d = 1.78$ mm, (—) 1 Hz, (---) 35 Hz, (····) 55 Hz.

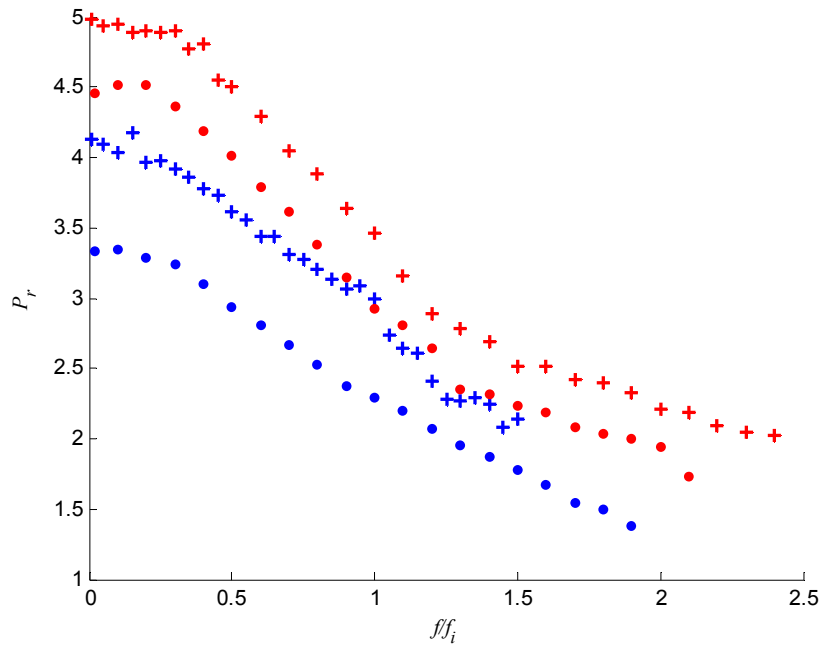


Figure 4.2: Peak pressure vs. f/f_i , of hydrogen 2cc, $Q = 12$ L/min premixed (+) and nonpremixed (+), $Q = 6$ L/min premixed (•) and nonpremixed (•), $\Phi = 0.41$, $d = 1.78$ mm.

Flame photography of premixed and nonpremixed propane combustion was taken to illustrate the differences in flame propagation. Figure 4.3 shows the pressure time history of this combustor used (as shown in Figure 3.4 with a square base combustion chamber) and circular markers denotes the segments which were captured with the flame photography. Such as the case with Figure 4.1, peak pressure increased with nonpremixed ($P_r = 1.8$ premixed and $P_r = 2.2$ nonpremixed) with a decrease in both t_{pulse} (3.7ms to 3.4ms) and t_{peak} (2.55ms to 2.15ms) in Figure 4.3. The sequence of flame images from these combustion processes are shown in Figure 4.4 for premixed and Figure 4.5 for nonpremixed. Both chamber configurations have the exhaust orifice (a simple circular orifice) centered at the top of the image frames. The premixed configuration (Figure 4.4) has the air/fuel mixture rising from the bottom of the frame toward the exhaust orifice at the top. Figure 4.4 shows the flame propagation, starting from the center and initially expanding vertically upwards and downwards at 1.8 ms (Figure 4.4b). Then there is a clear spreading towards the edges of the chamber through images at 2.5 ms (Figure 4.4c), 3.1 ms (Figure 4.4d), and 3.6 ms (Figure 4.4e) where the pressure peak is achieved. At 4.0 ms (Figure 4.4f), the flame begins to extinguish. At 4.7 and 5.3 ms (Figure 4.4g & h), the flame starts to be quenched and the pressure in the chamber drops below atmospheric level (see Figure 4.3), finally in Figure 4.4i the flame is extinguished and new reactants begin to enter the chamber.

Figure 4.5 is the corresponding sequence of images for the nonpremixed configuration. In this setup, the fuel flows from the bottom of the image, upwards, and air is injected from the right-hand side of the image frame (Figure 4.5) normal to the fuel

flow at $l_a/L = 0.8$ from the exhaust orifice at the top. The air orifice is positioned on the far side of the centerline, a distance of one-quarter the width of the chamber, to induce swirl. At 1.1 ms (Figure 4.5a), the spark has already started to ignite the mixture (earlier than the premixed chamber). At 1.8 ms (Figure 4.5b), the flame is advancing down and away from the air intake, and is driven by the air circulation. The flame then expands around the front of the chamber, spreading across the window at 2.5 and 3.1 ms (Figure 4.5c & d). Note the strong flame front at 3.1 ms (Figure 4.5d) which corresponds to the highest pressure reading. At 3.6 and 4.0 ms (Figure 4.5e & f), the flame strength is somewhat reduced as it wraps around the back of the chamber, and finally at 4.7 and 5.3 ms (Figure 4.5g & h), the low pressure within the chamber (see Figure 4.3) helps extinguish the flame and begin the refill process.

There are several significant features in the nonpremixed flame images that illustrate the increased pressure and higher actuation frequencies. With the air flow dominating the flame path (seen in Figure 4.5), the flame is drawn away from the incoming reactants sooner than what is shown in the premixed case (Figure 4.4), aiding in preventing autoignition (maximizing the distance between incoming reactants and the evacuating flame) and therefore allowing for higher frequencies. Also notice that the premixed flame is in contact with the walls of the chamber (Figure 4.4) longer than in the nonpremixed case (Figure 4.5). Less contact with the wall allows for less heat transfer loss and partly explains why there is a dramatic difference in the rate of pressure increase from the two configurations (Figure 4.3). Both premixed and nonpremixed flames have “wrinkles” in the flame suggesting non-laminar flame propagation. However, the

nonpremixed flame in Figure 4.5 shows more perturbations in the flame front and irregularity in its advancement within the chamber.

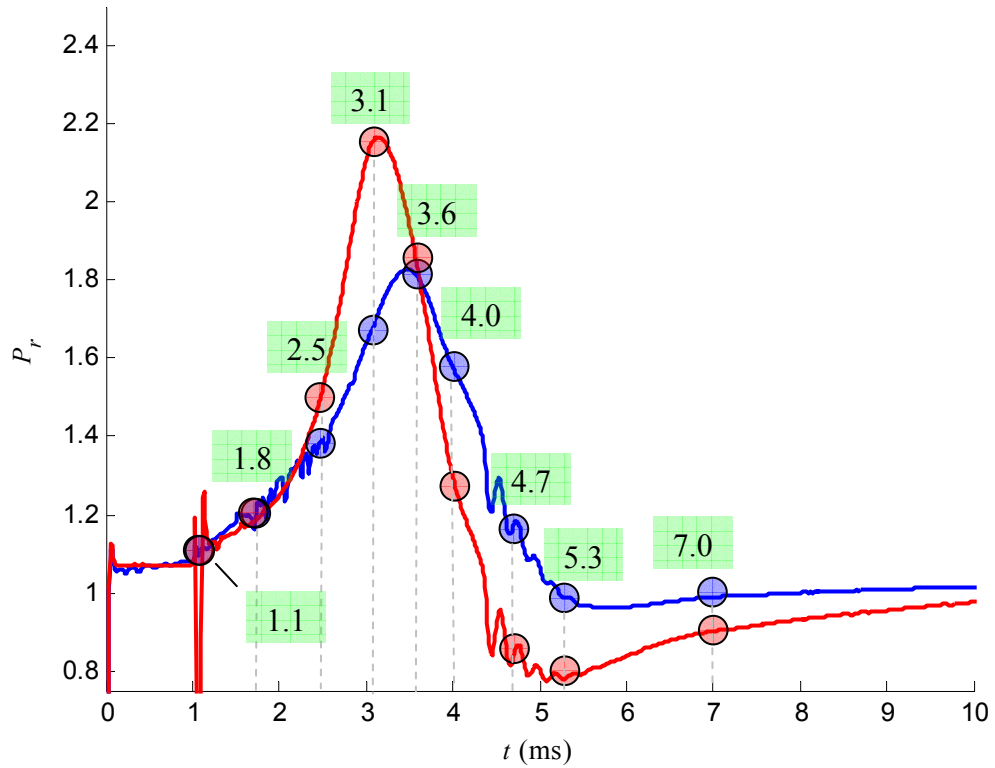


Figure 4.3: Premixed (—) and nonpremixed (—) pressure time history with photograph location; Propane, 2cc, $Q = 9\text{L/min}$, $\Phi = 1.0$, $d = 1.78\text{ mm}$, $f = 30\text{ Hz}$.

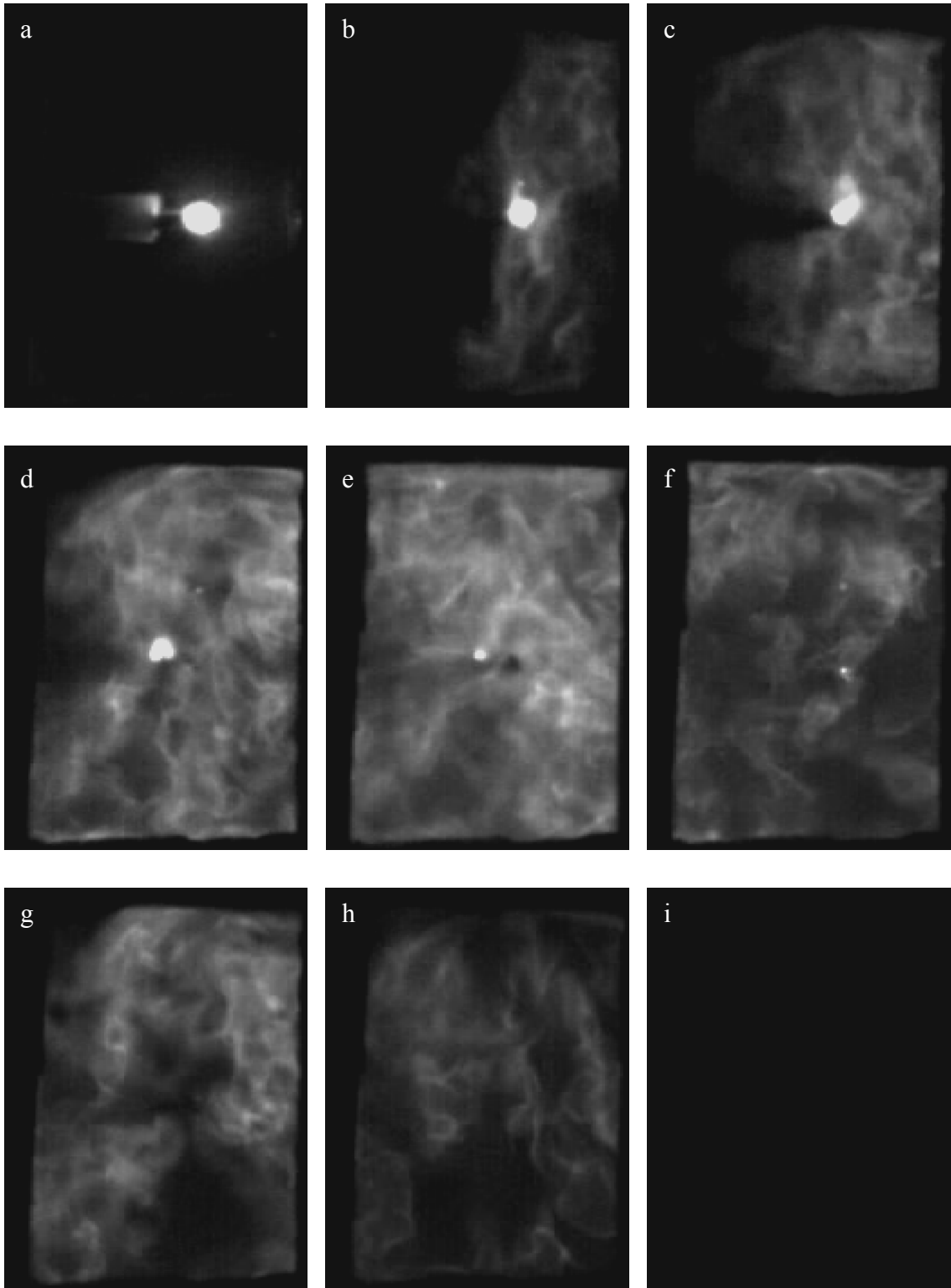


Figure 4.4: Premixed propane flame propagation, 2cc, $Q = 9/\text{min}$, $\Phi = 1.0$, $d = 1.78 \text{ mm}$, $f = 30 \text{ Hz}$ at $t = 1.1 \text{ ms}$ (a), 1.8 ms (b), 2.5 ms (c), 3.1ms (d), 3.6 ms (e), 4.0 ms (f), 4.7 ms (g), 5.3 ms (h), and 7.0 ms (i).

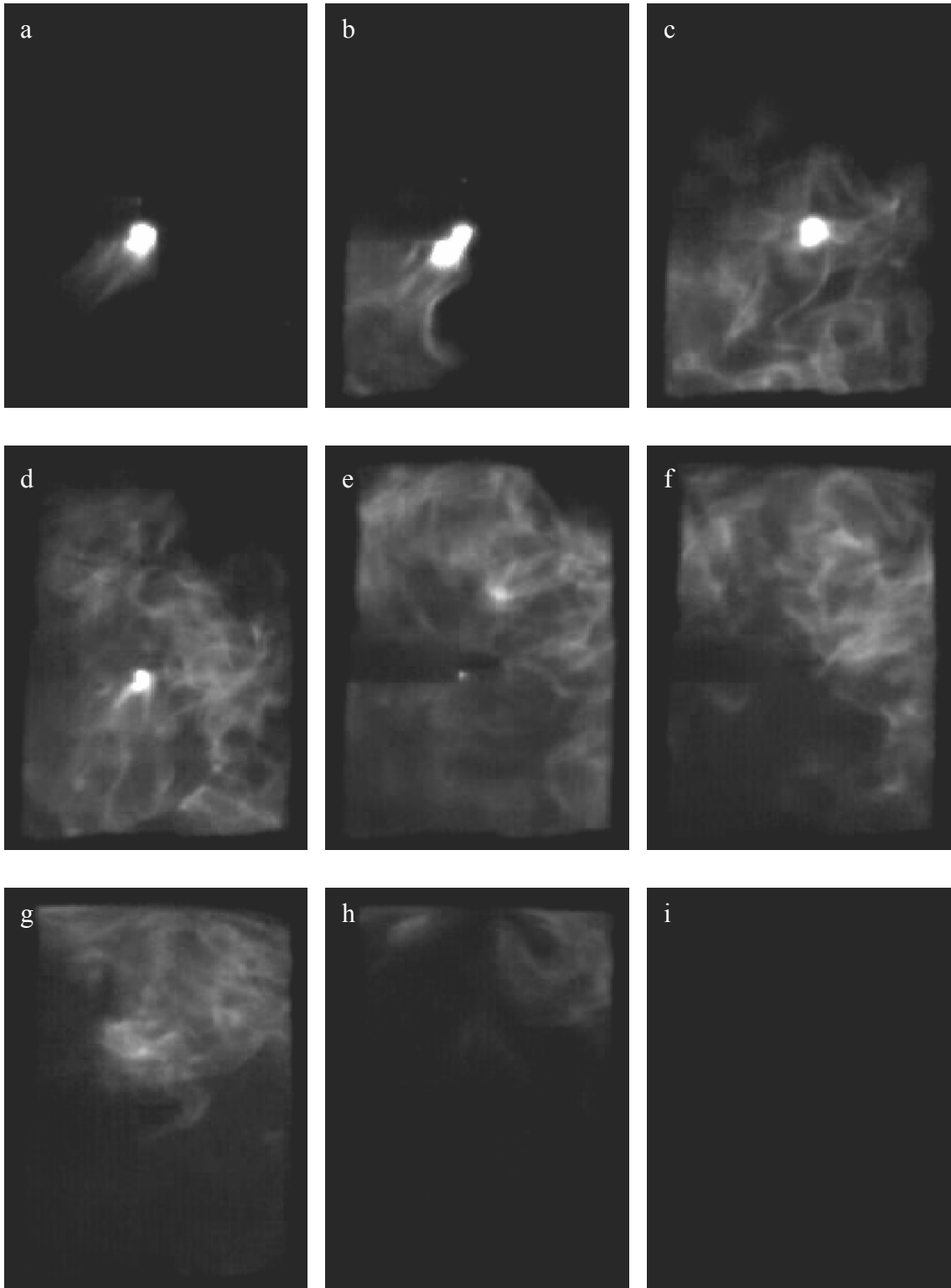


Figure 4.5: Nonpremixed propane flame propagation, 2cc, $Q = 9/\text{min}$, $\Phi = 1.0$, $d = 1.78$ mm, $f = 30$ Hz at $t = 1.1$ ms (a), 1.8 ms (b), 2.5 ms (c), 3.1ms (d), 3.6 ms (e), 4.0 ms (f), 4.7 ms (g), 5.3 ms (h), and 7.0 ms (i).

Quenching distance is defined as the critical diameter of a tube in which the flame extinguishes rather than propagating (Turns 2000). By igniting a premixed mixture of fuel and oxidizer in a conical tube, it is found that the reducing radius of the tube characteristically quenches the flame at a certain diameter, which is the quenching distance of the fuel/air mixture. Analysis has shown that the quenching distance is on the order of the flame thickness, and the quenching distance is a function of the fuel type, oxygen content (or equivalence ratio), temperature, and pressure. Hydrogen possesses the lowest of all common fuel types at 0.61 mm, Table 4.1, making it the optimal candidate for small scale combustion.

When engineering a small scale combustion chamber, the quenching distance becomes a key constraint. Designing a combustion chamber at the same order of magnitude as the quenching distance inherently yields high heat transfer loss, as discussed in Section 2.2. Basically, increased heat transfer minimizes the usable energy for generating a jet impulse, thus increasingly small combustion chambers could become less suitable for high speed flow control applications.

The equivalence ratio is defined as the number of moles-fuel over the number of moles-oxidizer (in this case air), relative to the stoichiometric mixture fuel/oxidizer ratio where $\Phi = 1$ (Heywood 1988).

$$\phi = \frac{\left(\frac{\text{fuel}}{\text{air}}\right)_{\text{actual}}}{\left(\frac{\text{fuel}}{\text{air}}\right)_{\text{stoich}}} \quad \text{Eq. 4.3}$$

Equivalence ratios greater than 1 specify a mixture with abundant fuel, or a rich mixture. Equivalence ratios less than 1 indicate a mixture abundant in air, or a lean mixture (Because rich mixtures are unlikely to be used in real applications where fuel supply is limited, tests were typically done with $\Phi \leq 1$).

4.2 Parametric Study of Nonpremixed and Premixed Combustor Configuration

This section discusses the effects of several primary parameters and the performance of COMPACT as measured by the pressure and actuation frequency. These parameters include fuel type, equivalence ratio, Φ , chamber aspect ratio, H/D , and exhaust orifice diameter, d .

4.2.1 Fuel Type and Equivalence Ratio

Perhaps the most critical system parameter is the type of fuel. Since fuel characteristics influence the actuator's performance and therefore may affect the design of the combustion chamber. In addition, a given fuel ratio enables substantial variations in the details of the combustion process and actuator performance. In the present experiments, only two types of fuel were used namely hydrogen and propane. Although for a given equivalence ratio the flame speed in propane/air mixture is slower than in hydrogen/air mixture, for constant volume combustion the pressure rise in propane/air combustion is higher than in hydrogen/air combustion. However, due to COMPACT's

open exhaust design, the combustion process is neither constant volume nor constant pressure. A hydrogen powered actuator generates more pressure than with propane fuel, primarily due to the substantially higher flame speed of hydrogen mixtures the maximum combustion frequency with propane is lower. These effects are evident in Figure 4.6 and Figure 4.7 which show the time history of normalized pressure for propane and hydrogen, respectively. These data show that for propane combustion the pressure peaks decrease while the characteristic rise time and overall combustion duration decrease compared to hydrogen. Additionally, the range of operable equivalence ratios is also shown. For propane a range from $0.74 \leq \Phi \leq 1.31$ while for hydrogen $0.32 \leq \Phi \leq 1.15$.

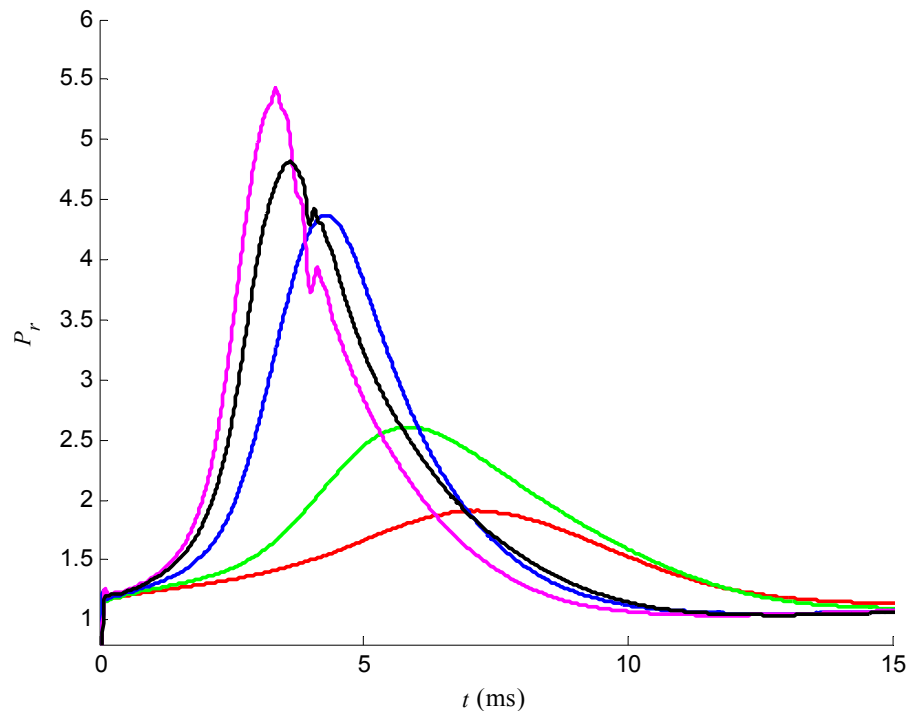


Figure 4.6: Nonpremixed propane combustion pressure time history with $\Phi = 0.74$ (—), 0.86 (—), 1.00 (—), 1.15 (—), 1.31 (—), $V = 2\text{cc}$, $Q = 4.8\text{ L/min}$, $d = 0.89\text{ mm}$, $f = 5\text{ Hz}$, $H/D = 1.25$.

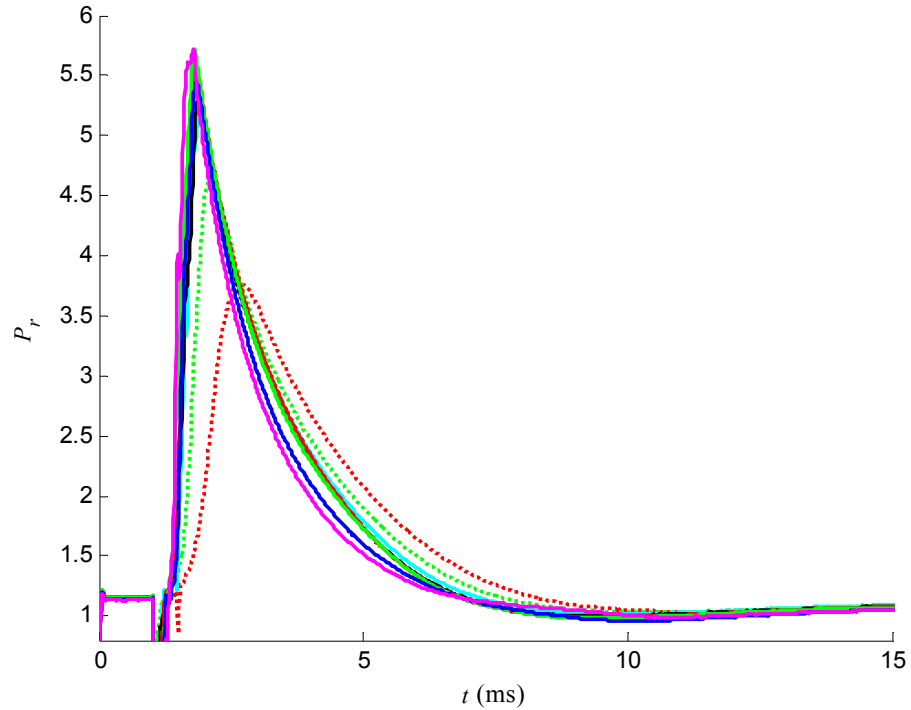


Figure 4.7: Nonpremixed hydrogen combustion pressure time history with $\Phi = 0.32$ (\cdots), 0.41 (\cdots), 0.51 (—), 0.62 (—), 0.74 (—), 0.86 (—), 1.00 (—), 1.15 (—), $V = 2\text{cc}$, $Q = 4.8$ L/min, $d = 0.89$ mm, $f = 5$ Hz, $H/D = 1.25$.

The critical combustion characteristics include: flame speed, flame temperature, flammability limits, and quenching distance. Each of these characteristics has an important role in the design of the actuator. Fuels with a narrow band of flammability limits are clearly more sensitive to an appropriate equivalence ratio. The present test results show that standard ideal flammability limits measured at STP (Table 4.1) don't fully match with the operational equivalence ratios in COMPACT. This mismatch is ostensibly the result of heat losses in the combustion chamber, mixing limitations, and variation in pressure. As shown in Table 4.1, decreases in equivalence ratio allow cooler operation of the combustion chamber but may cause quenching. Note that for pulsed

combustion the actuator temperature during operation is significantly lower than the flame temperature. As shown in Table 4.1, the flame speed of the fuel mixture characterizes the time it takes for the flame front to propagate from the spark to wall, where it is quenched. The higher the speed, the sooner the flame is quenched and the quicker the chamber can be refilled without autoignition. Thus, the flame speed plays an important role in determining the actuation frequency of the actuator. The flame speed is affected by the fuel type and the corresponding equivalence ratio in addition to pressure and temperature. However, it is also affected by the flow field characteristics within the chamber, in particular small-scale motions, as discussed in section 4.1.

Table 4.1: Fuel properties of Hydrogen and Propane (Turns 2000; Crittenden 2003).

Fuel Type	Flammability Limits (Φ , 1 atm)	Min. ignition Energy (10 ⁻⁵ J)	Quenching distance, min. (mm @ STP)	Equivalence Ratio (Φ)	Adiabatic Combustion	
					P =constant	
					Flame Temperature (K)	Flame Speed (S_L , cm/s)
Hydrogen	0.14-2.54	1.8	0.61	1.0	2432.4	210
				0.9	2340.4	190
				0.8	2201.5	150
				0.7	2034.9	125
				0.6	1849.8	90
				0.5	1648.0	60
				0.4	1428.7	35
Propane	0.51-2.83	26.0	1.8	1.0	2395.5	44
				0.9	2235.6	39
				0.8	2068.2	32
				0.7	1892.4	23
				0.6	1707.4	15

Figure 4.8 illustrates the benefit of nonpremixed hydrogen combustion over corresponding premixed combustion for different equivalence ratios. As noted in section 4.1, nonpremixed combustion is characterized by small-scale mixing, resulting in higher flame speed and higher pressures. As also shown in Figure 4.6, and Figure 4.7, an increased equivalence ratio results in an increased pressure with shorter t_{pulse} and t_{peak} . It is also noteworthy that while at low equivalence ratio ($\Phi < 1$) the rise time of the nonpremixed combustion is faster, this trend reverses at higher equivalence ratios

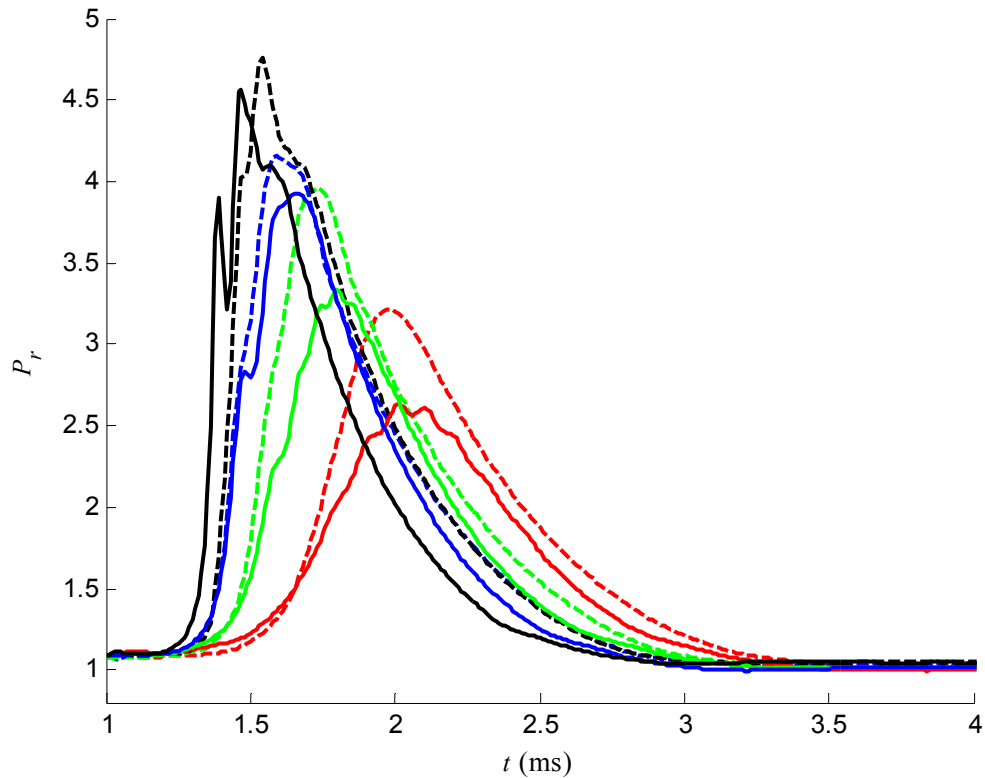


Figure 4.8: Premixed (—) and Nonpremixed (---) pressure time history at $\Phi = 0.32$ (—), 0.41 (—), 0.51 (—), 0.74 (—), 2cc, $Q = 14\text{L/min}$, $d = 1.98\text{ mm}$, $f = 20\text{ Hz}$.

4.2.2 Combustion Frequency

COMPACT is designed such that the actuation frequency is controlled by the ignition system, allowing for a high degree of controllability. As discussed in section 2.4, the combustion cycle has two primary stages, combustion (during t_{pulse}) and refill (during t_{refill}). For a given chamber volume, V , and flow rate, Q , the idealized time needed to refill the chamber (or residence time) is defined as V/Q and therefore the ideal combustion frequency is $f_i = Q/V$. This frequency is used for comparison to the actual performance (through the nondimensional ratio f/f_i). The variation of the maximum pressure ratio with f/f_i is shown in Figure 4.9. For $0 < f/f_i < 1$, there is enough time for the chamber to refill

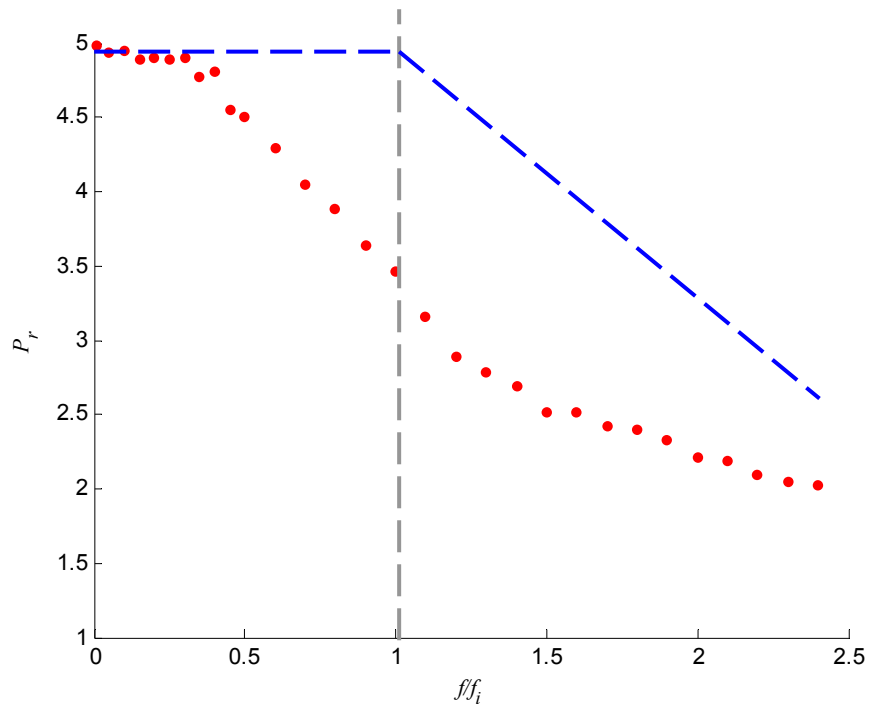


Figure 4.9: Peak pressure vs. normalized actuation frequency, comparing ideal performance (---) to measured performance (\bullet). $V = 2\text{cc}$, $Q = 12\text{ L/min}$, $\Phi = 0.41$, $d = 1.78\text{ mm}$.

completely such that chamber pressures during combustion is close to the peak levels of a fully replenished chamber. For $f/f_i > 1$, only a fraction of the reactants enter the chamber, mixing with remnants of the combustion products and lowering the effective mixture ratio, and resulting in diminished chamber pressures. However, as shown in Figure 4.9, the point of diminishing chamber pressures starts for $f/f_i < 1$.

Mixing of combustion products with fresh reactants within the combustion chamber is more prominent by the increased pulse duration relative to the cycle duration (t_{pulse}/τ) as f increases and the response time associated to the recommencement of reactants inflow. At low actuation frequency, the available refill time, t_{refill} , is longer than the pulse duration, t_{pulse} . With a typical t_{pulse} of 2.5 ms, at $f = 10$ Hz t_{refill} is nearly 40 times greater, but at 200 Hz, t_{refill} is the same as the t_{pulse} . The higher actuation frequencies result in more overflow of the chamber with new fuel and air, thus more exhaust products are mixed with the new reactants, decreasing the effective equivalence ratio seen within the combustion chamber. In addition to the percentage increase of the combustion time, the flow field characteristics of the chamber play a significant role in the venting of the exhaust gases. During the combustion pulse, the high chamber pressure cuts off the mixture inflow and the high-velocity jet carries out some of the combustion products. After combustion, the relatively weak inflow of reactants returns and aids in the process of venting out the rest of the products in a process called scavenging (similar to what occurs in a 2-stroke engine). The inflow of reactants contributes significantly to the chamber's flow field characteristics. Inflow velocity and the turbulent structures it creates determine how well the exhaust gases are vented. The response time for the flow to

resume after combustion is a large factor in the refilling of the chamber. A slow response time may cause misfires or weak combustion from the lack of effective scavenging and too quick of a response time can cause autoignition.

The pressure time history in Figure 4.1 illustrates the effect of increased actuation frequency. There is a clear decrease in the peak pressure with the higher actuation frequencies as more exhaust products combine with the incoming reactants, creating a less powerful mixture. This leads to a decrease in the rate of pressure rise at the higher frequencies resulting in a longer t_{peak} while leaving t_{pulse} relatively unchanged. The increase in t_{peak} is much more significant in the premixed configuration than the nonpremixed configuration, as a result of a higher flame speed. Figure 4.2 shows that the higher flame speed and preferential internal flow path of air seen in Figure 4.4 and Figure 4.5 are responsible for increased actuation frequencies for the nonpremixed compared to the premixed configuration.

4.2.3 Chamber Volume

The chamber of the combustion powered actuator can vary with size and shape depending on application, which is one of the attributes of this type of actuator that makes it so versatile. The present investigation has focused primarily on cylindrical combustion chambers because of their ease of manufacture and low surface area to volume ratio. As discussed in Section 2.2, low A_s/V improves the combustion efficiency by minimizing the amount of heat transfer loss. Table 4.2 includes A_s/V for the six

different chambers tested and includes a spherical chamber for comparison (lowest A_s/V). The table shows that smaller combustion chambers have increasingly higher A_s/V , making it more susceptible to heat losses. For consistency, all of the combustion chambers used in this section have an aspect ratio of $H/D = 1.27$.

Table 4.2: Surface area to volume ratio given various volumes and aspect ratio

V (cc)	H/D	D (cm)	A_s (cm ²)	A_s/V
0.25	1.27	0.6305	2.2105	8.8419
0.50	1.27	0.7944	3.5089	7.0178
0.75	1.27	0.9093	4.5980	6.1307
1.00	1.27	1.0008	5.5701	5.5701
2.00	1.27	1.2610	8.8419	4.4210
2.00	2.27	1.0391	9.3952	4.6976
2.00	Sphere	1.5632	7.6766	3.8383

Figure 4.10a and b shows the variation of pressure time history with combustor volume for premixed and nonpremixed combustion chambers, respectively. The flow rate was held at 4 L/min and the chart shows the combustion pulses at $f = 10$ Hz, thus the $f/f_i = 0.0375, 0.075, 0.11, 0.15, 0.30$ for chambers 0.25cc-2cc respectively. In the premixed chamber (Figure 4.10a) an increase in volume yields an increase in pressure, with volume as the total chemical energy release increases. However, this trend reverses as the chamber volume is increased to 2cc ostensibly because of the change in f/f_i (since the replenishing frequency is kept unchanged). It is also remarkable that the rate of pressure rise is relatively unaltered, leading to a slight increase in the time to peak pressure, t_{peak} , with increasing volume as the pressures increases. The increase in volume also results in

longer pulses, t_{pulse} , because more expanding products must be vented through the exhaust orifice.

The nonpremixed operation (Figure 4.10b) shows an increase in the peak pressure compared to the premixed combustion for all volumes tested. However, in Figure 4.10b the change in pressure with varying volumes is less noticeable (at least at 10 Hz). Similar to the premixed case, there is a decrease in t_{pulse} and t_{peak} with a smaller chamber volume. However, unlike the premixed case, the decrease in t_{peak} is attributed to an increase in the rate of pressure rise, suggesting an increase in flame speed for smaller volume chambers. This may be possible due to turbulent mixing streams comprising a higher percentage of the chamber when volumes decrease. These data suggest that in a low chamber volume, small-scale mixing between the fuel and oxidizer becomes more significant.

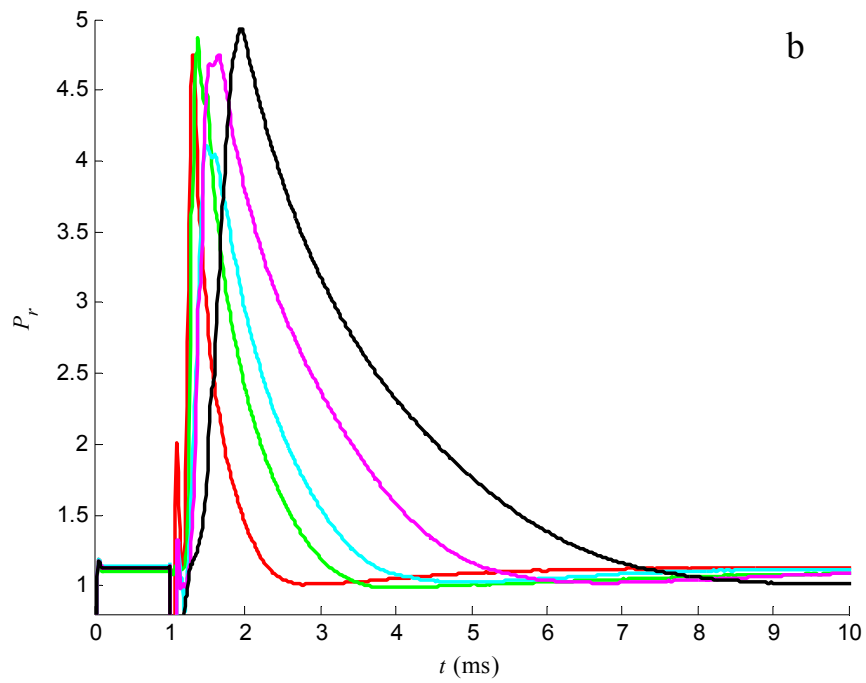
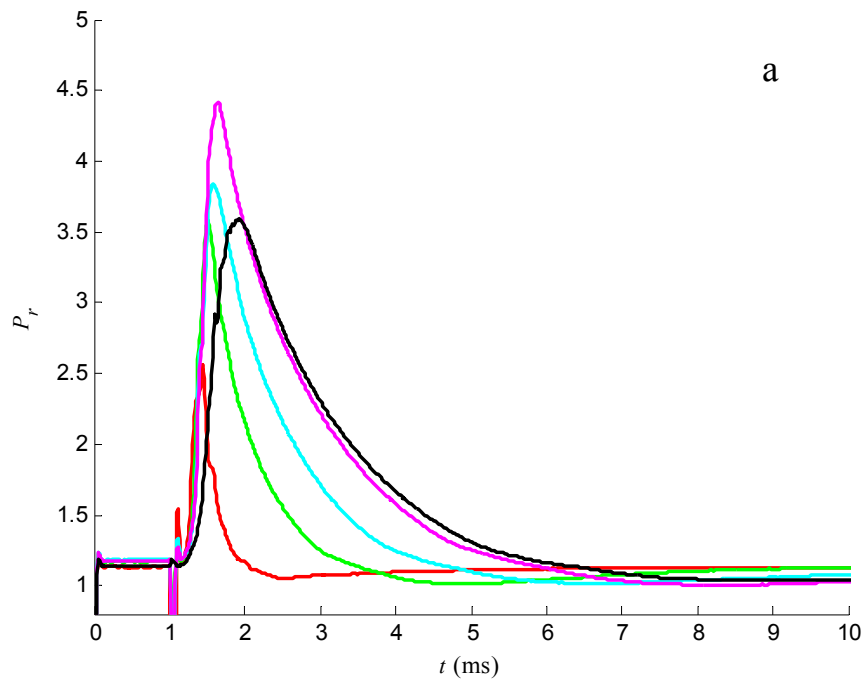


Figure 4.10: Pressure time history, premixed (a) and nonpremixed (b) hydrogen $V = 0.25\text{cc}$ (—), 0.50cc (—), 0.75cc (—), 1.00cc (—), 2cc (—), ignition spark is fired at 1 ms , $Q = 4\text{ L/min}$, $\Phi = 0.51$, $d = 0.89\text{ mm}$, $f = 10\text{ Hz}$.

4.2.4 Flow Rates

The mixture flow rate, Q , is the sum of both fuel and oxidizer flow rates into the combustion chamber. The relative fuel and oxidizer flow rates are determined by the mixture's equivalence ratio. Operating the actuator at higher frequencies necessitates more frequent refill of the combustion chamber, and therefore higher flow rates. As the flow rate increases, the gas speed within the chamber also increases, affecting the speed of the bulk flow and the rate of mixing between the fuel and oxidizer jets that can alter the flame's behavior.

Figure 4.11 shows the pressure time history of an actuator at three different flow rates for the premixed and nonpremixed configurations. These pressures are measured at $f = 10$ Hz, or $f/f_i = 0.250, 0.167, 0.125$ with respective flow rates of 4.8, 7.2, 9.6 L/min. Increasing flow rates result in higher rates of pressure increase along with higher peak pressures ($P_r = 3.75, 4.5, 4.8$ for premixed and $P_r = 4.2, 4.7, 4.9$ for nonpremixed at $Q = 4.8, 7.2, \text{ and } 9.6$ L/min respectively), as a result of higher flame speed due to the mixing enhancement and more complete venting of combustion products. It is also possible that a small increase in pre-pressurization of the combustion chamber contributes to the increased pressure peak. It is also noteworthy that the nonpremixed flow appears to have a longer pulse duration than the premixed case for this chamber design. The pulse duration does not vary substantially at the different nonpremixed flow rates ($t_{\text{pulse}} = 2.75$ ms) as it does in the premixed configuration ($t_{\text{pulse}} = 2.5, 2.3, \text{ and } 2.25$ ms for $Q = 4.8, 7.2, \text{ and } 9.6$ L/min respectively).

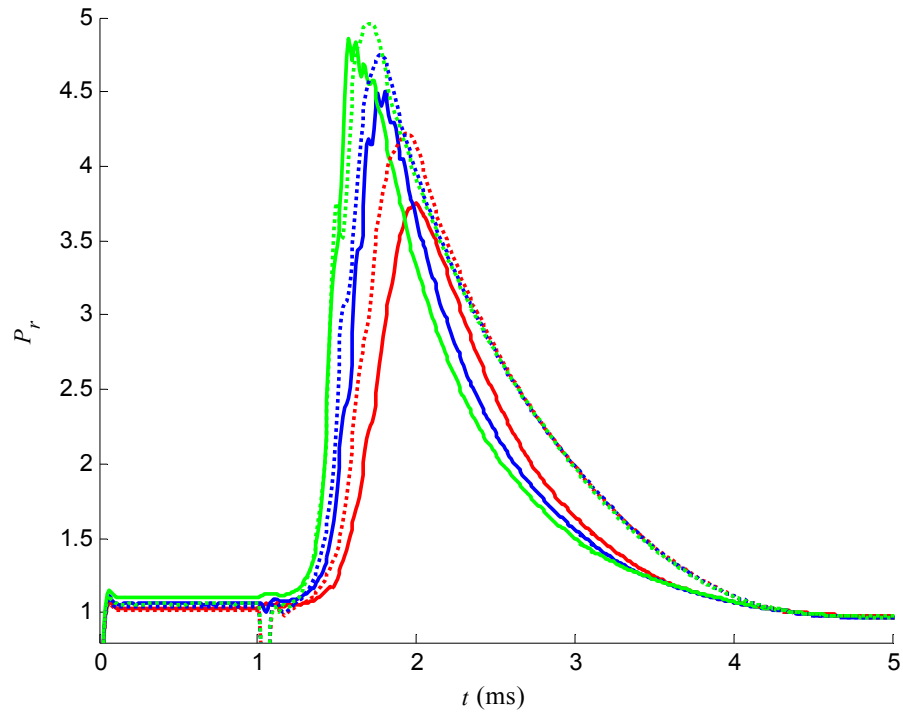


Figure 4.11: Pressure time history of premixed (—) and nonpremixed (⋯) hydrogen combustion with $Q = 4.80$ L/min (—), 7.20 L/min (—), 9.60 L/min (—), ignition spark at 1 ms, $V = 2$ cc, $\Phi = 0.51$, $d = 1.50$ mm, $f = 10$ Hz, $H/D = 1.25$.

It has been observed that with an increased in f there is a need to increase the velocities of the inflowing reactants to maintain the flow rate. Increasing f results in an increase in the mean back pressure observed by the passive fluidic resistance element. In order to maintain flow rates, compensation on the upstream pressure must be made.

4.2.5 Exhaust Orifice Diameter

Changing the exhaust orifice diameter alters the flow field characteristics of the combustion chamber by adjusting the amount of restriction and pressure drop of the

exhaust flow. Decreasing the orifice diameter increases the flow restriction, resulting in marginally higher pre-pressurization of the combustion chamber leading to higher peak chamber pressures. Under these conditions, more time is required for the chamber pressure to equalize following combustion (t_{pulse}) which can adversely affect high operating frequency and slow down the refill phase.

Figure 4.12 shows the pressure time history of a COMPACT using three different exhaust orifices operating in both premixed and nonpremixed configurations. There is a significant increase in pressure and rate of pressure increase with the nonpremixed configuration compared to the premixed across all orifice diameters. For both configurations, an increase in orifice diameter results in a decrease in pressure and a decrease in t_{pulse} . Interestingly, the rate of pressure rise for the nonpremixed flow appears to be less affected by changes in orifice diameter than the premixed configuration, ostensibly as a result of the small-scale mixing and higher flame speeds within the nonpremixed chamber.

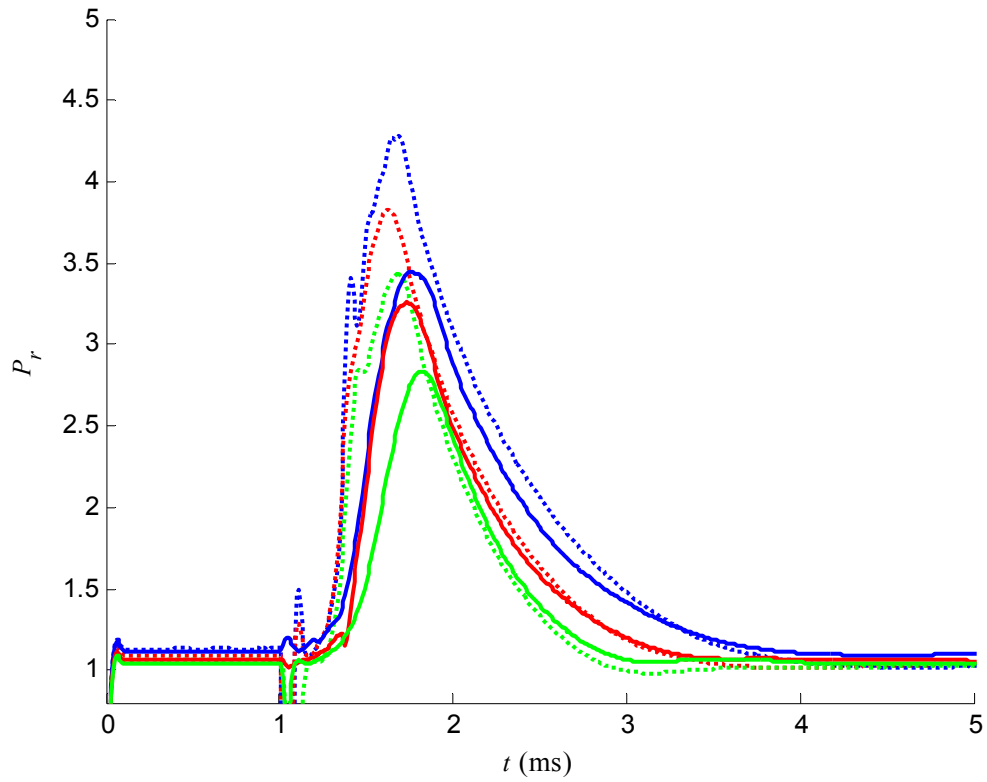


Figure 4.12: Pressure time history of premixed (—) and nonpremixed (---) hydrogen combustion with $d = 1.61$ mm (—), 1.98 mm (—), 2.21 mm (—), ignition spark at 1 ms, $V = 2$ cc, $Q = 18$ L/min, $\Phi = 0.37$, $f = 10$ Hz, $H/D = 2.27$.

CHAPTER 5

OPTIMIZATION OF OPERATING FREQUENCY

Earlier sections have demonstrated the advantages of nonpremixed COMPACT configurations. For applications in high-speed flow control it is necessary for the actuator to develop high impulse at high operating frequencies. As discussed in section 2.4, the initial development of COMPACT resulted in substantial impulse, but at relatively low operating frequencies. Significant frequency improvement is necessary for effective high-speed flow control. This section focuses on the optimization of these performance criteria in terms of the primary actuator parameters for extension of the operating frequency of COMPACT while maintaining high impulse.

There are three primary factors that affect and can limit the actuation frequency: mixing within the combustion chamber, misfires, and autoignition following combustion. Misfires, or combustion failure following ignition, occurs when there is inadequate mixture of reactants near the spark, thus hampering its ability to initiate a reaction. This is likely to occur when the desired actuation frequency exceeds the ideal actuation frequency or $f/f_i > 1$ and may be caused by inefficient mixing and venting of combustion products. Autoignition occurs when the air and fuel mixture ignites before the spark ignition due to hot spots or hot gases that remain within the combustor (note that the minimum ignition energy of H₂/air is 1.8E-5 J, more than 14 times smaller than C₃H₈/air at 26.0E-5 J (Turns 2000)). Autoignition results in uncontrollable continuous flame and

the actuator loses its time-dependent functionality. The presence of the continuous flame heats the chamber to significantly higher temperatures than pulsed combustion.

The characteristic of the flow field affects both the global large scale transport of fuel and oxidizer and the evolution of small-scale mixing. The ability for uniform mixing decreases when $f/f_i > 1$. Since the time available for mixing decreases, as a result Φ varies both spatially and temporally. The mixing process is further complicated by the presence of combustion products which must be exhausted and can lead to local dilution of the fuel/oxidizer mixture.

5.1 Flow Field Characteristics

5.1.1 Fuel & Equivalence Ratio

As noted in chapter 4, the two types of fuel used in the present investigation are hydrogen and propane. At STP, hydrogen has a wider range of flammability limits than propane ($\Phi_{\text{H}_2} = 0.14\text{--}2.54$ vs. $\Phi_{\text{C}_3\text{H}_8} = 0.51\text{--}2.83$) and can burn much leaner fuel mixtures (see Table 4.1). Figure 5.1a & b show the variation of the peak combustor pressure with characteristic operating frequencies for propane and hydrogen, respectively, for a range of equivalence ratios. These data show that the operating frequency for hydrogen is inherently higher than for propane, and that even near the upper limit for propane $f/f_i = 0.5$ the pressure peak for hydrogen is significantly higher at $P_r = 3.6$ vs. 4.75 with propane ($\Phi = 1.15$). Recall that while the flame temperatures of propane and hydrogen

are comparable, the laminar flame speed of hydrogen is significantly faster than that of propane (Table 4.1). The peak actuation frequency for hydrogen is $f/f_i = 3.4$ at very lean mixture ($\Phi = 0.41$) at which it reaches $P_r = 1.85$.

It is noteworthy that at high actuation frequencies the propane mixture frequently misfires over a wide range of equivalence ratios, while hydrogen mixtures typically misfire only at very lean mixtures ($\Phi < 0.51$). However, hydrogen tends to autoignite for $\Phi \geq 0.51$. For hydrogen, (Figure 5.1b) the pressure increases with equivalence ratio until $\Phi = 0.74$ and 0.86 where the increasingly rich mixtures leads to some pressure loss. Propane also experiences higher chamber pressures with higher equivalence ratios until $\Phi = 1.31$. However, note that for $\Phi = 1.31$ the propane mixture appears to achieve higher chamber pressures at high operating frequencies than $\Phi = 1.15$. This may be attributed to mixing with combustion products at higher frequencies which may help improve the flammability.

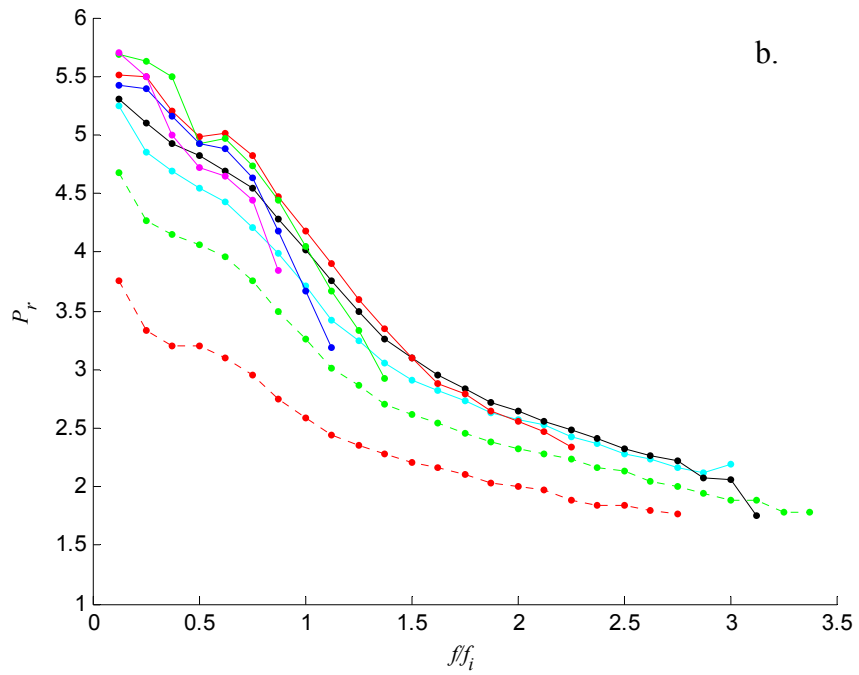
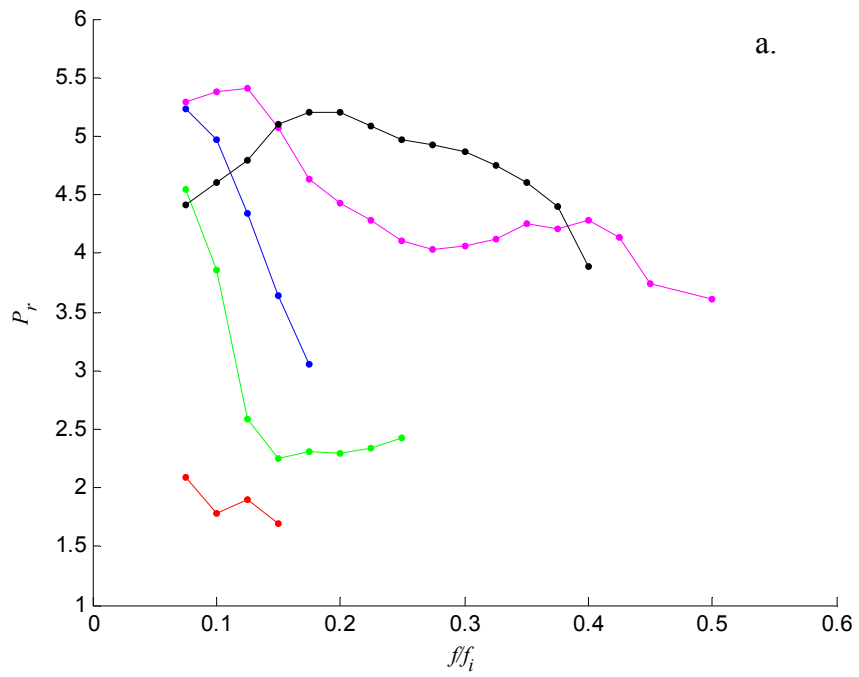


Figure 5.1: Peak pressure plot of propane mixture (a) and hydrogen mixture (b) with $\Phi = 0.32$ (\cdots), 0.41 (\cdots), 0.51 (---), 0.62 (---), 0.74 (---), 0.86 (---), 1.00 (---), 1.15 (---), $V = 2\text{cc}$, $Q = 4.8\text{ L/min}$, $d = 0.89\text{ mm}$, $H/D = 1.25$.

5.1.2 Combustion Frequency

As noted in section 2.4, during a combustion cycle of a combustion powered actuator the chamber pressure rises, exceeds the fuel line pressure and subsequently halts the flow of fuel. Air, which enters the chamber by direct injection (at sonic speed), is less affected by the increase in chamber pressure and continues to flow during most of this stage helping to shape the advancement of the flame front. The fuel flow resumes shortly after the chamber pressure drops below the line pressure and this marks the start of the refill stage. This stage is critical to insuring the occurrence of the next combustion cycle and the relatively low flow speed within the chamber during the refill stage can result in incomplete mixing and low equivalence ratios.

Figure 5.2 shows the effects of an increasing operational frequency on the complete pressure time history of a COMPACT for hydrogen with $\Phi = 0.51$. These data show that as f increases, the peak pressure diminishes, while pulse duration and time to peak pressure are almost invariant. Although t_{peak} remains virtually unchanged, the rate of pressure rise decreases, indicating a reduction in the burn rate. The drop in burn rate can be attributed to the change in the mixture's Φ_{eff} , as more combustion products remain in the combustion chamber at higher frequencies.

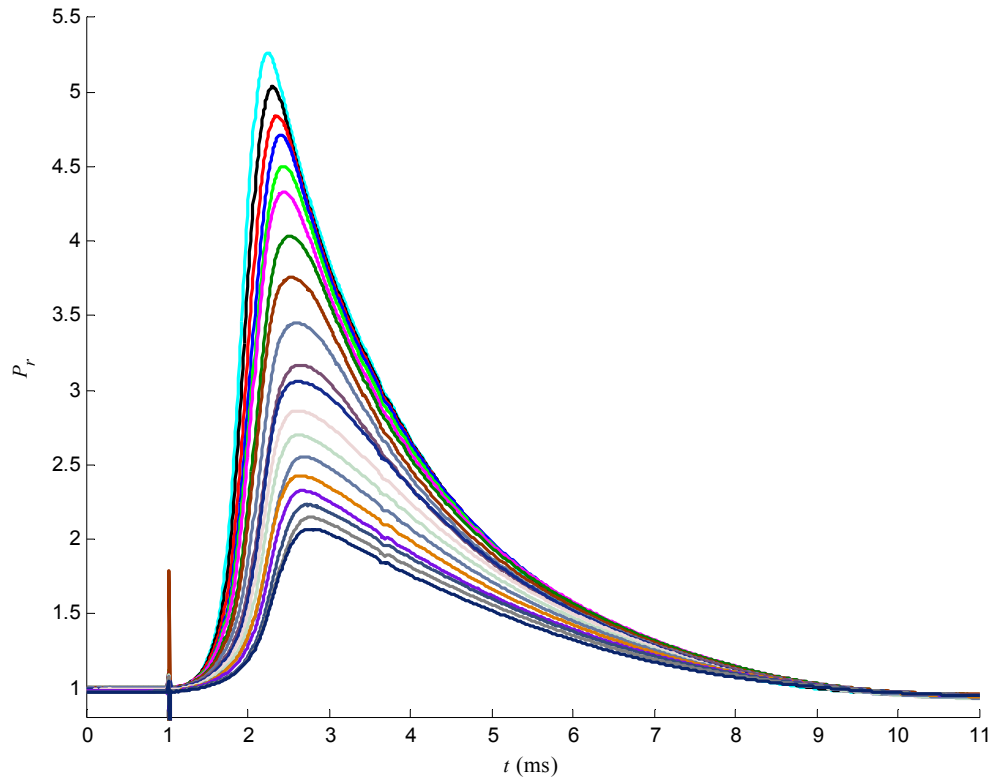


Figure 5.2: Pressure time history at $f/f_i = 0.10$ (—), 0.20 (—), 0.30 (—), 0.40 (—), 0.50 (—), 0.60 (—), 0.75 (—), 0.90 (—), 1.05 (—), 1.20 (—), 1.35 (—), 1.50 (—), 1.65 (—), 1.80 (—), 1.95 (—), 2.10 (—), 2.25 (—), 2.40 (—), 2.55 (—), ignition at 1 ms, $V = 2\text{cc}$, $Q = 2.4\text{ L/min}$, $d = 0.89\text{ mm}$, $\Phi = 0.51$, $H/D = 2.27$.

Since the fluidic resistance element relies on the magnitude of the chamber pressure to stop/start the fuel flow, the decrease in peak pressure at high actuation frequencies degrades its performance. However, at the same time the refill process can occur faster, although an early fuel flow can result in autoignition.

5.1.3 Variation of Actuator Impulse

The two primary parameters that affect the actuation impulse are the internal pressure and orifice diameter. Modification of the orifice area affects the combustor flow during both the combustion and refill stages of the cycle. A smaller orifice increases chamber pressures and raises the mean exhaust speed, but can result in lowering impulse and reduce the flow of the combustion products. Figure 5.3 shows how the pressure time history is affected by varying exhaust orifice diameter. As expected, these data show that the peak pressures increase as the exhaust orifice is reduced. However, there is also higher pressure during the refill before and after the pulse which leads to higher pre-ignition pressure which can affect the flame speed and reaction rate of the combustible mixture (Peters 1999; Turns 2000). It is noteworthy that the data do not show significant changes in the time to peak pressure and the burn rate. What is changing with the orifice diameter is the pulse duration t_{pulse} due to the change in resistance of outward flow and therefore for pressure relief.

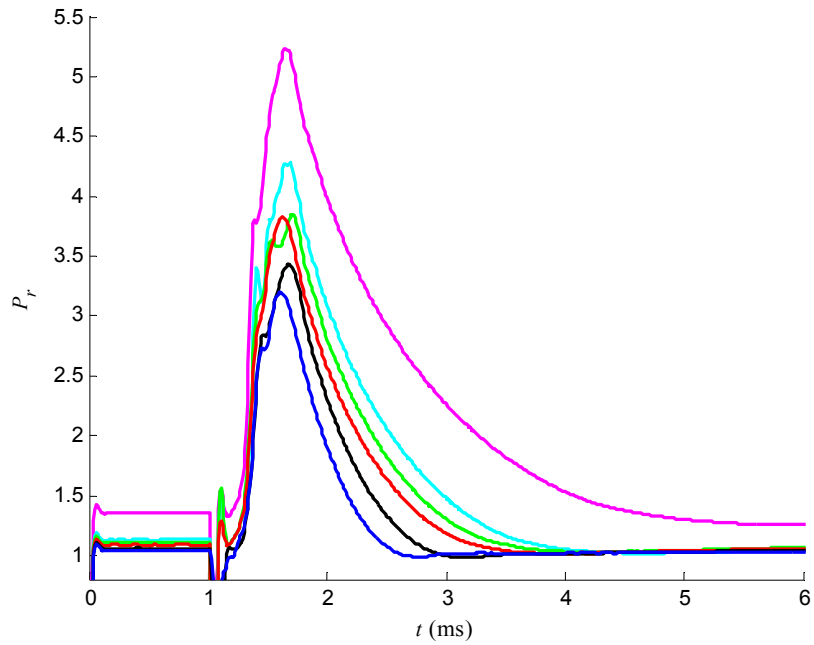


Figure 5.3: Pressure time history with $d = 1.50$ mm (—), 1.61 mm (—), 1.78 mm (—), 1.98 mm (—), 2.21 mm (—), 2.54 mm (—), spark initiated at 1 ms, $V = 2$ cc, $Q = 18$ L/min, $\Phi = 0.37$, $H/D = 2.27$, $h/d = 2$, $f = 10$ Hz.

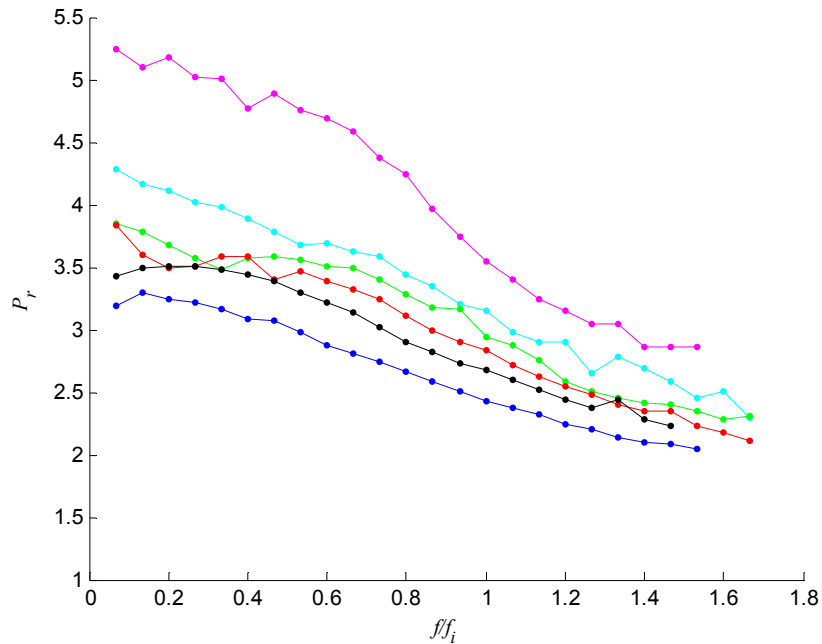


Figure 5.4: Peak Pressure with $d = 1.50$ mm (—), 1.61 mm (—), 1.78 mm (—), 1.98 mm (—), 2.21 mm (—), 2.54 mm (—), $V = 2$ cc, $Q = 18$ L/min, $\Phi = 0.37$, $H/D = 2.27$, $h/d = 2$.

Figure 5.4 shows the variation of the peak pressure with orifice diameter and actuation frequency. These data indicate that the highest peak pressures are obtained for $d = 1.5$ mm. At this diameter the rate of pressure decrease with frequency is faster than at the larger orifice diameters. While the data in Figure 5.4 show minimal variation of the maximum operating frequency on the jet diameter, it is important to recognize that the diameter does have a profound effect on the actuator performance. It is found that for a given set of operating conditions there is an optimal jet diameter. For orifices smaller than the optimal diameter, the actuator can misfire at lower frequencies due to higher chamber pressures that increase the lag-time for the fuel supply. While larger exhaust orifices can lead to autoignition at lower operating frequencies as the weaker chamber pressures reduced the lag-time, filling the chamber with fuel before the flame is extinguished.

With the assumption of isentropic compressible flow of an ideal gas, the pressure time history during the combustion cycle allows for an estimate of the impulse. Impulse, J (Eq. 5.1), is defined as the force integral over time (John 1969).

$$J = \int F dt \tag{Eq. 5.1}$$

The thrust, F , is calculated from the pressure within the chamber denoted as the stagnation pressure, P_t , and the area of the exhaust orifice, A (Eq. 5.2) where M is the

Mach number, P_e is the pressure at the exit plane, and P_b is the back pressure for which the jet pulse experiences after exiting the exhaust orifice.

$$F = [P_e M^2 \gamma + (P_e - P_b)] A \quad \text{Eq. 5.2}$$

For Mach number less than 1, exit plane pressure equals back pressure (Eq 5.3). Mach numbers greater than or equal to 1, P_e is directly proportional to stagnation pressure (Eq 5.4).

$$P_e = P_b \quad M < 1 \quad \text{Eq. 5.3}$$

$$\frac{P_e}{P_t} = 0.5283 \quad M \geq 1 \quad \text{Eq. 5.4}$$

The Mach number defined in Eq. 5.5 is based on the pressure ratio of stagnation pressure over back pressure and the specific heat ratio ($\gamma = 1.41$).

$$M = \sqrt{\frac{2}{\gamma - 1} \left[\left(\frac{P_t}{P_b} \right)^{\frac{\gamma - 1}{\gamma}} - 1 \right]} \quad \text{Eq. 5.5}$$

Using a simple exhaust orifice limits the exit velocity to the speed of sound, therefore the Mach number, M , is held at 1 for all calculations resulting supersonic speeds when $P_t/P_b > 1.89$ at STP (unless using a converging-diverging nozzle).

The computed variation of peak thrust with f/f_i is shown in Figure 5.5. These data show a reversed trend of the variation with orifice diameter compared to the data in Figure 5.4, where larger orifice diameters provide higher thrust despite the low pressures. The corresponding impulse is shown in Figure 5.6, where the pulse duration t_{pulse} begins at the time of ignition and concluded during pressure decrease at a pressure that is 5% of the peak pressure above the baseline (non-combustion) pressure. As expected, the impulse is higher at low actuation frequencies. For this case, the 1.50 mm orifice has a significantly higher impulse than any other orifice in this operating range

Figure 5.7 shows the gain in impulse using pulsed combustion relative to the steady flow of mixture without combustion (J/J_o). The data in Figure 5.7 are computed over the same period (t_{pulse}) as in Figure 5.6. The highest percent gain is for $d = 2.54$ mm, and all cases exhibit a decrease with increasing frequency.

Figure 5.8 shows the variation of the “total” impulse gain (J_t/J_o) over the entire actuation cycle τ compared with operating frequency. The orifice $d = 2.54$ mm has the highest percent gain in “total” impulse. Note that the “total” impulse increases with frequency approaching a peak value near $f/f_i = 0.9$. While at low frequencies the pulse duration represents a small fraction of the cycle period and therefore results in low gain, at high frequencies, the pulse duration is a higher fraction of the actuation period and leads to higher gain (or higher average momentum flux).

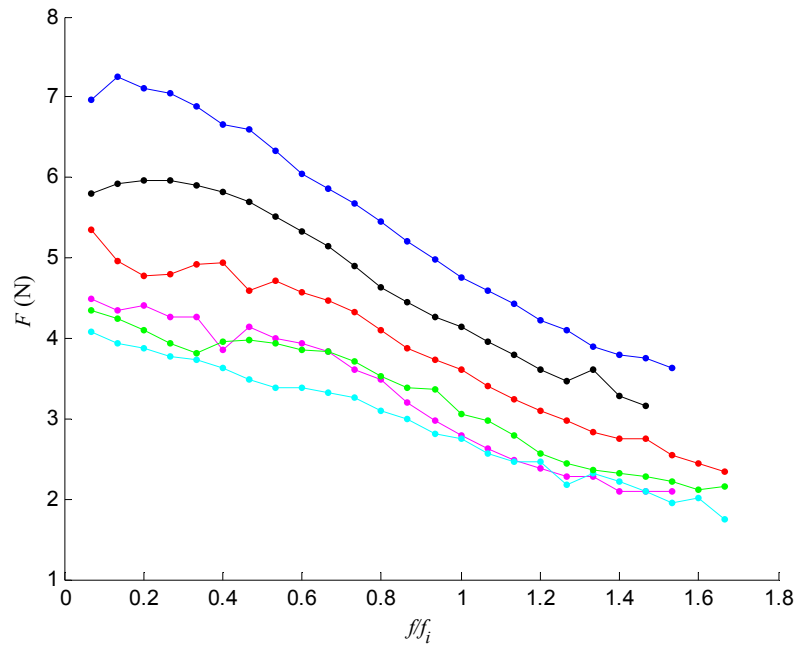


Figure 5.5: Peak thrust [N] with $d = 1.50$ mm (—), 1.61 mm (—), 1.78 mm (—), 1.98 mm (—), 2.21 mm (—), 2.54 mm (—), $V = 2$ cc, $Q = 18$ L/min, $\Phi = 0.37$, $H/D = 2.27$, $h/d = 2$.

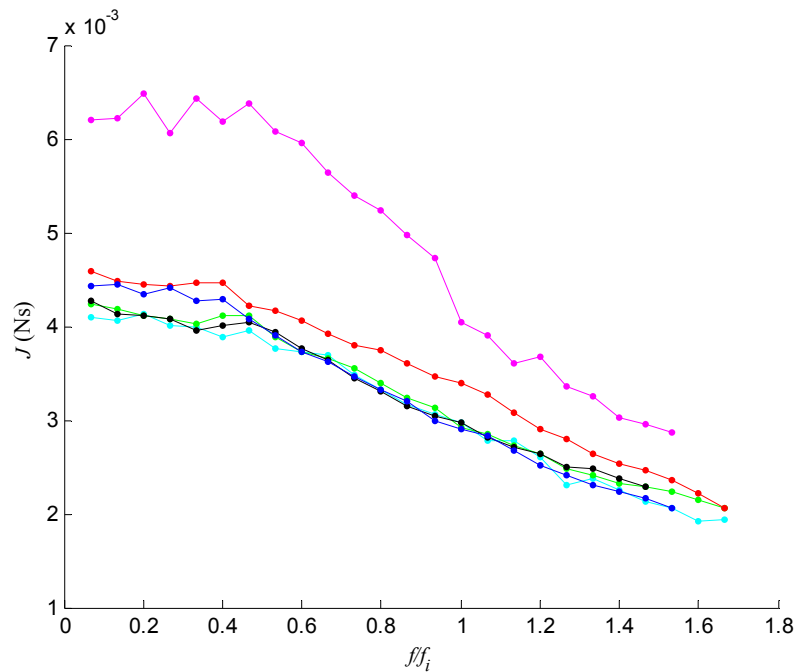


Figure 5.6: Impulse computed during t_{pulse} [N·s] with $d = 1.50$ mm (—), 1.61 mm (—), 1.78 mm (—), 1.98 mm (—), 2.21 mm (—), 2.54 mm (—), $V = 2$ cc, $Q = 18$ L/min, $\Phi = 0.37$, $H/D = 2.27$, $h/d = 2$.

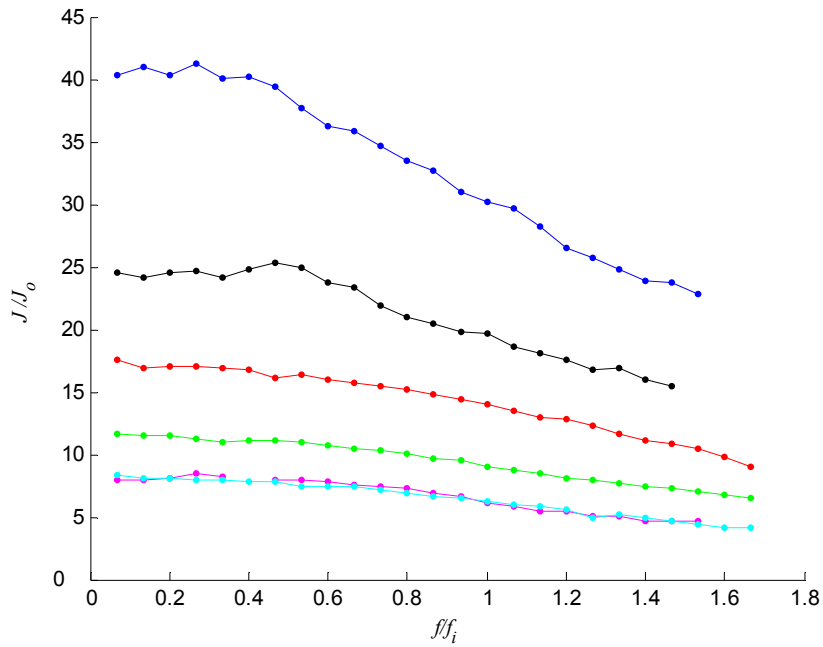


Figure 5.7: Impulse gain during t_{pulse} with $d = 1.50$ mm (—), 1.61 mm (—), 1.78 mm (—), 1.98 mm (—), 2.21 mm (—), 2.54 mm (—), $V = 2\text{cc}$, $Q = 18$ L/min, $\Phi = 0.37$, $H/D = 2.27$, $h/d = 2$.

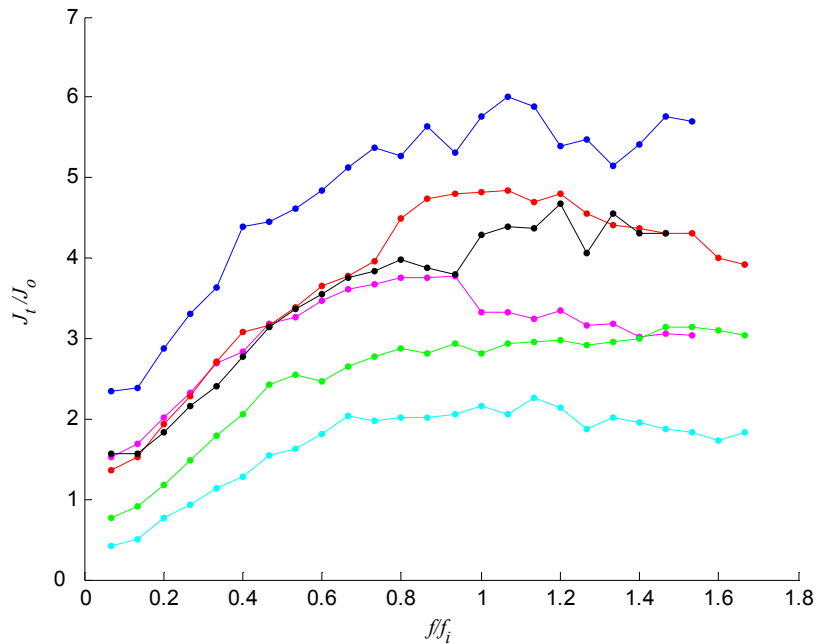


Figure 5.8: Impulse gain computed over τ with $d = 1.50$ mm (—), 1.61 mm (—), 1.78 mm (—), 1.98 mm (—), 2.21 mm (—), 2.54 mm (—), $V = 2\text{cc}$, $Q = 18$ L/min, $\Phi = 0.37$, $H/D = 2.27$, $h/d = 2$.

In addition to changes in the exhaust area, the effects of some modifications of the orifice shape on the exhaust flow are considered for a given area. These changes include the aspect ratio (h/d , as defined in Figure 3.2), orifice convergence and/or divergence. It is noted that for steady flow ($Re = 10,000$) through simple circular orifices of varying aspect ratios the minimum discharge coefficient occurs at $h/d \approx 2$ when a closed separation bubble forms on the inner surface of the orifice throat, and the losses associated with flow separation at the inlet are reduced (Fried and Idelchik 1989). For $h/d > 2$ the losses continue to increase due to viscous losses on the surface. Crittenden (2003) showed that at low actuation frequencies $h/d = 2$ leads to lower losses in the combustion actuator even though the flow is unsteady. However, as the actuation frequency increases, the effect of h/d decreases (Crittenden 2003). Similar results were found in the present

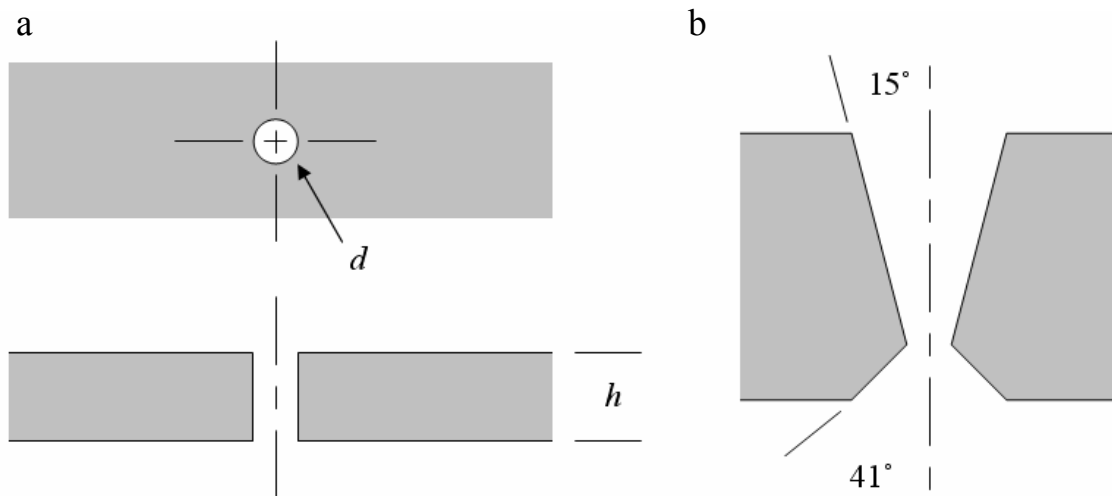


Figure 5.9: Circular simple orifice cross-sectional and top view (a) and converging-diverging cross-sectional view (b).

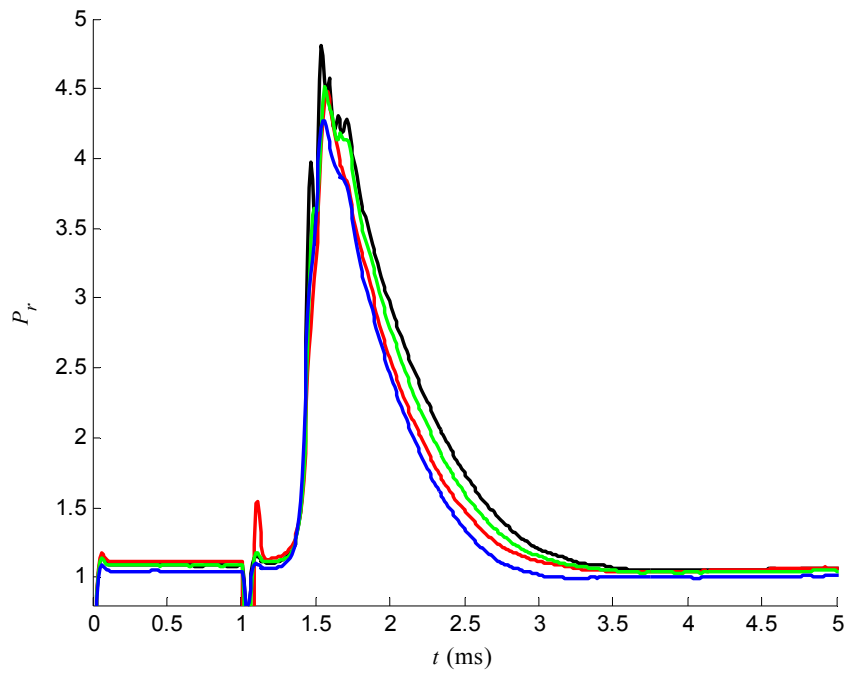


Figure 5.10: Pressure time history varying $h/d = 2.0$ (—), 0.5 (—), 0.7 converging (—), and CD nozzle (—), $V = 2\text{cc}$, $Q = 14\text{ L/min}$, $\Phi = 0.51$, $d = 1.78\text{ mm}$, $f = 30\text{ Hz}$.

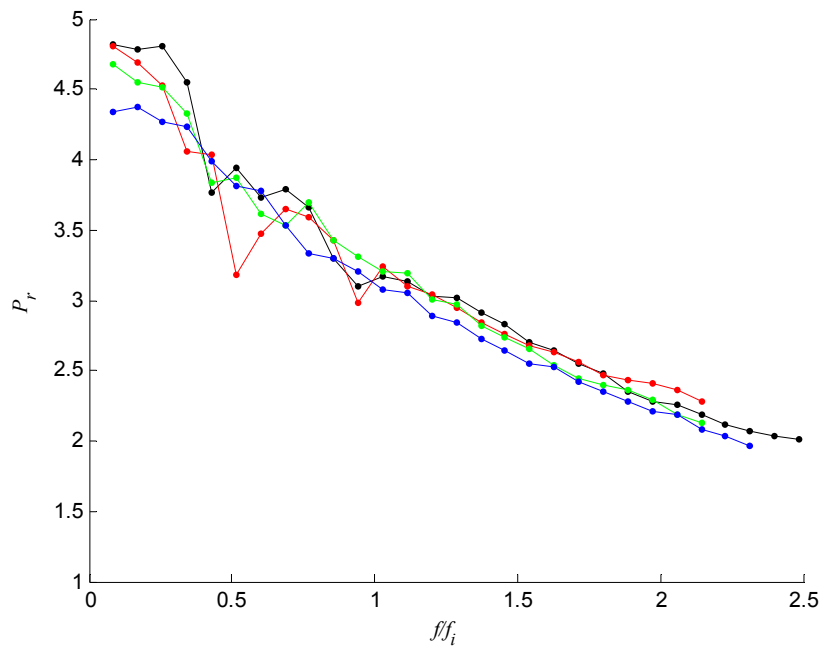


Figure 5.11: Peak pressure vs. normalized actuation frequency varying $h/d = 2.0$ (—), 0.5 (—), 0.7 converging (—), and CD nozzle (—), $V = 2\text{cc}$, $Q = 14\text{ L/min}$, $\Phi = 0.51$, $d = 1.78\text{ mm}$.

configuration as is evident from the pressure time history in Figure 5.10. These data demonstrate that the various orifice shapes considered here have little effect on the performance of the actuator ($h/d = 0.5, 2, 0.7$ converging, and converging-diverging nozzle CD, see Figure 5.9). This observation is also demonstrated in Figure 5.11 which shows variation of the peak pressure with actuation frequency where the highest frequency of $f/f_i = 2.5$ is attained with $h/d = 2$.

5.1.4 Flow Rate

Operation of the combustion actuator at higher frequency requires a higher mixture flow rate in order to refill the combustion chamber more rapidly. Clearly, the higher flow rates have a substantial effect on the mixing process within the combustor and can lead to changes in the combustion properties and flame propagation.

Traces of the pressure time history in Figure 5.12 illustrate the variations with different flow rates at the same (normalized) firing frequency $f/f_i = 0.5$. As expected, the figure shows higher peak pressures and greater rates of pressure rise with higher flow rates. Although t_{peak} decreases with higher flow rates, t_{pulse} is largely unaffected. This can be attributed to the intensified small-scale mixing that increases the flame propagation speed.

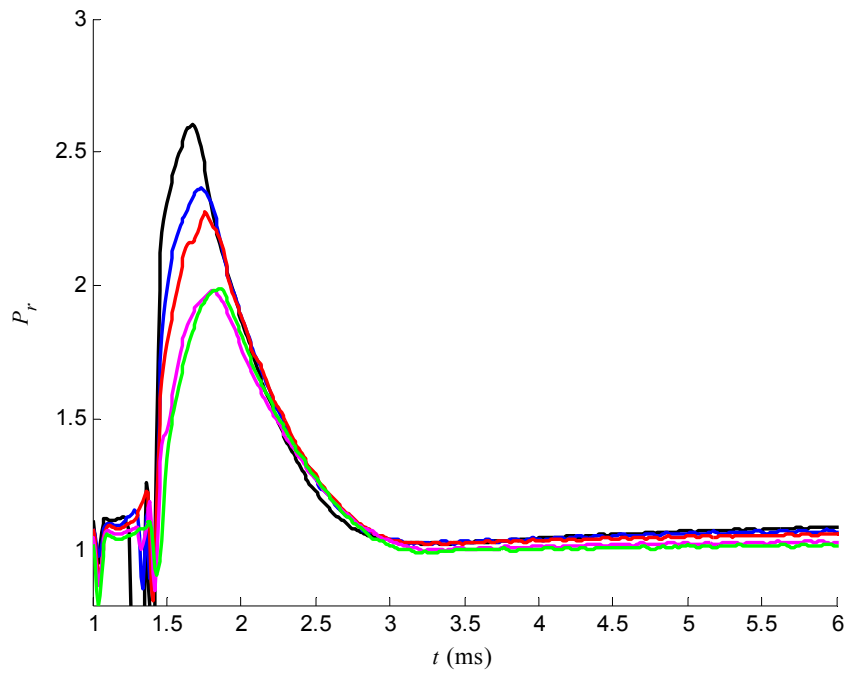


Figure 5.12: Pressure time history varying $Q = 18.0$ (—), 16.0 L/min (—), 14.0 (—), 12.0 (—) and 10.0 (—), $V = 1.33\text{cc}$, $\Phi = 0.27$, $d = 1.98$ mm, $H/D = 1.51$, $f/f_i = 0.5$.

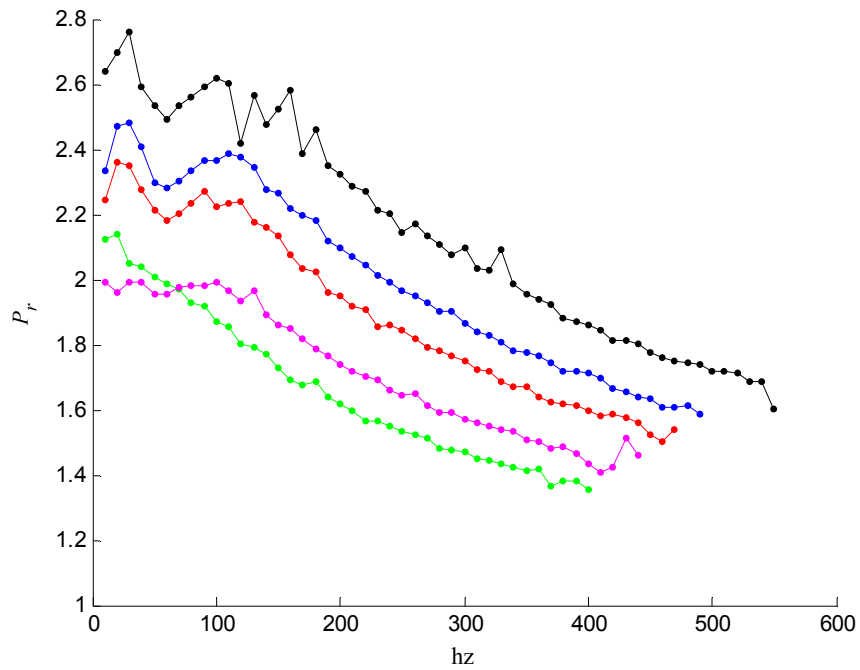


Figure 5.13: Peak pressure vs. actuation frequency, f , varying $Q = 18.0$ (—), 16.0 L/min (—), 14.0 (—), 12.0 (—) and 10.0 (—), $V = 1.33\text{cc}$, $\Phi = 0.27$, $d = 1.98$ mm, $H/D = 1.51$.

Figure 5.13 and Figure 5.14 show the effects of the flow rate on the actuation frequency. In Figure 5.13 the actuation frequency is not normalized and higher flow rates yield higher actuation frequencies as expected. The maximum actuation frequency reached in this test is $f = 550$ Hz with $Q = 18$ L/min, whereas $Q = 10$ L/min yields $f = 400$ Hz. Note that the increase leads to a frequency increase of 150 Hz, where the corresponding change in the ideal actuation frequency is 100 Hz for the $V = 1.33$ cc chamber. However, when these data are plotted versus the normalized actuation frequency in Figure 5.14 this trend is reversed and the highest f/f_i is obtained at the lowest flow rate. Thus, the lower normalized actuation frequency at higher flow rate indicates a loss in overall cycle efficiency.

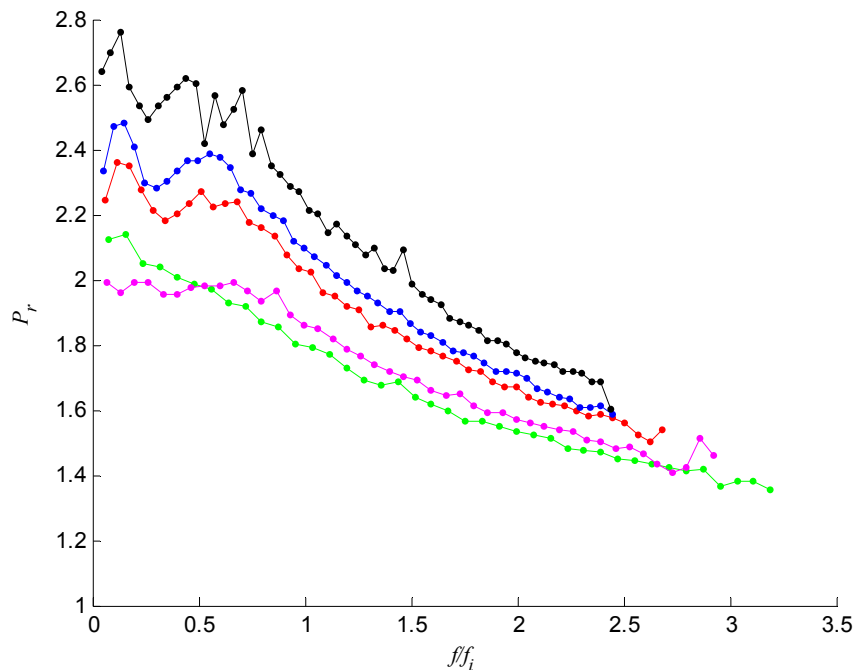


Figure 5.14: Peak pressure vs. normalized frequency, f/f_i , varying $Q = 18.0$ (—), 16.0 L/min (—), 14.0 (—), 12.0 (—) and 10.0 (—), $V = 1.33$ cc, $\Phi = 0.27$, $d = 1.98$ mm, $H/D = 1.51$.

5.1.5 Spark Location and Multiple Ignition Points

Three spark gaps are located in a 2cc combustion chamber that was specifically designed for these experiments. The spark height was varied through $l/H = 0.25$ (upper), $l/H = 0.50$ (middle), and $l/H = 0.75$ (lower). The aspect ratio of the chamber was 2.27, air is injected through a choked orifice at $l_a/H = 0.75$ and $r/R = 0.50$, and fuel is injected axially via the passive fluidic element.

Changing the location of the spark alters the location of the initial flame front and the pattern of the combustion within the chamber. The effects on the pressure time history are shown in Figure 5.15. The initial pressure rise for the lower spark starts as the shortest, potentially because the spark is located closer to the fuel supply, which would have the highest localized equivalence ratio. However, the rate of increase slows (at $t = 1.8\text{ms}$) and results in the lowest peak pressure. It is conjectured that this is the result of heat loss as the flame front propagates along the combustor's side wall towards the exhaust orifice. Additionally, the flame front propagation leads to expulsion of unburned fuel through the orifice.

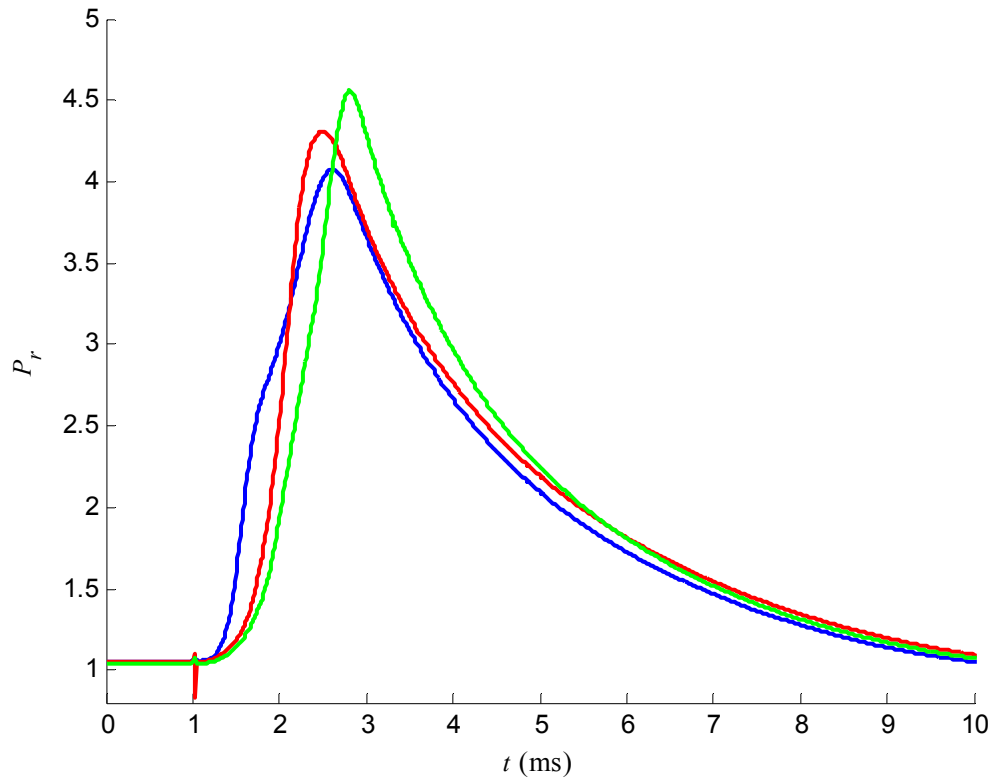


Figure 5.15: Pressure time history comparing spark location $l/H = 0.75$ (—), 0.50 (—), 0.25 (—), $V = 2\text{cc}$, $Q = 2.4\text{ L/min}$, $\Phi = 0.51$, $d = 0.89\text{ mm}$, $H/D = 2.27$, $f = 2\text{ Hz}$.

Under ideal conditions (for uniform mixture) it would be argued that the middle ignition point leads to a flame that advances evenly outward from the center of the cylinder in both axial directions and is quenched at the walls with the minimal heat transfer loss. However, the flame front still pushes some reactants from the combustion chamber prior to burning. While the flame propagation from the upper ignition point, is also limited by contact with the walls, it also propagates against the direction of the nominal flow in the chamber and therefore has a slow t_{peak} . However the flame path allows for the maximum fuel consumption and therefore leads to the highest peak

pressure. Note that all three cases depicted in Figure 5.15 show relatively minor changes in the pulse duration.

The variation of the peak pressures with frequency is shown in Figure 5.16. It is remarkable that the spark location that yields the highest pressure has the t maximum lowest maximum frequency. It is conjectured that the reason is that it takes more time for fresh reactants to reach an ignition point.

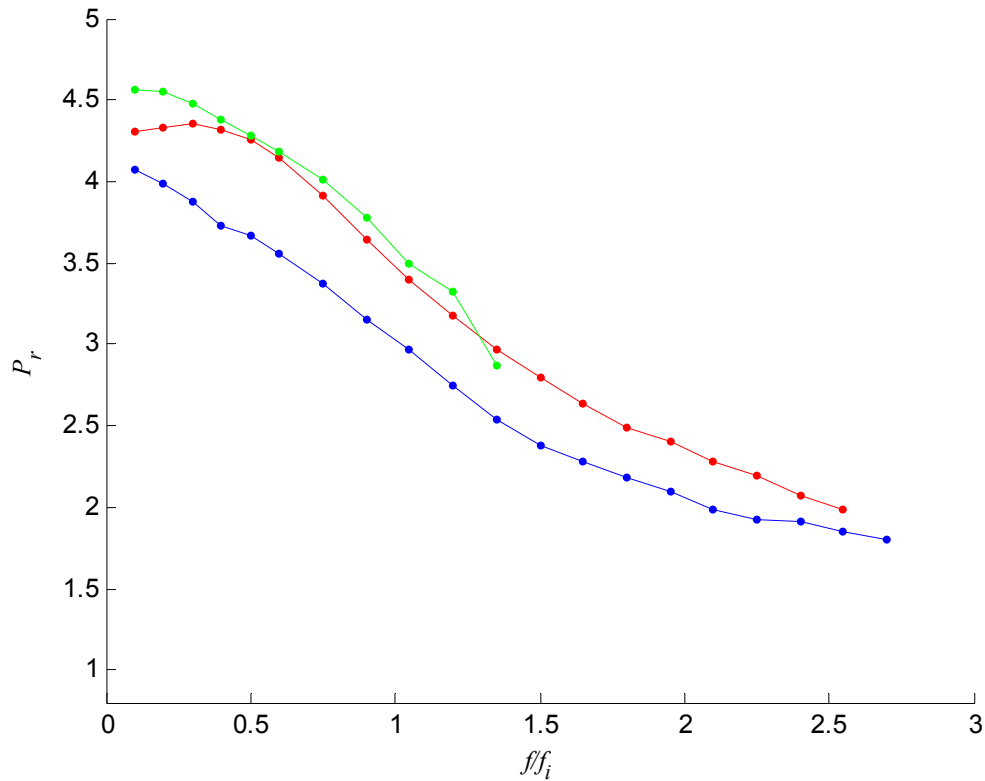


Figure 5.16: Peak pressure vs. normalized actuation frequency comparing spark location $l/H = 0.75$ (—), 0.50 (—), 0.25 (—), $V = 2\text{cc}$, $Q = 2.4\text{ L/min}$, $\Phi = 0.51$, $d = 0.89\text{ mm}$, $H/D = 2.27$.

Multiple ignition points during the combustion cycle result in multiple flame fronts and allow for faster combustion and faster pressure rise. Figure 5.17 shows the pressure time history for three multiple ignition configurations. It is shown that a three-spark ignition configuration ($l/H = 0.25, 0.50, \text{ and } 0.75$) has the highest performance in peak pressure and the shortest t_{peak} and t_{pulse} and therefore it may be argued that multiple sparks can lead to higher operating frequencies. Also shown are two-spark configurations at $l/H = 0.25, 0.50$ and $l/H = 0.50, 0.75$. Figure 5.18 shows that the three-spark configuration leads to a somewhat higher operating frequency, but not significantly higher than for the two-spark configuration.

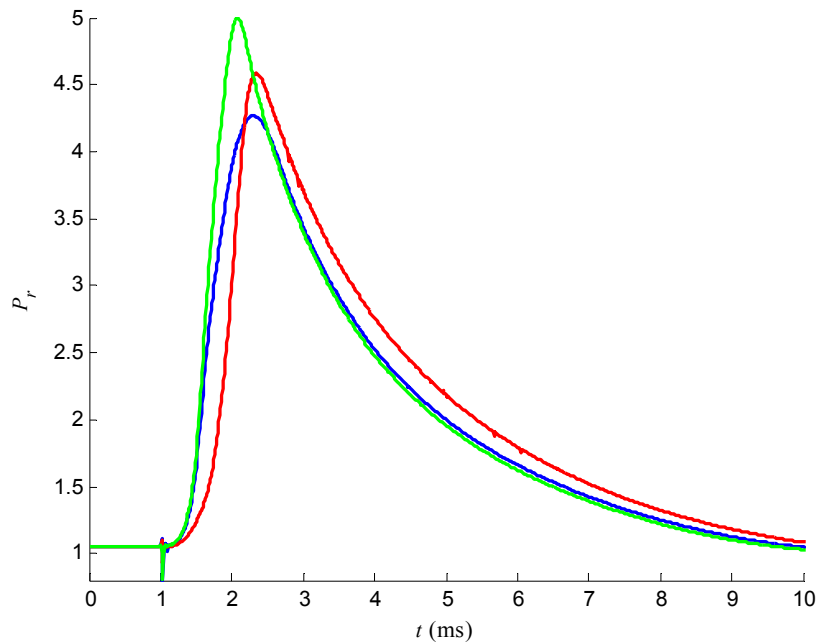


Figure 5.17: Pressure time history comparing multiple sparks and their location $l/H = 0.75 \text{ \& } 0.50$ (—), $0.50 \text{ \& } 0.25$ (—), $0.75 \text{ \& } 0.50 \text{ \& } 0.25$ (—), $V = 2\text{cc}$, $Q = 2.4 \text{ L/min}$, $\Phi = 0.51$, $d = 0.89 \text{ mm}$, $H/D = 2.27$, $f = 2 \text{ Hz}$.

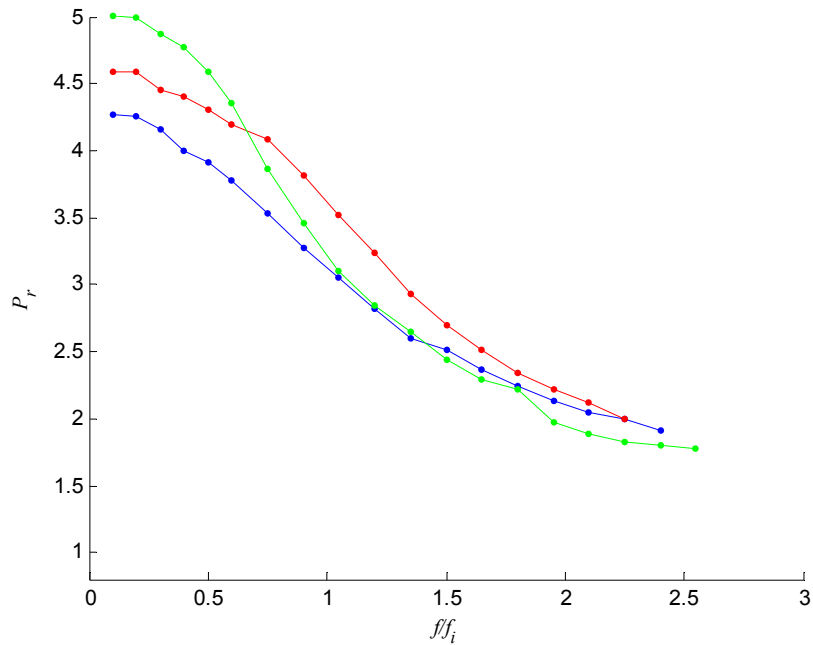


Figure 5.18: Peak pressure comparing multiple sparks and their location $l/H = 0.75$ & 0.50 (—), 0.50 & 0.25 (—), 0.75 & 0.50 & 0.25 (—), $V = 2\text{cc}$, $Q = 2.4\text{ L/min}$, $\Phi = 0.51$, $d = 0.89\text{ mm}$, $H/D = 2.27$, $f = 2\text{ Hz}$.

5.2 Chamber Size and Shape

5.2.1 Chamber Volume

Figure 5.19 and Figure 5.20 show the effect of the chamber volume on the actuation frequency (dimensional and normalized respectively). Figure 5.19 shows that the two most notable characteristics of increasing the volume are the increase in peak pressure, and a decrease in the maximum attainable frequency, f_{\max} . For $V = 0.25\text{cc}$ f_{\max} is highest and the rate of pressure decrease lowest. Higher volumes show a larger change in pressure within their operating ranges. This is somewhat misleading since Q is

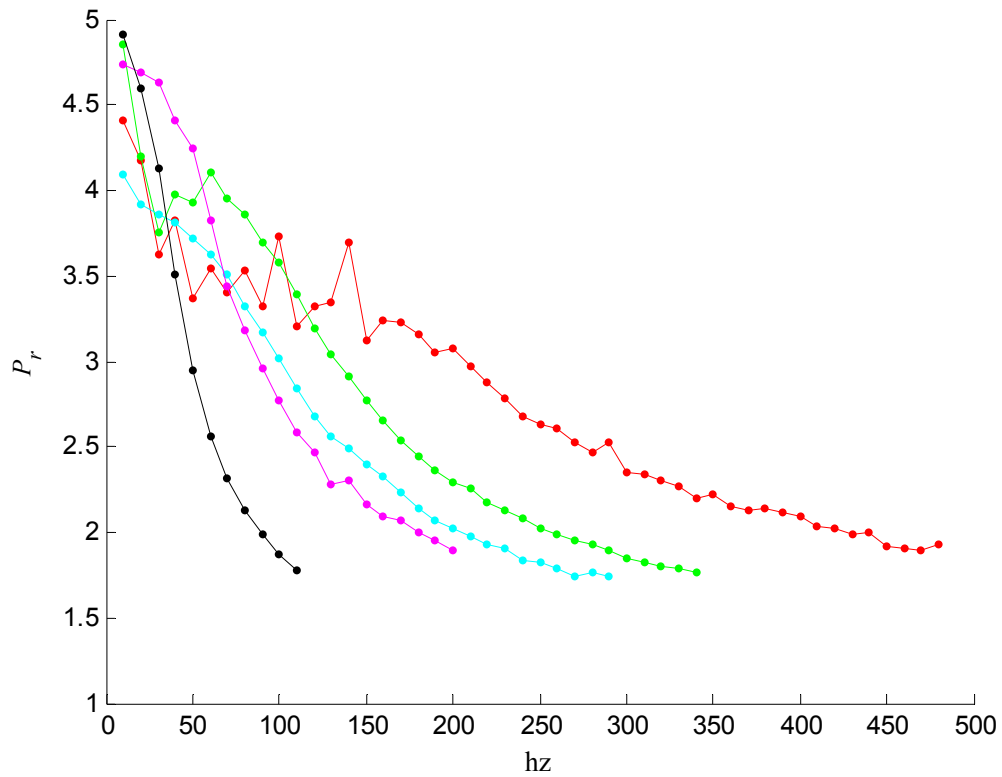


Figure 5.19: Nonpremixed peak pressure vs. actuation frequency with $V = 0.25$ (—), 0.50 (—), 0.75 (—), 1.00 (—), $2cc$ (—), $Q = 4$ L/min, $d = 0.89$ mm, and $\Phi = 0.51$.

unchanged and therefore the ideal actuation frequency decreases. When these data are plotted at the normalized frequency (Figure 5.20), rate of change of pressure is similar for different volumes. Also, the maximum normalized actuation frequency is attained with $V = 2cc$ (not $V = 0.25cc$) which also has a better thermal efficiency (as measured by the ratio of A_s/V for heat transfer loss and total potential chemical energy as discussed in chapter 4).

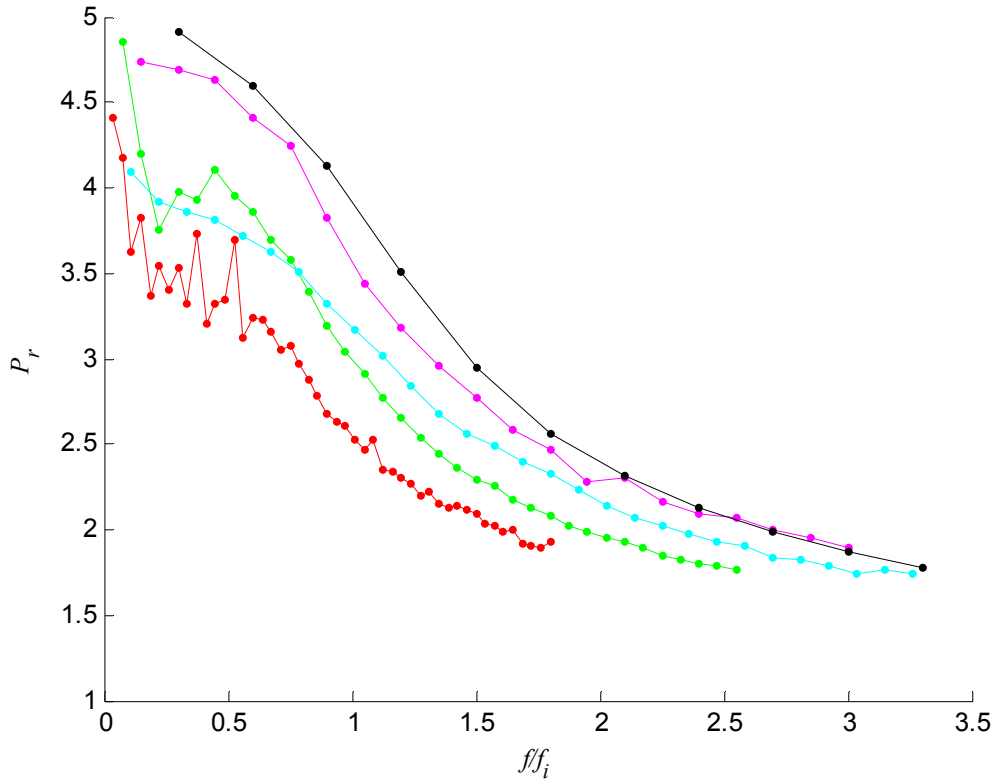


Figure 5.20: Nonpremixed peak pressure vs. normalized actuation frequency with varying $V = 0.25$ (—), 0.50 (—), 0.75 (—), 1.00 (—), $2cc$ (—), $Q = 4$ L/min, $d = 0.89$ mm, and $\Phi = 0.51$.

5.2.2 Aspect Ratio

The aspect ratio AR of the combustion chamber is defined as the ratio of the chamber height to its diameter, H/D . Changing the aspect ratio alters the surface area of the combustion chamber walls and alters the shape of the propagating flame, which directly affects the chemical energy release rate and the amount of heat transfer loss. As noted early, the chamber design with the absolute minimum surface area is spherical (see Table 4.2). The minimum surface area achievable for a cylindrical chamber has an $H/D =$

1, which also enables the flame to propagate evenly to all internal surfaces at about the same time. With $AR > 1$ or < 1 , the flame can reach some surface earlier than others leading to an increased heat loss. With $H/D \gg 1$, the combustion chamber is a tube where the flame propagates along its axis. While $H/D \ll 1$, the chamber is shaped like a disk and the flame propagates radially. Assuming that the flame front is at a distance of $S_L \cdot t$ from the spark, the time rate of change for the combusted volumes can be estimated as:

$$\text{Spherical flame front } (H/D \approx 1) \quad \frac{\partial V}{\partial t} = \frac{4}{3} \pi (S_L)^3 t^2 \quad \text{Eq. 5.6}$$

$$\text{Radial flame front } (H/D \ll 1) \quad \frac{\partial V}{\partial t} = \pi H (S_L)^2 t \quad \text{Eq. 5.7}$$

$$\text{Dual linear flame fronts } (H/D \gg 1) \quad \frac{\partial V}{\partial t} = \frac{\pi}{2} D^2 S_L \quad \text{Eq. 5.8}$$

These equations give a simplified approximation to the flame propagation based on idealized operating conditions and laminar flame speed. Fastest burn times are present with chamber aspect ratios close to unity, then chambers with $H/D < 1$, and slowest burn times with chambers having $H/D > 1$ (Crittenden 2003).

Figure 5.21 shows the pressure time histories of the two different aspect ratio chamber used in these investigations ($H/D = 1.27$ and $H/D = 2.27$) with the flow conditions $V = 2\text{cc}$, $Q = 4.8 \text{ L/min}$, $d = 1.50 \text{ mm}$, $\Phi = 0.51$, and at $f = 10 \text{ Hz}$. The lower aspect ratio chamber has significantly more peak pressure at $P_r = 4.8$ for $H/D = 1.27$ and

$P_r = 3.5$ for $H/D = 2.27$. Pulse duration remains unchanged at nearly 4 ms, however t_{peak} is lower with the lower aspect ratio with $t_{\text{peak}} = 0.8$ ms for $H/D = 1.27$ and $t_{\text{peak}} = 1.25$ ms for $H/D = 2.27$. Figure 5.22 plots the peak pressures to normalized actuation frequencies showing the $H/D = 1.27$ chamber obtained higher actuation frequencies ($f/f_i = 1.7$ for $H/D = 1.27$ compared to $f/f_i = 0.8$ for $H/D = 2.27$).

Most of the combustion chambers tested in the present work have an aspect ratio $H/D = 1.27$ which is similar to chambers used in the works of Crittenden (2003) and Crittenden, Warta et al. (2006).

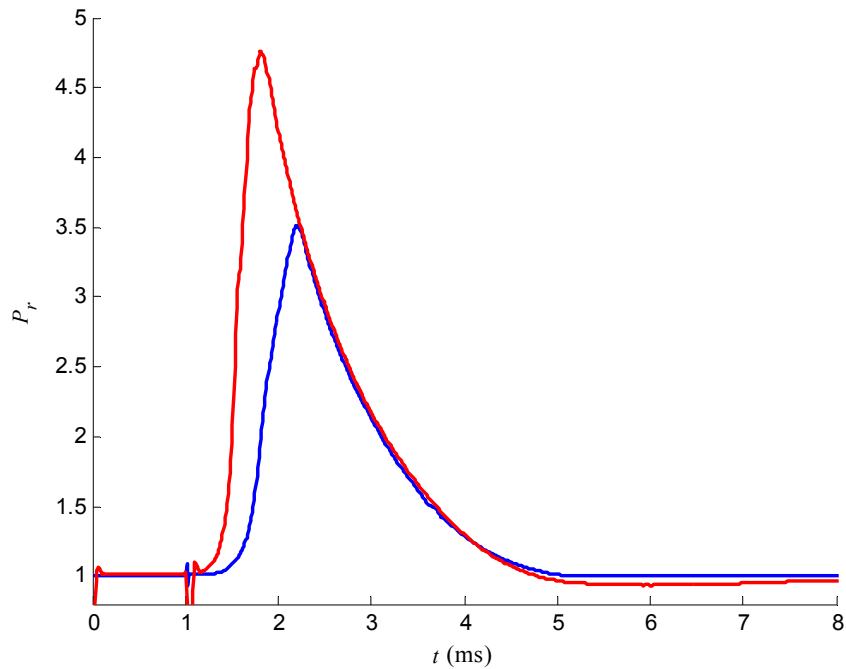


Figure 5.21: Pressure time history with $H/D = 1.27$ (—) and $H/D = 2.27$ (—) for $V = 2\text{cc}$, $Q = 4.8\text{ L/min}$, $d = 1.50\text{ mm}$, $\Phi = 0.51$, $f = 10\text{ Hz}$.

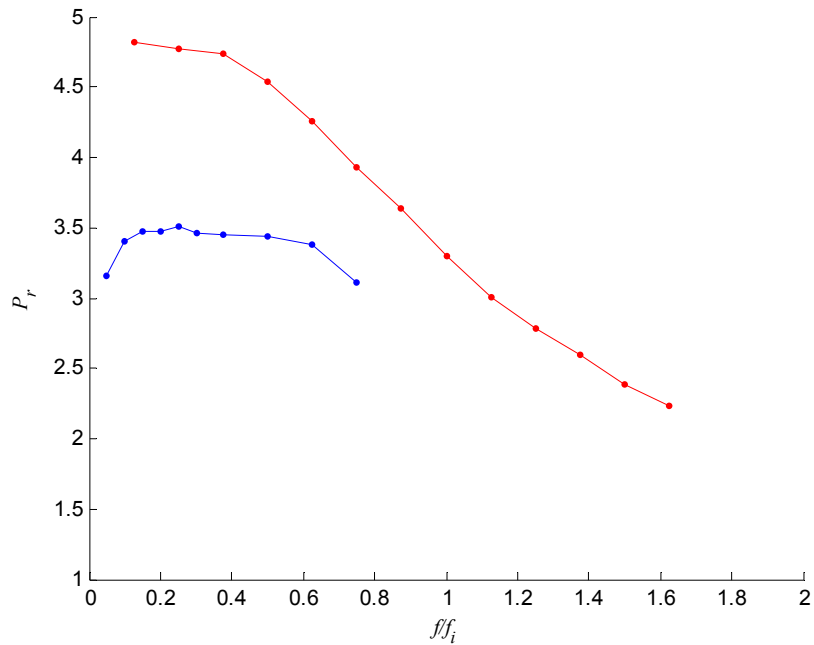


Figure 5.22: Peak pressure ratio vs. normalized frequency with $H/D = 1.27$ (—) and $H/D = 2.27$ (—) for $V = 2\text{cc}$, $Q = 4.8\text{ L/min}$, $d = 1.50\text{ mm}$, $\Phi = 0.51$.

5.3 Fuel/Air Injection

5.3.1 Air Inlet

This section details the variations of combustor performance when the location of the air inlet is varied with respect to the chamber height, H . The air is injected normal to the fuel flow at $r/R = 0.50$ to induce swirl. Three positions were explored: closest to the fuel intake ($l_a/H = 0.75$), centered ($l_a/H = 0.50$), and furthest from the fuel intake ($l_a/H = 0.25$). The placement of the air inlet clearly modifies the characteristics of the flow field within the chamber, which affects its performance in both peak pressure and operating

frequency range. Figure 5.23 illustrates that the inlet at $l_a/H = 0.75$ and 0.50 results in the highest peak pressures, and longest t_{pulse} and t_{peak} . The inlet at $l_a/H = 0.25$ results in the lowest peak pressure, and has a significant decrease in t_{pulse} and t_{peak} . Figure 5.24 shows the range of operating frequencies. The highest frequency attained is for $l_a/H = 0.75$, followed by $l_a/H = 0.25$, then $l_a/H = 0.50$. Significant reduction in the actuation frequency for $l_a/H = 0.50$ may be the proximity of the injection to the spark which may have precipitated a steady flame at the low frequency. It is also speculated that air injection at $l_a/H = 0.25$ prevents thorough mixing within the chamber because of the distance from the fuel source. The operational limit of the other two injection location is associated with autoignition.

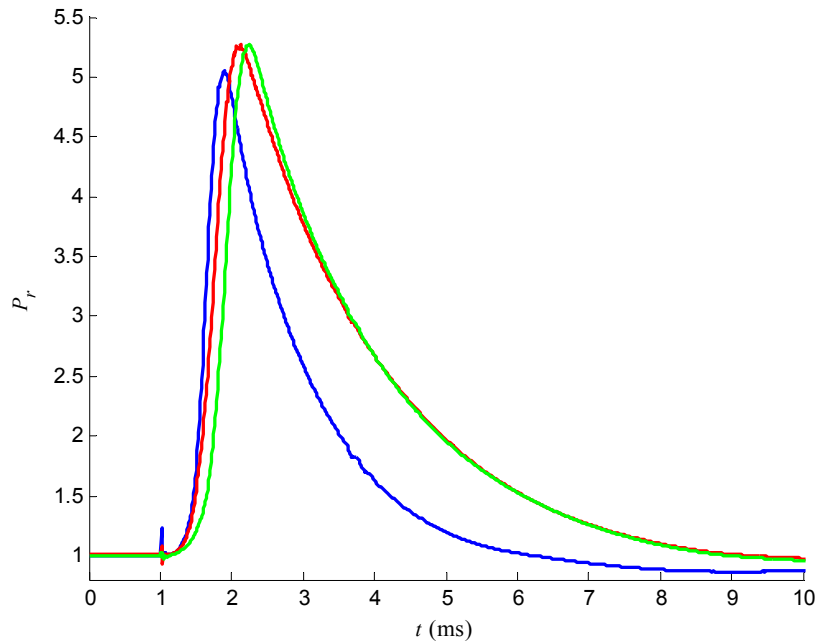


Figure 5.23: Pressure time history with air intake $l_a/H = 0.25$ (—), $l_a/H = 0.50$ (—), $l_a/H = 0.75$ (—), $V = 2\text{cc}$, $Q = 4.8\text{ L/min}$, $d = 0.89\text{ mm}$, $\Phi = 0.51$, $H/D = 2.27$, $f = 2\text{ Hz}$, $r/R = 0.50$.

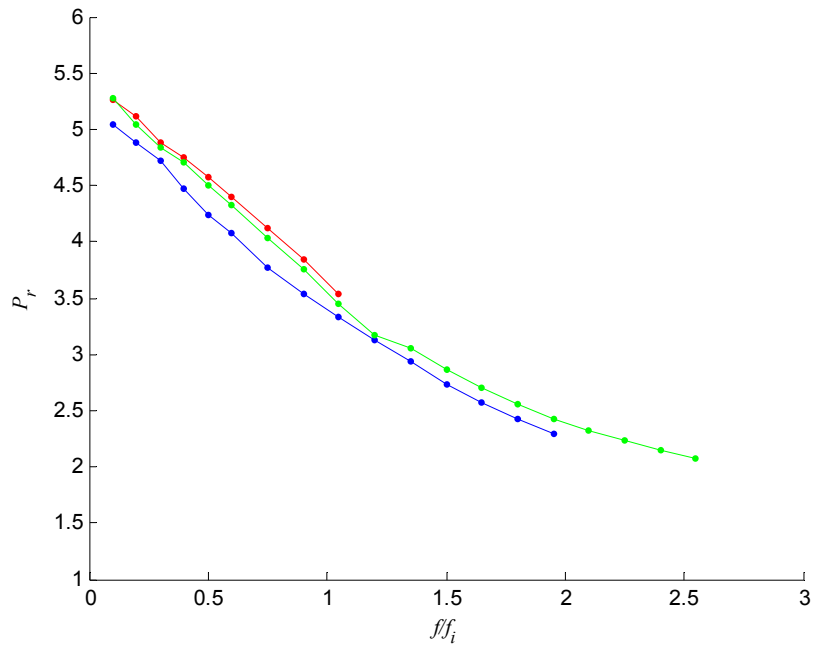


Figure 5.24: Peak pressure vs. actuation frequency of three air intake $l_a/H = 0.25$ (—), $l_a/H = 0.50$ (—), $l_a/H = 0.75$ (—), $V = 2\text{cc}$, $Q = 4.8\text{ L/min}$, $d = 0.89\text{ mm}$, $\Phi = 0.51$, $H/D = 2.27$, $f = 2\text{ Hz}$, $r/R = 0.50$.

5.3.2 Fluidic Element

The fluidic element used in most of the actuators is made from porous sintered metal cut into a flat disk shape. When placed at the base of the combustion chamber, it acts as one of the chamber's walls and quenches the oncoming flame, but has the ability to seep gaseous fuel into the chamber. This element is implemented as the passive fluidic "valve" by utilizing the pressure drop across it. For nonpremixed operation, the fuel supply line requires a relatively low line pressure in comparison to the premixed case. This lower line pressure allows the fluidic actuator to continue to operate at higher actuation frequencies while chamber pressure decreases.

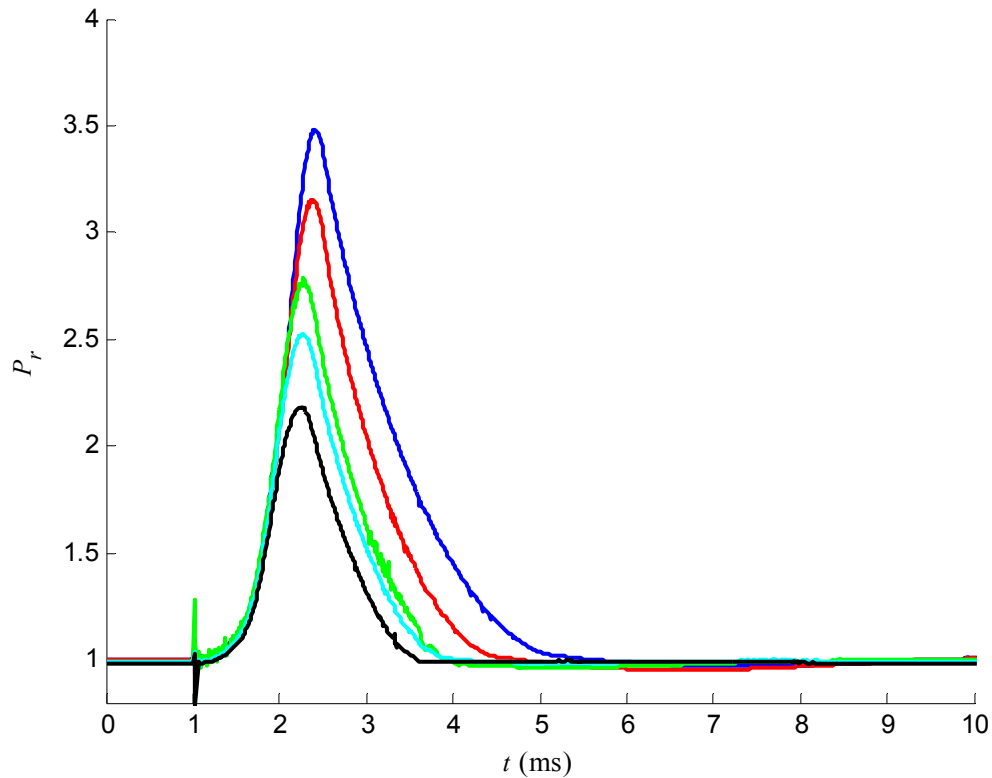


Figure 5.25: Pressure time history with varying sintered metal porosity level of 2 (—), 5 (—), 10 (—), 20 (—), 40 μm (—), $V = 2\text{cc}$, $Q = 2.4\text{ L/min}$, $d = 1.50\text{ mm}$, $\Phi = 0.51$, $H/D = 2.27$, and $f = 2\text{ Hz}$.

As shown in Figure 5.25, increasing the porosity of the sintered metal affects the chamber in much the same way as increasing the exhaust orifice diameter. Highly porous element results in a decrease in the peak pressure, as more backflow occurs through the sintered metal. The time to peak pressure and t_{pulse} is noticeable shorter. Although there is a reduction in peak pressure and impulse with increased porosity, Figure 5.26 shows that a substantial increase in actuation frequency can be obtained at higher porosity (e.g. 20 μm), but there is also a reduction in the maximum chamber pressure.

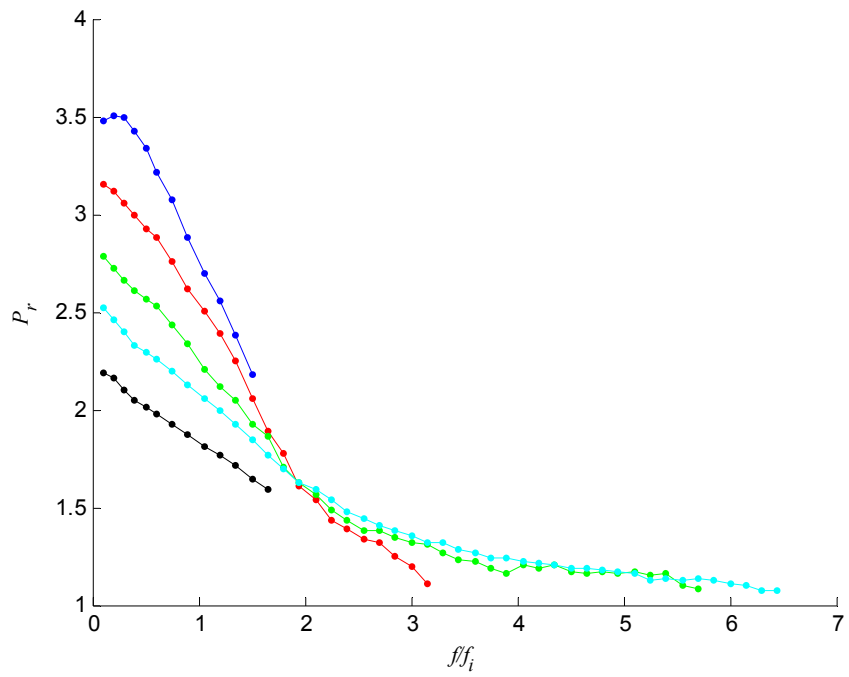


Figure 5.26: Peak pressure with varying sintered metal porosity level of 2 (---), 5 (---), 10 (---), 20 (---), 40 μm (---), $V = 2\text{cc}$, $Q = 2.4\text{ L/min}$, $d = 1.50\text{ mm}$, $\Phi = 0.51$, $H/D = 2.27$.

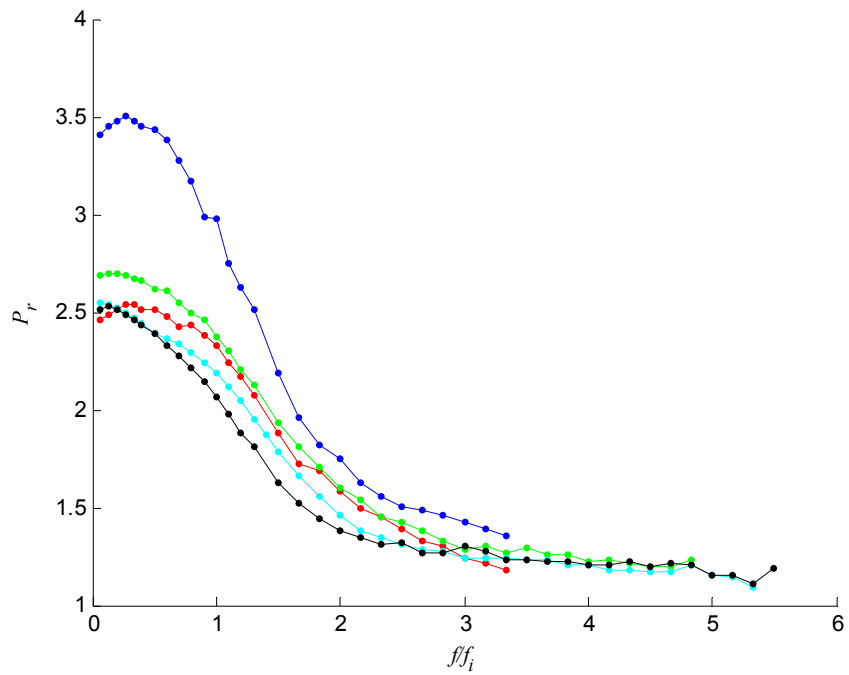


Figure 5.27: Peak pressure with varying sintered metal porosity level of 2 (---), 5 (---), 10 (---), 20 (---), 40 μm (---), $V = 2\text{cc}$, $Q = 3.6\text{ L/min}$, $d = 1.50\text{ mm}$, $\Phi = 0.51$, $H/D = 2.27$.

Higher porosity is needed for higher flow, as shown in Figure 5.27 for the same combustion chamber as in Figure 5.26. The maximum frequency (not the highest pressure) is achieved at 40 μ m.

5.3.3 Reed Valves

An alternative to the sintered metal element is a passive valve based on a moving reed that allows flow in one direction only, shutting off when downstream pressure exceeds upstream pressure. The advantage of using reed valves in COMPACT versus sintered metal is the potential for higher chamber pressures due to lower back flow of combustion products. The drawback however is the addition of a moving part to the system, possibly hindering its long term reliability.

The reed valves tested in the present work were constructed out of various shim stock materials and were fabricated by laser cutting. Figure 5.28 shows an example of a reed valve design including a brass orifice grid plate (Figure 5.28a) which rests on the sintered metal facing the combustion chamber. The reed valves are placed between the combustion chamber and the orifice grid and are aligned with the orifice plate (Figure 5.28b). When the pressure in the fuel line is greater than the chamber pressure, the reed valve opens (Figure 5.28c) to allow flow. As the chamber pressure exceeds the line pressure during combustion, the valve close on the orifice grid to seal off the flow of fuel.

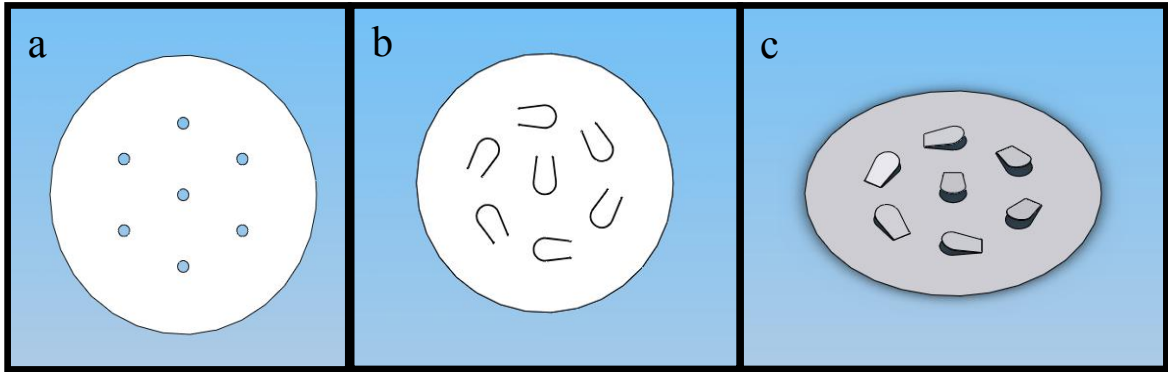


Figure 5.28: Reed valve design utilizing two plates, inlet orifice grid plate (a), and reed valve plate (b and c).

Figure 5.29 shows a comparison between a conventional sintered metal element and reed valves. Several reed valve plates manufactured from 12.7 microns thick 301 stainless steel. The reeds are 0.75 mm wide and at varying lengths. Actuators with reed valves could achieve higher pressures, as expected. A 2 mm reed provides the highest pressure overall. The rate of pressure rise remains unchanged among each configuration while the t_{peak} increases slightly with the reed valve setup. Pulse duration is noticeably longer with the actuators using reed valves.

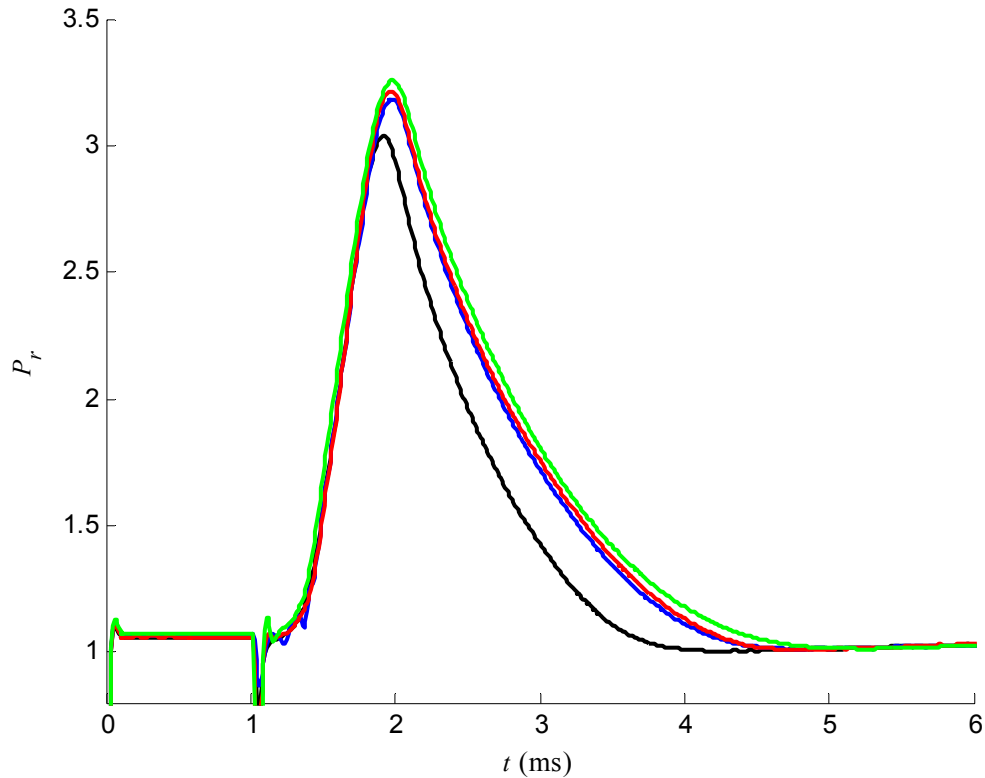


Figure 5.29: Pressure time history comparing conventional reedless design (—) with reed valve lengths of 1.40 (—), 1.75 (—), 2 mm (—), 11 reed configuration, 12.7 μ m thick reeds, $V = 2\text{cc}$, $Q = 14\text{ L/min}$, $d = 1.78\text{ mm}$, $\Phi = 0.37$, $f = 10\text{ Hz}$, $H/D = 1.27$.

As expected, the maximum actuation frequency decreases when the reed valves are used as shown in Figure 5.30. The chamber configuration without reed valves has the highest actuation frequency. However, the use of the reed valves lead to higher chamber pressures. The temporal performance of the reed valves can be considerably improved by altering the material from which they are fabricated and thereby increasing the natural frequency. The design process also considered resonance modes that could lead to destruction of the reeds.

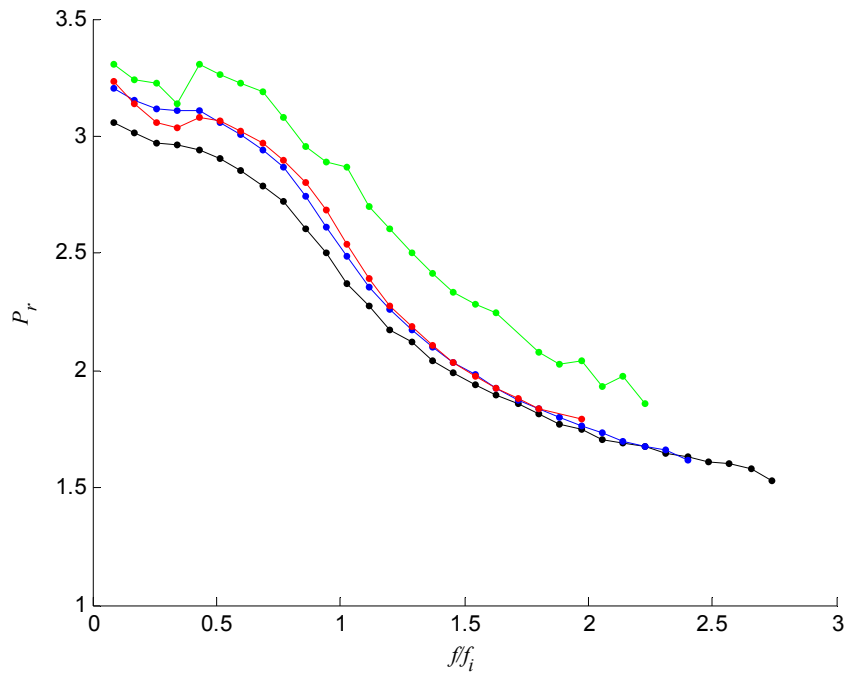


Figure 5.30: Peak pressure vs. normalized frequency comparing conventional reedless design (—) with reed valve lengths of 1.40 (—), 1.75 (—), 2 mm (—), 11 reed configuration, 12.70 μm thick reeds, $V = 2\text{cc}$, $Q = 14\text{ L/min}$, $d = 1.78\text{ mm}$, $\Phi = 0.37$, $H/D = 1.27$.

Figure 5.31 shows the pressure time history comparing the different types of reed valve material to a configuration in the absence of reed valves. All reed valves are 2 mm long, 0.75 mm wide, and 50.80 μm thick (except the graphite foil which is of 280 μm thick). It is remarkable that all pressure curves are fairly similar. The chamber without reed valves had the longest time to peak pressure and the median pulse duration. The stainless steel reed valves had the highest peak pressure and the shortest pulse duration. For maximum actuation frequency under the same test conditions as Figure 5.31, the titanium reed valves attained the highest $f/f_i = 2.15$, then spring steel at $f/f_i = 2.10$, stainless steel at $f/f_i = 2$, and graphite foil and fluidic element at $f/f_i = 1.6$.

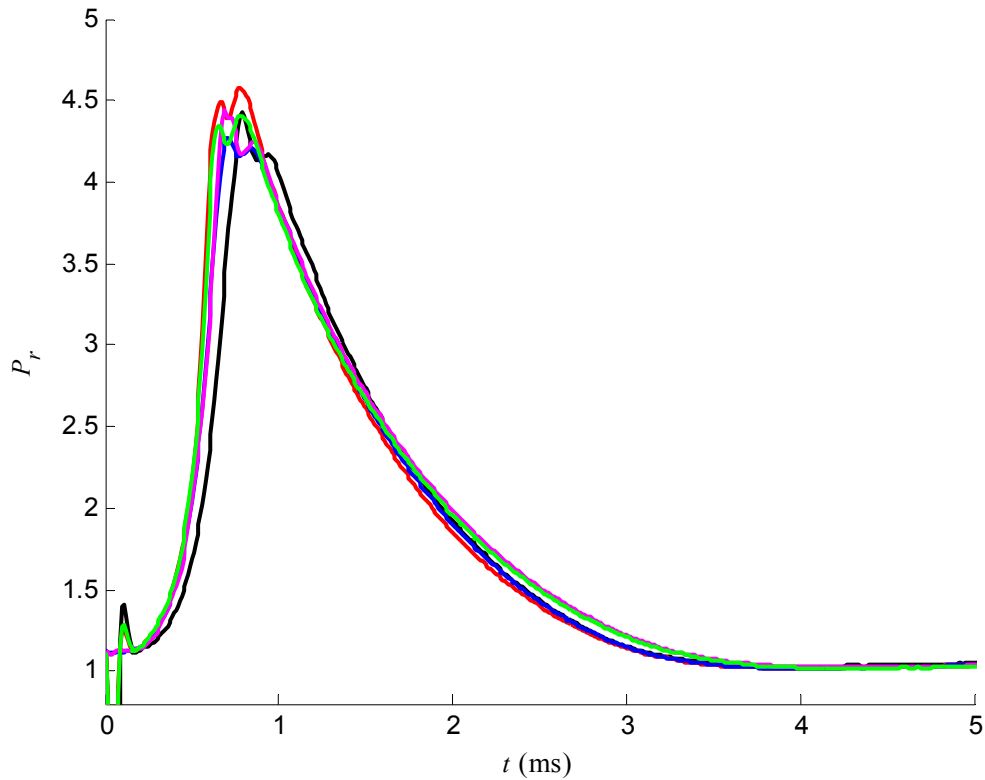


Figure 5.31: Pressure time history comparing conventional reedless design (—) to reeds made of 301SS (—), Spring Steel (—), Ti (—), Graphite foil (—), reed length 2 mm and thickness 50.80 μm , $V = 2\text{cc}$, $Q = 14\text{ L/min}$, $d = 1.61\text{ mm}$, $\Phi = 0.37$, $H/D = 1.27$, and $f/f_i = 0.17$.

5.3.4 Direct Injection of Fuel and Air

A combustion chamber that operates based on fuel starvation rather than fast fluidic element could allow for actuation frequencies that are more closely linked to flame speed rather than pressure differentials across the fluidic element. The principle is to design a fuel and air injection system that requires a certain amount of time before the two gases coalesce and mix within the chamber, therefore allowing time for the

combustion process to be complete before a combustible mixture is available. Thus the process of converting the fuel injection system to direct injection (DI), similar to the air injection system, is tested.

Manipulating the inflow of fuel and air within the chamber significantly affects the mixing process within the combustion chamber, which in turn affects the flame propagation and the performance of the actuator. Four different injection configurations are investigated to assess their effect on performance. Figure 5.32 illustrates the configuration tested, including the standard injection technique with sintered metal (Figure 5.32a), direct injection with induced co-rotational swirl (Figure 5.32b), direct injection with impinging flows and induced swirl (due to the greater mass flux of air that controls the mean flow, Figure 5.32c), and direct injection with impinging flow without swirl (Figure 5.32d). The chamber volume is $V = 2\text{cc}$, l_a/L and $l_f/L = 0.875$ for the direct injection setup with $r/R = 0.875$ for configurations with swirl. The air inlet diameter, d_a , is at 0.79 mm and the fuel inlet diameter, d_f , 0.40 mm.

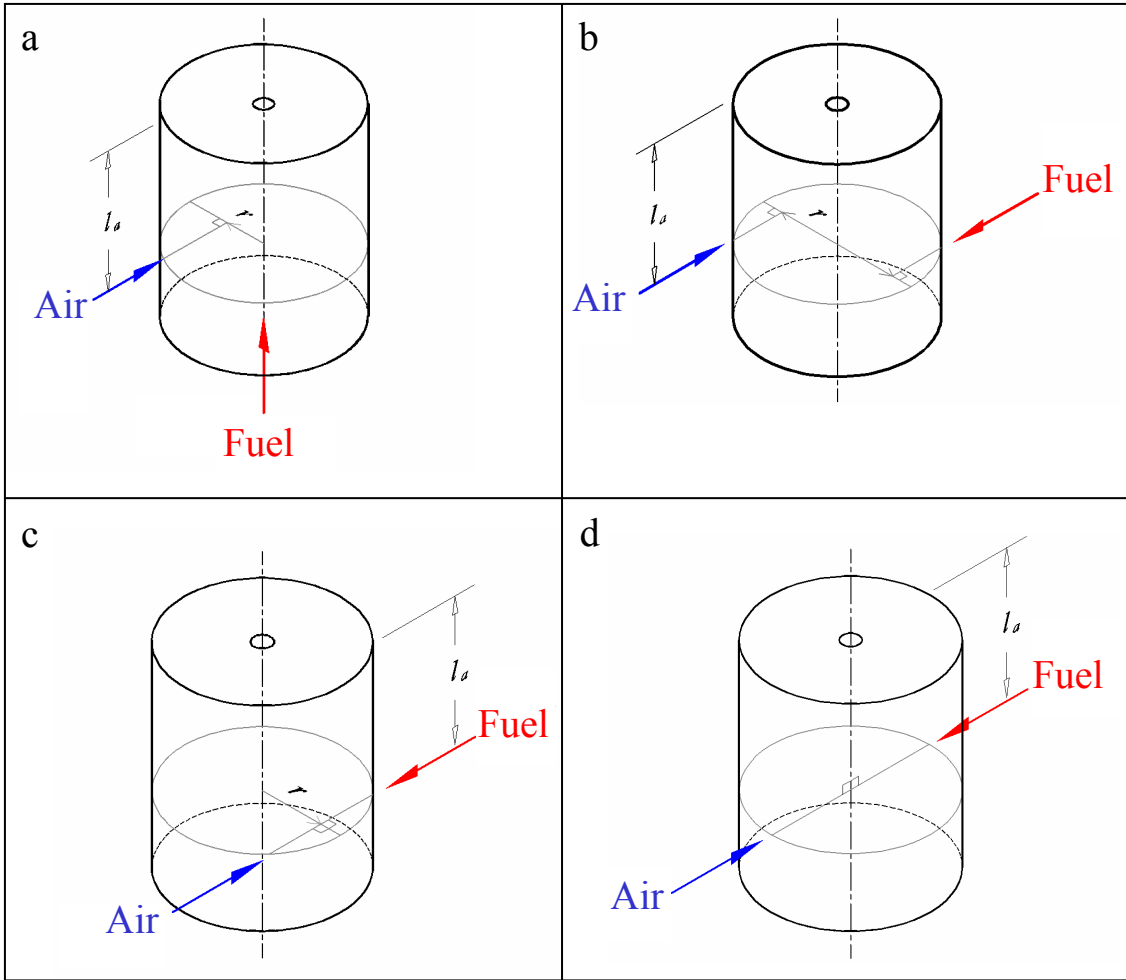


Figure 5.32: Different injection configurations: standard injection with sintered metal (a), direct injection with induced co-rotational swirl (b), direct injection with impinging flow and swirl (c), and direct injection with impinging flow (d).

The performance variations between the different inlet configurations are shown in Figure 5.33 and Figure 5.34. The pressure time history in Figure 5.33 shows a pressure curve for each type of injection technique. The sintered metal configuration yields the lowest peak pressure ($P_r = 3.18$), and the shortest t_{pulse} (1.09 ms) and t_{peak} (0.73 ms). The direct injection with co-rotational swirl has the highest peak pressure ($P_r = 3.5$), but the second longest t_{pulse} (1.73 ms) and third longest t_{peak} (0.89 ms). Direct injection with

impinging flow with swirl has the second highest peak pressure ($P_r = 3.38$), the longest t_{pulse} (1.82 ms) and t_{peak} (0.96 ms). Finally, the direct injection with impinging flows without swirl has the second lowest peak pressure ($P_r = 3.3$) and the second shortest t_{pulse} (1.49 ms) and t_{peak} (0.78 ms).

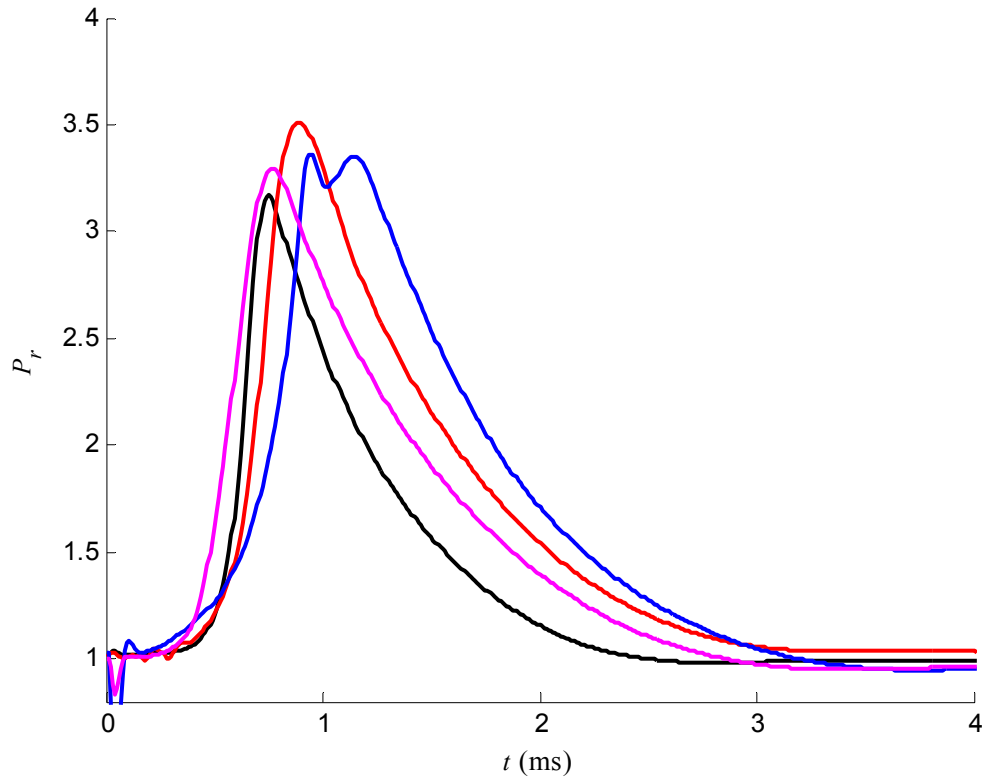


Figure 5.33: Pressure time history comparing the use of sintered metal (—) with direct injection of co-rotational swirl (—), impinging swirl (—), and impinging without swirl (—), $V = 2\text{cc}$, $Q = 14\text{ L/min}$, $d = 1.98\text{ mm}$, $\Phi = 0.37$, $H/D = 1.27$ (100 micron sintered metal used).

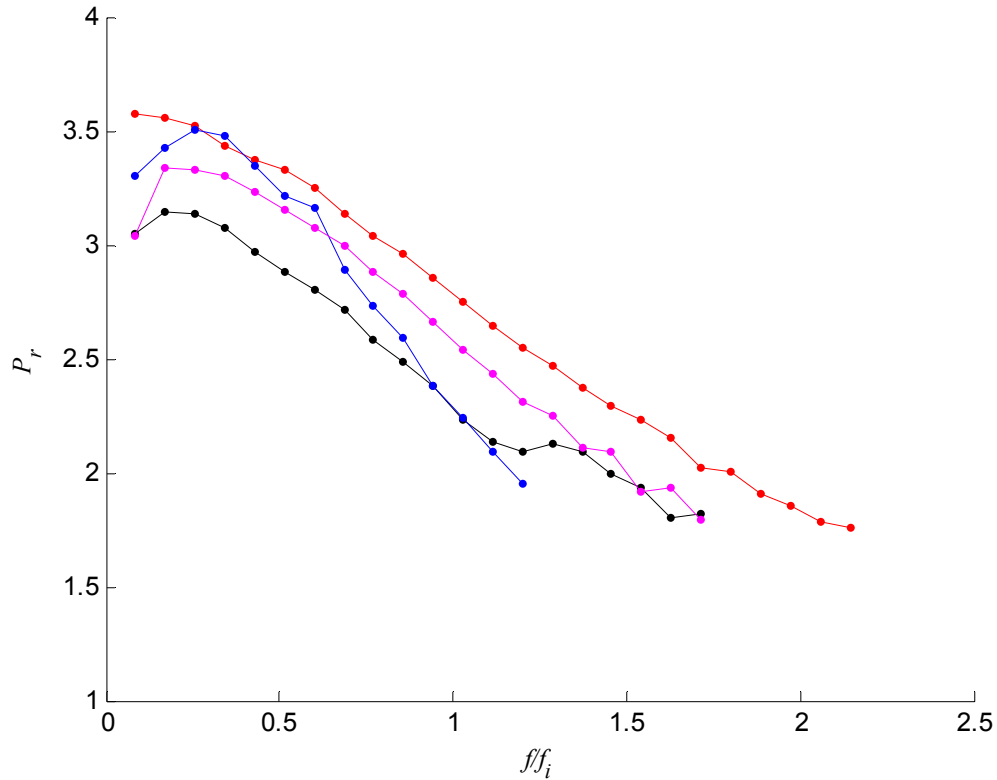


Figure 5.34: Peak pressure comparing the use of sintered metal (—) with direct injection co-rotational swirl (—), impinging swirl (—), and impinging without swirl (—), $V = 2\text{cc}$, $Q = 14\text{ L/min}$, $d = 1.98\text{ mm}$, $\Phi = 0.37$, $H/D = 1.27$ (100 micron sintered metal used).

Figure 5.34 shows the variation of peak pressure with normalized actuation frequency of the various inlet configurations. The sintered metal configuration has the lowest overall pressure readings on average and the second highest actuation frequency ($ff_i = 1.7$). Direct injection with co-rational swirl has the highest peak pressure and the highest actuation frequency ($ff_i = 2.14$). This is likely due to the spacing between injectors being the furthest apart in this configuration, allowing more time before mixing and more mixture to be present. Direct injection with impinging flows with swirl had the second highest peak pressure from $0 < ff_i \leq 0.6$, but drops $ff_i > 0.6$ at the end of its range

and stopping short with the lowest actuation frequency ($f/f_i = 1.2$). This configuration has the closest placement of the fuel and air injectors to each other, limiting both time and mixture quantity. Lastly the direct injection with impinging flows without swirl had the second highest actuation frequency on average and tied with the second highest actuation frequency ($f/f_i = 1.7$). This placement of injectors is the second closest of the configurations, which justifies its performance.

CHAPTER 6

CONCLUSION

The combustion powered actuator (COMPACT) is a novel and high momentum flux fluidic actuator that can provide brief high-impulse actuation for flow control. A robust reliable design is possible due to the absence of moving parts, and the actuator can also be easily integrated in many flow systems because of its flexible geometry which allows it to conform to a wide range of confined spaces and aerodynamic surfaces.

The performance of COMPACT depends primarily on the maximum actuation frequency and peak pressure. As shown in earlier work the combustion chamber peak pressure decreases as the actuator frequency increases. This is expected since an increase in operating frequency reduces the amount of time in which fresh reactants can enter the combustion chamber for the following combustion cycle. As actuation frequency increases, more residual combustion products dilute the fuel/oxidizer mixture and therefore the energy release per cycle decreases (although the impulse over a given period of time can increase).

In earlier investigations of COMPACT the actuator design was based on premixed configuration in which the fuel and oxidizer were mixed upstream of the combustor. This configuration results in performance limitations that can be alleviated by

using a nonpremixed configuration in which the fuel and oxidizer are mixed within the combustion chamber and the focus of the present investigation. It is shown that nonpremixed configuration can improve both the maximum operating frequency and the peak pressure by taking advantage of the internal small-scale mixing within the combustion chamber. Small-scale mixing results in higher flame speed and can be manipulated to allow for preferential internal flow path of the combustion products. This along with higher flame speed leads to an increased chamber pressure and shorter actuation cycle that raises the actuation frequency.

The present work has considered the effects of several actuator parameters on the overall performance:

Exhaust Orifice (area and shape). The size directly affects the thrust and impulse of the exhaust jet and changes in the orifice area result in significant changes in chamber pressure and pulse duration. In addition to its effect on the thrust, the chamber pressure also controls the operation of the fluidic element and the fuel flow and therefore the time delay associated with the supply of fuel to the chamber. When the chamber pressure is low (i.e. large exhaust orifice), fuel flow into the chamber is faster and can result in autoignition. When the chamber pressure is high (i.e. small exhaust orifice), the fuel supply following combustion is delayed which can result in misfire. Several exhaust orifice configurations were tested and the results indicate that a simple orifice with aspect ratio (diameter to thickness) 2 yield the best performance.

Mixture Flow, the flow rate of fuel and oxidizer are a crucial performance parameter. The present results show that increasing the mixture flow rate to the combustion chamber results in a higher ideal firing frequency, higher actuation frequencies, and often higher chamber pressures. However, it was also found that although high flow rates often lead to higher (dimensional) operating frequencies they also result in lower peak normalized frequencies.

Chamber Volume. A decrease in the chamber volume increases the ideal firing frequency, provides higher maximum actuation frequencies, but usually at lower peak normalized frequencies. Furthermore, a reduction in chamber volume results in a decrease of the peak chamber pressure primarily to a higher heat transfer loss.

Ignition Locations. The location of the spark source affects the flame propagation and therefore the actuator performance. A spark at located $0.25L$ below the exit plane forces the flame front to propagate upstream, opposite the direction of the nominal gas flow, resulting in the highest peak pressure but lowest maximum actuation frequency. When the spark is located $0.75L$ below the exit plan the flame front propagates downstream with the nominal gas flow resulting in the lowest peak pressure but the highest maximum actuation frequency. The centrally located spark ($0.50L$ below the exit plane) enables the flame front to propagate in both directions, optimizing the peak pressure and maximum actuation frequency. Using multiple sparks during the combustion cycle can improve both pressure and maximum actuation frequency by faster fuel consumption which reduces rise time. Using three spark gaps at $l_s/L = 0.25, 0.50, \&$

0.75 provides the highest peak pressures and maximum actuation frequencies with the shortest rise time and pulse duration.

Air Injection. The location of the injection was designed to provide swirl motion within the combustion chamber. The injection port was varied axially to $0.25L$, $0.50L$, and $0.75L$ below the exit plane. It was found that injection at $0.75L$ yielded optimal actuation frequencies and peak chamber pressure (best performing configuration). Air injection at $0.25L$ resulted in the lowest chamber pressure.

A passive fluidic element in the nonpremixed COMPACT is used to regulate the flow of fuel while the air is injected at sonic speeds directly into the chamber. Earlier premixed designs had to regulate the mixture of both fuel and air, using a relatively high feed-line pressure. In the nonpremixed configuration the pressure upstream of the fluidic element is lower, allowing the actuator to operate at lower chamber pressures. This is extremely important at high actuation frequencies when the chamber pressure is inherently lower. It was also found that the resistance of the fluidic element as measured by the porosity of the sintered metal can significantly affect the performance of the actuator. High porosity metal allows more combustion products to pass upstream through the fluidic element during the actuation cycle, resulting in lower peak pressures and shorter pulse durations. Of course, higher porosity is needed for high flow rates to attain in increased actuation frequency.

Reed Valves. The flow of fuel was also controlled with reed valves with the objective of increasing the chamber pressures with reduced backflow of combustion products. It is shown that the use of reed valves results in higher jet impulse, however the mechanical valves raise concerns regarding fatigue and therefore reliability. Additional concern with the (thin metal) reed designs is that they retain significant heat and can lead to premature autoignition.

Direct Fuel Injection. When the fuel inlet is changed to direct injection, the combustor can deliver high jet impulse. However, the fuel injection system operates at subsonic speeds while the air injection operates at sonic speed. Similar to the fluidic element, the high chamber pressures during combustion temporarily stops the fuel flow long enough for the flame to extinguish before re-injection (fuel injection at sonic speed can cause autoignition). Three configurations of direct fuel and air injection were tested: co-rotational swirl, impinging flows with swirl, and impinging flows without swirl. The maximum actuation frequency depends on the distance between air and fuel injectors. The furthest distance configuration (co-rotational swirl) yields the highest actuation frequency while the shortest distance configuration (impinging flow with swirl) has the lowest actuation frequency. The highest peak pressures and second longest pulse duration occur during co-rotational swirl. Impinging flow without swirl results in the shortest pulse duration and rise time with the second highest pressure levels through the frequency range. Impinging flow with swirl had the longest pulse duration and rise time with the lowest peak pressure levels through the operating range.

REFERENCES

- Amitay, M., V. Kibens, et al., "The Dynamics of Flow Reattachment over a Thick Airfoil Controlled by Synthetic Jet Actuators," AIAA Paper 99-1001, 1999.
- Amitay, M., Smith, B.L., and Glezer, A., "Aerodynamic Flow Control Using Synthetic Jet Technology," AIAA Paper 98-0208, 1998.
- Ballal, D. R. and A. H. Lefebvre, "The Influence of Flow Parameters on Minimum Ignition Energy and Quenching Distance," *Proceedings of the 15th International Symposium on Combustion*, 1473-1481, 1975.
- Beck, B. T., A. D. Cutler, et al., "A Resonant Pulse Detonation Actuator for High-Speed Boundary Layer Separation Control," *11th International Symposium on Flow Visualization*, University of Notre Dame, 2004.
- Boyarko, G. A., C.-J. Sung, et al., "Catalyzed Combustion of Hydrogen-Oxygen in Platinum Tubes for Micro-Propulsion Application," AIAA 2004-303, 2004.
- Brzozowski, D. and A. Glezer, "Transient separation control using pulse-combustion actuation," AIAA Paper, 2006.
- Crittenden, T. M., "Fluidic Actuators For High Speed Flow Control," Mechanical Engineering. Atlanta, GA, Georgia Institute of Technology. Ph.D. Thesis, 2003.
- Crittenden, T. M., B. J. Warta, et al., "Characterization of combustion powered actuators for flow control", AIAA Paper 2006-2864, 2006.
- Cutler, A. D., B. Terry Beck, et al., "Development of a pulsed combustion actuator for high-speed flow control," AIAA Paper 2005-1084, 2005.
- Epstein, A. H., S. D. Senturia, et al., "Micro-Heat Engines, Gas Turbines, and Rocket Engines," AIAA Paper 97-1773, 1997.
- Fried, A. and I. E. Idelchik, *Flow Resistance: A Design Guide for Engineers*, Hemisphere Publishing, New York, 1989.

- Fu, K., A. J. Knobloch, et al., "Microscale Combustion Research for Applications to MEMS Rotary IC Engines," *Proceedings of ASME NHTC Paper NHTC2001-20089*, 2001.
- Geng, T., F. Zheng, et al., "Experimental and numerical investigation of an 8-cm valveless pulsejet," *Journal of Experimental Thermal and Fluid Science*, **31**, 641-647, 2007.
- Glezer, A., M. Amitay, et al., "Aspects of low- and high-frequency actuation for aerodynamic flow control" *AIAA Journal*, **43**, 1501-1511, 2005
- Heywood, J. B., *Internal Combustion Engine Fundamentals*, McGraw-Hill, New York, 1988.
- John, J. E. A., *Gas Dynamics*. Boston, MA, Allyn and Bacon, Inc, 1969.
- Kailasanath, K., "Review of Propulsion Application of Detonation Waves," *AIAA Journal* **38**, 1156-888, 2000.
- Kiker, A. P., "Experimental Investigations of Mini-Pulsejet Engines," Aerospace Engineering, North Carolina State University, M.S. Thesis, 2005
- Lee, D. H., D. E. Park, et al., "Fabrication and test of a MEMS combustor and reciprocating device," *Journal of Micromechanics and Microengineering*, **12**, 26-34, 2001.
- Peters, N., "Turbulent burning velocity for large-scale and small-scale turbulence," *Journal of Fluid Mechanics*, **384**, 107-132, 1999.
- Smith, D. R., Amitay, M., and Glezer, A., "Modification of Lifting Body Aerodynamics using Synthetic Jet Actuators," AIAA Paper 98-0209, 1998.
- Spadaccini, C. M., J. Peck, et al., "Catalytic combustion systems for microscale gas turbine engines." *Journal of Engineering for Gas Turbines and Power*, **129**, 49-60, 2007.
- Turns, S. R., *An Introduction to Combustion*, McGraw-Hill, New York, 2000.

- Vukasinovic, B. and A. Glezer, "Transitory fluidic control of turbulent shear flows," *AIAA Journal*, **2**, 1042-1057, 2006.
- Waitz, I. A., G. Gauba, et al., "Combustors for Micro-Gas Turbine Engines," *Proceedings of the ASME Aerospace Division*, **52**, 1996.
- Wan, Q., W. L. Roberts, et al., "Computational analysis of the feasibility of a micro-pulsejet." *Journal of International Communications in Heat and Mass Transfer*, **32**, 19-26, 2005.